Dissection of Complex Behavior and Whole-Brain Functional Mapping in Larval Zebrafish

Dissection of complex behavior and whole-brain functional mapping in larval zebrafish

ABSTRACT

Understanding how the brain transforms sensory input into complex behavior is a fundamental question in systems neuroscience. Using larval zebrafish, we study the temporal component of phototaxis, which is defined as orientation decisions based on comparisons of light intensity at successive moments in time. We developed a novel "Virtual Circle" assay where whole-field illumination is abruptly turned off when the fish swims out of a virtually defined circular border, and turned on again when it returns into the circle. The animal receives no direct spatial cues and experiences only whole-field temporal light changes. Remarkably, the fish spends most of its time within the invisible virtual border. Behavioral analyses of swim bouts in relation to light transitions were used to develop four discrete temporal algorithms that transform the binary visual input (uniform light/uniform darkness) into the observed spatial behavior. In these algorithms, the turning angle is dependent on the behavioral history immediately preceding individual turning events. Computer simulations show that the algorithms recapture most of the swim statistics of real fish. We discovered that turning properties in larval zebrafish are distinctly modulated by temporal step functions in light intensity in combination with the specific motor history preceding these turns. Several aspects of the behavior suggest memory usage of up to 10 swim bouts (~10 sec).

Thus, we show that a complex behavior like spatial navigation can emerge from a small number of relatively simple behavioral algorithms.

Simultaneous whole-brain functional imaging should in principle provide a comprehensive understanding of the functional organization of the brain. However, the sheer quantity of neurons in whole-brain data makes extracting such an understanding a daunting task. An important first step is breaking up the neurons into functionally related clusters. These clusters then form manageable units for understanding and modeling the brain. Leveraging recent advances in light-sheet calcium imaging of behaving larval zebrafish, we recorded the ~100,000 neurons of the entire brain simultaneously at single-neuron resolution. We then employed a custom clustering algorithm to automatically classify neurons into functional clusters (~100 clusters per animal), characterized the sensory-motor transformations and compared multiple stimulus conditions. To facilitative in-depth exploratory analysis of whole-brain functional data, we constructed an interactive analytical software platform. This approach allowed us to both identify several known functional brain regions as well as discover previously uncharacterized activity patterns. In particular, the anterior hindbrain region shows great promise as an important site for sensory-motor transformations.

Table of Contents

ACKNOWLEDGEMENTS

I am indebted to many generous people who have dedicated their time and efforts to supporting me.

First, I would like to thank Florian, my advisor, who has shown me, both by example and through his guidance, that being a scientist could be an immensely gratifying experience. His flexible and incredibly generous style of leadership has encouraged me to be independent and find my own intellectual voice, and his optimistic and supportive nature has made me a much happier person over my years in graduate school.

Many thanks also to my labmates in the Engert Lab, who have been a constant source of intellectual stimulation and companionship. Thanks to Drew Robson and Jennifer Li, whose enthusiasm and expertise in neuroscience have inspired me to join the field, and Ruben Portugues, who taught me many skills and gave me much good advice during my more junior years in the lab. The imaging project would not have been possible without my collaborators, especially Yu Mu, Misha Ahrens and Yu Hu, and it has been a great pleasure to work with and learn from them.

I would also like to thank my thesis committee members (past and present): Christopher Harvey, Alexander Schier, Bence Olveczky, Sharad Ramanathan, and especially my committee chair, Joshua Sanes, for their long-term mentorship and support. I am thankful to Venkatesh Murthy, who offered me the opportunity to work in his lab over a summer; Alain Viel, for providing workspace and personal support through the Harvard College teaching labs; and the

MCO program and the Center for Brain Science, for providing resources and a wonderfully supportive environment for my graduate studies.

I am also deeply grateful to my friends and family who have supported me throughout graduate school. Laila Akhmetova and Ching-Han Shen have shown me a world much bigger and more beautiful than I knew before, and their friendships brought me courage, faith and much laughter. My friends from high school that are currently in the States made me feel like I have never been far away from home. Thanks to Harvard Graduate Women in Science and Engineering and the Dudley House Orchestra for providing a warm space for friendship and personal growth throughout graduate school. Finally, thanks to my parents, for their unwavering love and support from across the globe; to my husband Aaron Kuan, for his unbounded love and encouragement; and my baby daughter, with whom the world starts anew.

1. General Introduction

1.1 Overview

The overarching goal of systems neuroscience is to achieve an understanding of how neural networks in the brain integrate sensory input and generate behavioral output. The first step in this investigation is often behavioral studies, in which the sensory input is controlled and behavioral responses are carefully analyzed. These experiments can often reveal the underlying neural computations that transform the sensory input to behavioral output, which will then serve as guiding hypotheses for a mechanistic understanding on the neural circuitry level.

However, for complex behavior, large populations of neurons across multiple brain regions may be involved, and it is generally a difficult task to achieve an understanding of widespread and complicated neural dynamics. Given brain-wide neural recordings of a behaving animal, we can map direct neural representations of the sensory input and motor output with relative ease, but the neural networks involved in between these two ends may require more careful and systematic analysis. In addition, with fast advancements in the quality and quantity of functional imaging data, the integration and accumulation of circuit information from a large number of individual focused studies becomes a more exacting and pressing task.

This dissertation describes the discovery of a complex behavior in the larval zebrafish, and subsequently, an exploration of the complex landscape of brain-wide neural dynamics. More specifically,

The remaining portions of this introductory chapter provides background information on the choice of larval zebrafish as a model organism for behavioral and systems neuroscience,

large scale functional studies and data analysis, and insights from existing studies on the functional architecture of the larval zebrafish brain.

Chapter 2 presents the discovery of a spatial navigation behavior guided by temporal changes in illumination level, and presents a set of relatively simple algorithms that can explain the complex behavioral phenotype.

Chapter 3 is an exploration of simultaneous whole-brain calcium imaging data at the single cell resolution, with the aim of reducing the full dataset into manageable functional maps to aid hypothesis generation and downstream analyses.

Chapter 4 discusses the recurrent themes of exploration and reduction, as well as the implications of these studies and future directions.

1.2 LARVAL ZEBRAFISH AS A MODEL IN BEHAVIORAL AND SYSTEMS NEUROSCIENCE

The fundamental challenge in neuroscience is to understand how the brain integrates sensory information from the environment and generates behavior. The larval zebrafish is an excellent model to study the neural basis of behavior: it is a behaving vertebrate with a small and translucent brain that allows for non-invasive optical methods to monitor and manipulate neural circuits (Friedrich, Jacobson, and Zhu 2010; Portugues et al. 2013; Baier and Scott 2009; McLean and Fetcho 2011). Calcium imaging techniques have allowed near-simultaneous acquisition of neural activity of almost all of the ~100,000 neurons in the larval zebrafish brain during behavior (Ahrens et al. 2013). But this poses a significant challenge for the analysis and interpretation of such large and complex datasets. One approach is to analyze the imaging data in a data-driven fashion, as I will discuss in the next section. The other more dominant approach is

to use behavioral analysis to generate hypotheses and guide the identification of specific neural circuits. The zebrafish behavioral repertoire has been comprehensively reviewed by (Fero, Yokogawa, and Burgess 2011), and I will only briefly introduce the relevant categories in this section.

The week-old zebrafish displays a number of innate, robust visual behaviors (Budick and O'Malley 2000; Portugues and Engert 2009). Examples include the optomotor response (OMR), the optokinetic reflex (OKR), prey tracking, the visual escape behavior, the dark flash response and (spatial) phototaxis. In OMR, larval zebrafish respond to translational motion by orienting and swimming along the direction of the moving stimulus (Neuhauss et al. 1999; Orger et al. 2000). In OKR, zebrafish track rotational motion with their eyes with a smooth pursuit followed by a fast saccade to reset the eye position (Easter and Nicola 1997). Both behaviors are robust even in immobilized preparations, and serve to minimize retinal "slip" when the visual field moves. In addition to these reactions to whole-field motion, larval zebrafish also responds discriminately to motion of a prey-sized target versus a much larger target. A small moving dot elicits prey tracking by eye convergence and specialized maneuver of the tail to orient towards the dot (Gahtan, Tanger, and Baier 2005; McElligott and O'malley 2005). A quickly expanding dot with signatures of impending collision (looming) evokes an innate escape behavior (Dunn et al. 2016). In general, larval zebrafish also prefer light over darkness, possibly because foraging behavior is much more effective in light (Flamarique 2016). This preference is evident from their positive phototaxis behavior (orientation towards light) (Brockerhoff et al. 1995; Michael B Orger and Baier 2005; Huang et al. 2013; Burgess, Schoch, and Granato 2010) as well as their dark flash response, which is a large angle turn that occurs upon sudden darkening of the surroundings, while their response to onset of whole-field illumination is less pronounced. While

an abrupt decrease of luminosity may potentially signal an overshadowing predator or an unfavorable navigational move, prolonged darkness is not a noxious stimulus to the larval zebrafish - they gradually adapt within a time frame of tens of minutes (Burgess and Granato 2007).

Navigation behavior in the form of chemotaxis and thermotaxis has been studied extensively in *E. coli* (Segall, Block, and Berg 1986; Brown and Berg 1974), *C. elegans* (Zariwala et al. 2003; Gray, Hill, and Bargmann 2005; Ryu and Samuel 2002), and *Drosophila* (Gomez-Marin, Stephens, and Louis 2011; Louis et al. 2008; Luo et al. 2010). In larval zebrafish, perhaps due to the difficulty of implementing a controlled gradient in an aquatic environment, chemotaxis has not been characterized despite potential for such studies (Fero, Yokogawa, and Burgess 2011). A recent study described thermal navigation in larval zebrafish, and reported that in addition to modulating their turn magnitude, animals turn in a biased direction until they achieve a favorable orientation (Robson 2013). Spontaneous swimming behavior has also been described in another recent study as alternating sequences of repeated turns to the left and to the right (Dunn, Mu, et al. 2016). Both behaviors highlight biased turning probability that result in concerted turns over successive swim bouts. This is in concordance with a subset of the navigational strategies that I propose in Chapter 2 in the context of navigation guided by temporal changes of whole-field illumination (i.e. a series of dark flashes triggered by the animal's position). Fero et al. have also speculated that the first turn in response to a dark flash could be a navigational movement instead of a startle response (Fero, Yokogawa, and Burgess 2011), based on the fact that if the stimulus light is placed at one end of the arena, this turn will be in the direction of the extinguished light (Burgess and Granato 2007). Chapter 2

expands on this idea, and show that the complex behavioral phenotype can mostly be explained by navigational strategies involving short-term memory.

1.3 LARGE-SCALE FUNCTIONAL IMAGING AND DATA ANALYSIS

For neuroscientists, experimentalists and theorists alike, having access to the neural activity at high spatial and temporal resolution for all the neurons in an advanced brain has been a long time dream. Conventional wisdom dictates that there is an inherent tradeoff between the resolution of the measurement and the scope of coverage. On one side of the spectrum, the electric potential of a single neuron can be measured with great temporal resolution using electrophysiology; on the other end, whole-brain functional activity in a brain as large as the human brain is recorded routinely with functional magnetic resonance imaging (fMRI).

To achieve a comprehensive understanding of the brain, it is critical to bridge the information obtained at different scales. Calcium imaging methods span a broad middle range of this continuum. Genetically encoded calcium indicators (GECI's) can be broadly expressed in neural populations to optically report neural activity with increasing sensitivity and temporal resolution (Grienberger and Konnerth 2012; Chen et al. 2013). Combined with various optic techniques (Ahrens and Engert 2015; Prevedel et al. 2014; Keller and Ahrens 2015; Broxton et al. 2013), calcium imaging that can be applied to study neural circuits at the synaptic scale (Higley and Sabatini 2008), larger neural populations in superficial mammalian cortices (Peron, Chen, and Svoboda 2015), or almost the entire brain or central nervous system in smaller model organisms (Lemon et al. 2015; Schrödel et al. 2013; Prevedel et al. 2014; Nguyen et al. 2015; Venkatachalam et al. 2016). In particular, in the transparent larval zebrafish, two-photon or

recent light-sheet imaging techniques enabled the recording of almost all of the hundred thousand neurons in the brain at single cell resolution (Panier et al. 2013; Ahrens et al. 2013).

With the rapid advancement of functional imaging techniques, data acquisition will become increasingly streamlined, and single experiments can yield terabytes of neural data that are not only large in volume but also of high complexity. The next pressing challenge is to advance the analysis and interpretation of such large-scale datasets. There are at least two complementary styles towards data analysis, mostly depending on the strength of the data and traditions of the field. For fMRI, neuronal activity is indirectly reported by secondary BOLD (Blood-oxygen-level dependent) signals with comparatively low spatial and temporal resolution (on the order of $1mm^3$ and several seconds). Therefore, the common analyses are top-down approaches that seek holistic insights and are less limited by the resolution, such as mapping large-scale features (Huth et al. 2012), examining functional connectivity of large networks (Rubinov and Sporns 2010), and probabilistic and generative modelling (Huth et al. 2016). For neurophysiological studies, a bottom-up approach focused on small circuits is traditionally favored, as only small targets can be dissected with high precision to achieve a mechanistic understanding. In this case, large-scale datasets may be screened for a small subset of neurons that are related to the behavior of interest, and in animal models, these neurons can then be probed with other techniques (Yizhar et al. 2011) to test for necessity and sufficiency, thereby complementing the functional imaging approach that only reveals correlations.

The hope is that the bottom-up and the top-down approaches would meet naturally with the emergence of datasets that boast both brain-wide coverage and single-neuron-resolution. It may be tempting to wish that the knowledge accumulated from studies of small circuits would eventually lead to a comprehensive understanding of the brain. But to quote P.W. Anderson

(Anderson 1972), “the behavior of large and complex aggregates of elementary particles, it turns out, is not to be understood in terms of a simple extrapolation of the properties of a few particles. Instead, at each level of complexity entirely new properties appear.” Although such high-level properties may be more difficult to characterize and quantify, the diversity and complexity of the brain-wide dynamics cannot be predicted from responses of individual neurons, and the analysis of neural activity from large populations will open up great scientific opportunities.

In their review on analysis of large-scale neural data with dimensionality reduction (Cunningham and Yu 2014), the authors listed three motivations for population studies. The first one is single-trial statistical power. For traditional recordings that sample one imaging plane or a sub-region at a time, functional comparisons across the brain can only be made in reference to externally measurable or controllable variables like the stimulus or the behavior. Simultaneous brain-wide recordings are especially suitable for single-trial analysis, and one can examine activity patterns that, for example, correspond to internal states that are not reflected in a trial average. The second motivation is to form and test hypotheses about population activity structure where heterogeneous single-neuron responses cannot explain the neural mechanisms. Lastly, visualizing large amounts of data from populations of neurons promotes data-driven hypothesis generation.

Dimensionality reduction is a class of statistical methods that is very befitting for analyzing large-scale datasets. Cunningham et al. also reviewed the common methods applied to neural data, and discussed their suitability for different types of data. This includes basic covariance methods, such as Principal component analysis (PCA) and factor analysis (FA); time series methods, such as hidden Markov models (HMM) Gaussian process factor analysis (GPFA), latent linear dynamical systems (LDS) and latent nonlinear dynamical systems (NLDS);

methods with dependent variables, such as linear discriminant analysis (LDA); and nonlinear dimensionality reduction methods, such as Isomap and locally linear embedding (LLE). However, while these methods are good for simplifying large datasets by mapping them into lower dimensional space, there are not necessary optimized for visualizing and exploring complex data. It is very difficult to visualize the extracted latent variables in a high-dimensional space, so only 2-dimensional or 3-dimensional projections can be examined. In addition, usually only very few dimensions have intuitive interpretations, and visualization in highly abstract dimensions is often less fruitful. But for neural activity data, if every time point is viewed as a dimension, I would argue that although the data is very high-dimensional, the time-series carries rich information is nevertheless very intuitive for neuroscientists. I would suggest that for exploratory purposes, neural data is better reduced in the sampling dimension (e.g. pixels or neurons) instead of the time dimensions. In this regard, clustering methods are more flexible in representing the relationship between neurons (or other recording units). While dimensionality reduction methods aim to reduce the number of dimensions, cluster analysis aims to reduce the number of examples by grouping objects that are similar together, and is essentially exploratory analysis with little or no prior knowledge (Xu and Wunsch 2005).

One of the most popular and simple clustering algorithms, k-means, was first proposed over 50 years ago. Since then thousands of clustering algorithms have been published, yet, k-means is still widely used (Jain 2010). This underlines the complex nature of the clustering problem and the difficulty in designing a general purpose clustering algorithm. In Chapter 3, I describe a customized unsupervised clustering method to extract the most representative groups of active neurons. These groups would then represent network elements, and be of great interest for many types of downstream analysis.

For the remaining part of this section, I will briefly summarize some recent large-scale imaging studies using advanced technology in different model organisms. Most of them are in fact technique papers, and although not too surprising, methods for the interpretation of brain-wide functional data are significantly outpaced by tools for their acquisition in animal models.

C. elegans, as a model organism with a stereotypic nervous system of just 302 identifiable neurons, and with the structural connectome described 30 years ago [c], has been an attractive target for whole-brain imaging. Schrödel, Prevedel et al. (Schrödel et al. 2013) demonstrated near-simultaneous recording of 70% of all head neurons, using nuclear GCaMP as reporter of neural activity, and two-photon light-sculpting technique to achieve volumetric acquisition speeds of about 5 Hz. The next study (Prevedel et al. 2014) reported an even faster technique, light-field microscopy, applied on both *C. elegans* and larval zebrafish (with up to 20 Hz for the volume of the larval zebrafish brain, although single-cell resolution was compromised). Another two recent studies (Venkatachalam et al. 2016; Nguyen et al. 2015) reported fast volumetric imaging with spinning-disk confocal microscopy, but in freely moving worms. These studies focused on the technique, and the analysis mainly consists of correlation analysis and identification of individual neurons. In Kato, Kaplan, Schrödel et al. (Kato et al. 2015), constrained worms were imaged with a spinning disc microscope, and Principle Component Analysis (PCA) was their method of choice. They emphasize that a large proportion of neurons together engage in "coordinated, dynamical network activity" and showed that the first three principle components, which roughly correspond to movement in different directions, are robustly represented in the population dynamics.

Drosophila functional imaging in adult flies are usually limited to smaller regions, for example, the antenna lobe (Akerboom et al. 2012; Chen et al. 2013) or the optic lobe (Seelig et

al. 2010), presumably because its small size and lack of transparency makes it technically difficult to image large sections of the brain, while its vast resources for genetic labelling makes studying smaller and more precise circuits more attractive in this model. For *Drosophila* larvae, a recent paper reported light-sheet imaging of the entire central nervous system (Lemon et al. 2015) at 2 or 5 Hz, with fictive behavior recorded. They presented a coarse mapping of motor activity, described the activity of 24 manually drawn ROI's relative to the motor activity, analyzed single-neuron activity for ~200 neurons mostly in relation to motor waves, performed registration across animals and identified 4 types of neurons.

As mentioned before, larval zebrafish is a transparent model of intermediate size, ideal for either whole-brain optical imaging or optical interrogation of smaller circuits. The visuomotor circuits are the most studied, and have been discussed extensively in a very recent review (Orger 2016).

In mammalian studies, functional imaging at cellular resolution has mostly been limited to hundreds of neurons in small brain regions. Methods for automated ROI analysis (Mukamel, Nimmerjahn, and Schnitzer 2009; Pnevmatikakis et al. 2016) provide excellent opportunities for scaled-up analysis. In one recent study in mice (Peron et al. 2015), the authors examined approximately 12,000 neurons per animal in the superficial barrel cortex. Another study (Chen et al. 2016) was able to track anatomically-identified projection neurons across sensory cortices with multi-area two-photon imaging.

1.4 ANATOMICAL MAPPING IN LARVAL ZEBRAFISH

To achieve a comprehensive understanding of neural circuits, functional activity maps need to be examined in the proper anatomical context. In a very small model organism like *C. elegans*,

studies across different scales are easy to integrate since all individual neurons can be identified. For much larger models, individual studies typically specialize in a particular anatomical region, and it is imperative to have resources for brain-level mapping that integrate data into the same framework (Oh et al. 2014). For larval zebrafish, given the ease of brain-wide imaging, developing resources to easily merge anatomical as well as functional data at the cellular resolution would be extremely useful (Arrenberg and Driever 2013).

Indeed, there has been some recent effort to promote a high-resolution standardized digital atlas to facilitate the application of anatomical information already available in more traditional formats (see Arrenberg and Driver 2013 for a list of anatomical resources for the larval and adult zebrafish brain). Ronneberger et al. (Ronneberger et al. 2012) developed a software that maps gene expression data with cellular resolution to a 3D standard brain of 2-4 d post-fertilization larvae (dpf). Marquart et al. (Marquart et al. 2015) haven generated a searchable database of Gal4 and Cre lines for 6 dpf larvae. Owen et al. (Randlett et al. 2015) have built an atlas containing molecular labels for 5-7 dpf zebrafish, and have integrated it with brain-wide activity maps obtained by a post hoc staining assay (MAP-mapping). The mapping assay is high-throughput and easy to perform in freely swimming fish, and thus is excellent for registration to an atlas and comparisons between animals. Another comparable assay to map activity in freely swimming fish uses photoconversion of an integrative calcium sensor (CaMPARI) with UV light (Fosque et al. 2015).

In Chapter 3, I built on these methods and integrate functionally defined maps to these high-resolution anatomical maps. Such an integrated atlas provides an effective guide to the interpretation of experiments across different animals, and hopefully, to the accumulation of insights across many different studies of the larval zebrafish brain.

1.5 REFERENCES

Ahrens, Misha B, and Florian Engert. 2015. “Large-Scale Imaging in Small Brains.” *Current Opinion in Neurobiology* 32. Elsevier Ltd: 78–86. doi:10.1016/j.conb.2015.01.007.

Ahrens, Misha B., Michael B. Orger, Drew N. Robson, Jennifer M. Li, and Philipp J. Keller. 2013. “Whole-Brain Functional Imaging at Cellular Resolution Using Light-Sheet Microscopy.” *Nature Methods*, no. March. doi:10.1038/NMETH.2434.

Akerboom, J., T.-W. Chen, T. J. Wardill, L. Tian, J. S. Marvin, S. Mutlu, N. C. Calderon, et al. 2012. “Optimization of a GCaMP Calcium Indicator for Neural Activity Imaging.” *Journal of Neuroscience* 32 (40): 13819–40. doi:10.1523/JNEUROSCI.2601-12.2012.

Anderson, P W. 1972. “More Is Different.” *Science (New York, N.Y.)* 177 (4047). American Association for the Advancement of Science: 393–96. doi:10.1126/science.177.4047.393.

Arrenberg, Aristides B, and Wolfgang Driever. 2013. “Integrating Anatomy and Function for Zebrafish Circuit Analysis.” *Frontiers in Neural Circuits* 7 (April): 74. doi:10.3389/fncir.2013.00074.

Baier, Herwig, and Ethan K Scott. 2009. “Genetic and Optical Targeting of Neural Circuits and Behavior--Zebrafish in the Spotlight.” *Current Opinion in Neurobiology* 19 (5): 553–60. doi:10.1016/j.conb.2009.08.001.

Brockerhoff, SE, JB Hurley, U Janssen-Bienhold, SC Neuhauss, W Driever, and JE Dowling. 1995. “A Behavioral Screen for Isolating Zebrafish Mutants with Visual System Defects.” *Proceedings of the ...* 92 (November): 10545–49. http://www.pnas.org/content/92/23/10545.short.

Brown, D a, and H C Berg. 1974. “Temporal Stimulation of Chemotaxis in Escherichia Coli.” *Proceedings of the National Academy of Sciences of the United States of America* 71 (4): 1388–92. http://www.pubmedcentral.nih.gov/articlerender.fcgi?artid=388234&tool=pmcentrez&rendertype=abstract.

Broxton, Michael, Logan Grosenick, Samuel Yang, Noy Cohen, Aaron Andalman, Karl Deisseroth, and Marc Levoy. 2013. “Wave Optics Theory and 3-D Deconvolution for the Light Field Microscope.” *Optics Express* 21 (21): 25418. doi:10.1364/OE.21.025418.

Budick, S a, and D M O’Malley. 2000. “Locomotor Repertoire of the Larval Zebrafish: Swimming, Turning and Prey Capture.” *The Journal of Experimental Biology* 203 (Pt 17): 2565–79. http://www.ncbi.nlm.nih.gov/pubmed/10934000.

Burgess, Harold A, Hannah Schoch, and Michael Granato. 2010. “Distinct Retinal Pathways Drive Spatial Orientation Behaviors in Zebrafish Navigation.” *Current Biology : CB* 20 (4). Elsevier Ltd: 381–86. doi:10.1016/j.cub.2010.01.022.

Burgess, Harold A., and Michael Granato. 2007. “Modulation of Locomotor Activity in Larval Zebrafish during Light Adaptation.” *The Journal of Experimental Biology* 210 (Pt 14): 2526–39. doi:10.1242/jeb.003939.

Chen, Jerry L., Fabian F. Voigt, Mitra Javadzadeh, Roland Krueppel, and Fritjof Helmchen. 2016. “Long-Range Population Dynamics of Anatomically Defined Neocortical Networks.” *eLife* 5: 1–26. doi:10.7554/eLife.14679.

Chen, Tsai-Wen, Trevor J Wardill, Yi Sun, Stefan R Pulver, Sabine L Renninger, Amy Baohan, Eric R Schreiter, et al. 2013. “Ultrasensitive Fluorescent Proteins for Imaging Neuronal Activity.” *Nature* 499 (7458): 295–300. doi:10.1038/nature12354.

Cunningham, John P, and Byron M Yu. 2014. “Dimensionality Reduction for Large-Scale Neural Recordings.”

Nature Neuroscience 17 (11): 1500–1509. doi:10.1038/nn.3776.

Dunn, Timothy W., Christoph Gebhardt, Eva A. Naumann, Clemens Riegler, Misha B. Ahrens, Florian Engert, and Filippo Del Bene. 2016. "Neural Circuits Underlying Visually Evoked Escapes in Larval Zebrafish." *Neuron*. Elsevier Inc., 1–16. doi:10.1016/j.neuron.2015.12.021.

Dunn, Timothy W., Yu Mu, Sujatha Narayan, Owen Randlett, Eva A. Naumann, Chao Tsung Yang, Alexander F. Schier, Jeremy Freeman, Florian Engert, and Misha B. Ahrens. 2016. "Brain-Wide Mapping of Neural Activity Controlling Zebrafish Exploratory Locomotion." *eLife* 5 (MARCH2016): 1–29. doi:10.7554/eLife.12741.

Easter, S S, and G N Nicola. 1997. "The Development of Eye Movements in the Zebrafish (Danio Rerio)." *Developmental Psychobiology* 31 (4): 267–76. http://www.ncbi.nlm.nih.gov/pubmed/9413674.

Fero, Kandice, Tohei Yokogawa, and Harold A Burgess. 2011. *Zebrafish Models in Neurobehavioral Research*. Edited by Allan V. Kalueff and Jonathan M. Cachat. Vol. 52. Neuromethods. Totowa, NJ: Humana Press. doi:10.1007/978-1-60761-922-2.

Flamarique, Iñigo N. 2016. "Diminished Foraging Performance of a Mutant Zebrafish with Reduced Population of Ultraviolet Cones." *Proceedings. Biological Sciences / The Royal Society* 283 (1826): 20160058. doi:10.1098/rspb.2016.0058.

Fosque, Benjamin F, Yi Sun, Hod Dana, Chao-tsung Yang, Tomoko Ohyama, Michael R Tadross, Ronak Patel, et al. 2015. "Labeling of Active Neural Circuits in Vivo with Designed Calcium Integrators." *Science (New York, N.Y.)* 347 (6223): 755–60. doi:10.1126/science.1260922.

Friedrich, Rainer W., Gilad a. Jacobson, and Peixin Zhu. 2010. "Circuit Neuroscience in Zebrafish." *Current Biology* 20 (8). Elsevier Ltd: R371–81. doi:10.1016/j.cub.2010.02.039.

Gahtan, Ethan, Paul Tanger, and Herwig Baier. 2005. "Visual Prey Capture in Larval Zebrafish Is Controlled by Identified Reticulospinal Neurons Downstream of the Tectum." *The Journal of Neuroscience : The Official Journal of the Society for Neuroscience* 25 (40): 9294–9303. doi:10.1523/JNEUROSCI.2678-05.2005.

Gomez-Marin, Alex, Greg J Stephens, and Matthieu Louis. 2011. "Active Sampling and Decision Making in Drosophila Chemotaxis." *Nature Communications* 2 (January). Nature Publishing Group: 441. doi:10.1038/ncomms1455.

Gray, Jesse M, Joseph J Hill, and Cornelia I Bargmann. 2005. "A Circuit for Navigation in Caenorhabditis Elegans." *Proceedings of the National Academy of Sciences of the United States of America* 102 (9): 3184–91. doi:10.1073/pnas.0409009101.

Grienberger, Christine, and Arthur Konnerth. 2012. "Imaging Calcium in Neurons." *Neuron* 73 (5). Elsevier Inc.: 862–85. doi:10.1016/j.neuron.2012.02.011.

Higley, Michael J, and Bernardo L Sabatini. 2008. "Calcium Signaling in Dendrites and Spines: Practical and Functional Considerations." *Neuron* 59 (6): 902–13. doi:10.1016/j.neuron.2008.08.020.

Huang, Kuo-Hua, Misha B. Ahrens, Timothy W. Dunn, and Florian Engert. 2013. "Spinal Projection Neurons Control Turning Behaviors in Zebrafish." *Current Biology*, August. The Authors. doi:10.1016/j.cub.2013.06.044.

Huth, Alexander G, Wendy A De Heer, Thomas L Griffiths, Frédéric E Theunissen, and L Jack. 2016. "Natural Speech Reveals the Semantic Maps That Tile Human Cerebral Cortex." *Nature* 532 (7600). Nature Publishing Group: 453–58. doi:10.1038/nature17637.

Huth, Alexander G, Shinji Nishimoto, An T Vu, and Jack L Gallant. 2012. “A Continuous Semantic Space Describes the Representation of Thousands of Object and Action Categories across the Human Brain.” *Neuron* 76 (6): 1210–24. doi:10.1016/j.neuron.2012.10.014.

Jain, Anil K. 2010. “Data Clustering: 50 Years beyond K-Means.” *Pattern Recognition Letters*. Vol. 31. doi:10.1016/j.patrec.2009.09.011.

Kato, Saul, Harris S. Kaplan, Tina Schrödel, Susanne Skora, Theodore H. Lindsay, Eviatar Yemini, Shawn Lockery, and Manuel Zimmer. 2015. “Global Brain Dynamics Embed the Motor Command Sequence of Caenorhabditis Elegans.” *Cell* 163 (3): 656–69. doi:10.1016/j.cell.2015.09.034.

Keller, Philipp J., and Misha B. Ahrens. 2015. “Visualizing Whole-Brain Activity and Development at the Single-Cell Level Using Light-Sheet Microscopy.” *Neuron* 85 (3). Elsevier Inc.: 462–83. doi:10.1016/j.neuron.2014.12.039.

Kinkhabwala, Amina, Michael Riley, Minoru Koyama, Joost Monen, Chie Satou, and Yukiko Kimura. 2010. “A Structural and Functional Ground Plan for Neurons in the Hindbrain of Zebrafish.” *PNAS*, 1–6. doi:10.1073/pnas.1012185108/-/DCSupplemental.www.pnas.org/cgi/doi/10.1073/pnas.1012185108.

Lemon, William C, Stefan R Pulver, Burkhard Hoeckendorf, Katie Mcdole, Kristin Branson, Jeremy Freeman, and Philipp J. Keller. 2015. “Whole-Central Nervous System Functional Imaging in Larval Drosophila.” *Nature Communications* 6 (May): 7924. doi:10.1038/ncomms8924.

Louis, Matthieu, Thomas Huber, Richard Benton, Thomas P Sakmar, and Leslie B Vosshall. 2008. “Bilateral Olfactory Sensory Input Enhances Chemotaxis Behavior.” *Nature Neuroscience* 11 (2): 187–99. doi:10.1038/nn2031.

Luo, Linjiao, Marc Gershow, Mark Rosenzweig, Kyeongjin Kang, Christopher Fang-Yen, Paul a Garrity, and Aravinthan D T Samuel. 2010. “Navigational Decision Making in Drosophila Thermotaxis.” *The Journal of Neuroscience : The Official Journal of the Society for Neuroscience* 30 (12): 4261–72. doi:10.1523/JNEUROSCI.4090-09.2010.

Marquart, Gregory D., Kathryn M. Tabor, Mary Brown, Jennifer L. Strykowski, Gaurav K. Varshney, Matthew C. LaFave, Thomas Mueller, Shawn M. Burgess, Shin-ichi Higashijima, and Harold A. Burgess. 2015. “A 3D Searchable Database of Transgenic Zebrafish Gal4 and Cre Lines for Functional Neuroanatomy Studies.” *Frontiers in Neural Circuits* 9 (November): 78. doi:10.3389/fncir.2015.00078.

McElligott, Melissa B, and Donald M O’malley. 2005. “Prey Tracking by Larval Zebrafish: Axial Kinematics and Visual Control.” *Brain, Behavior and Evolution* 66 (3): 177–96. doi:10.1159/000087158.

McLean, David L, and Joseph R Fetcho. 2011. “Movement, Technology and Discovery in the Zebrafish.” *Current Opinion in Neurobiology* 21 (1). Elsevier Ltd: 110–15. doi:10.1016/j.conb.2010.09.011.

Mitra, Partha P. 2014. “The Circuit Architecture of Whole Brains at the Mesoscopic Scale.” *Neuron* 83 (6). Elsevier Inc.: 1273–83. doi:10.1016/j.neuron.2014.08.055.

Mukamel, Eran a, Axel Nimmerjahn, and Mark J Schnitzer. 2009. “Automated Analysis of Cellular Signals from Large-Scale Calcium Imaging Data.” *Neuron* 63 (6). Elsevier Ltd: 747–60. doi:10.1016/j.neuron.2009.08.009.

Neuhauss, S C, O Biehlmaier, M W Seeliger, T Das, K Kohler, W A Harris, and H Baier. 1999. “Genetic Disorders of Vision Revealed by a Behavioral Screen of 400 Essential Loci in Zebrafish.” *The Journal of Neuroscience : The Official Journal of the Society for Neuroscience* 19 (19): 8603–15. doi:10.5167/uzh-227.

Nguyen, Jeffrey P, Frederick B Shipley, Ashley N Linder, George S Plummer, Mochi Liu, Sagar U Setru, Joshua W Shaevitz, and Andrew M Leifer. 2015. “Whole-Brain Calcium Imaging with Cellular Resolution in Freely

Behaving Caenorhabditis Elegans." *Proceedings of the National Academy of Sciences of the United States of America*, no. 9: 33. doi:10.1073/pnas.1507110112.

Oh, Seung Wook, Julie A. Harris, Lydia Ng, Brent Winslow, Nicholas Cain, Stefan Mihalas, Quanxin Wang, et al. 2014. "A Mesoscale Connectome of the Mouse Brain." *Nature* 508 (7495). Nature Publishing Group: 207–14. doi:10.1038/nature13186.

Orger, M B, M C Smear, S M Anstis, and Herwig Baier. 2000. "Perception of Fourier and Non-Fourier Motion by Larval Zebrafish." *Nature Neuroscience* 3 (11): 1128–33. doi:10.1038/80649.

Orger, Michael B, and Herwig Baier. 2005. "Channeling of Red and Green Cone Inputs to the Zebrafish Optomotor Response." *Visual Neuroscience* 22 (3): 275–81. doi:10.1017/S0952523805223039.

Orger, Michael B. 2016. "The Cellular Organization of Zebrafish Visuomotor Circuits." *Current Biology* 26 (9). Elsevier Ltd: R377–85. doi:10.1016/j.cub.2016.03.054.

Panier, Thomas, Sebastián a Romano, Raphaël Olive, Thomas Pietri, Germán Sumbre, Raphaël Candelier, and Georges Debrégeas. 2013. "Fast Functional Imaging of Multiple Brain Regions in Intact Zebrafish Larvae Using Selective Plane Illumination Microscopy." *Frontiers in Neural Circuits* 7 (April): 65. doi:10.3389/fncir.2013.00065.

Peron, Simon, Tsai-Wen Chen, and Karel Svoboda. 2015. "Comprehensive Imaging of Cortical Networks." *Current Opinion in Neurobiology* 32. Elsevier Ltd: 115–23. doi:10.1016/j.conb.2015.03.016.

Peron, Simon, Jeremy Freeman, Vijay Iyer, Caiying Guo, and Karel Svoboda. 2015. "A Cellular Resolution Map of Barrel Cortex Activity during Tactile Behavior." *Neuron* 86 (3). Elsevier Inc.: 783–99. doi:10.1016/j.neuron.2015.03.027.

Pnevmatikakis, Eftychios A., Daniel Soudry, Yuanjun Gao, Timothy A. Machado, Josh Merel, David Pfau, Thomas Reardon, et al. 2016. "Simultaneous Denoising, Deconvolution, and Demixing of Calcium Imaging Data." *Neuron* 89 (2): 299. doi:10.1016/j.neuron.2015.11.037.

Portugues, Ruben, and Florian Engert. 2009. "The Neural Basis of Visual Behaviors in the Larval Zebrafish." *Current Opinion in Neurobiology* 19 (6): 644–47. doi:10.1016/j.conb.2009.10.007.

Portugues, Ruben, Kristen E Severi, Claire Wyart, and Misha B Ahrens. 2013. "Optogenetics in a Transparent Animal: Circuit Function in the Larval Zebrafish." *Current Opinion in Neurobiology* 23 (1). Elsevier Ltd: 119–26. doi:10.1016/j.conb.2012.11.001.

Prevedel, Robert, Young-Gyu Yoon, Maximilian Hoffmann, Nikita Pak, Gordon Wetzstein, Saul Kato, Tina Schrödel, et al. 2014. "Simultaneous Whole-Animal 3D Imaging of Neuronal Activity Using Light-Field Microscopy." *Nature Methods* 11 (7): 727–30. doi:10.1038/nmeth.2964.

Randlett, Owen, Caroline L Wee, Eva a Naumann, Onyeka Nnaemeka, David Schoppik, James E Fitzgerald, Ruben Portugues, et al. 2015. "Whole-Brain Activity Mapping onto a Zebrafish Brain Atlas." *Nature Methods* 12 (September): 1–12. doi:10.1038/nmeth.3581.

Robson, Drew N. 2013. "Thermal Navigation in Larval Zebrafish." *Doctoral Dissertation, Harvard University*. http://nrs.harvard.edu/urn-3:HUL.InstRepos:11158267.

Ronneberger, Olaf, Kun Liu, Meta Rath, Dominik Rueβ, Thomas Mueller, Henrik Skibbe, Benjamin Drayer, et al. 2012. "ViBE-Z: A Framework for 3D Virtual Colocalization Analysis in Zebrafish Larval Brains." *Nature Methods* 9 (7): 735–42. doi:10.1038/nmeth.2076.

Rubinov, Mikail, and Olaf Sporns. 2010. "Complex Network Measures of Brain Connectivity: Uses and

Interpretations." *NeuroImage* 52 (3). Elsevier Inc.: 1059–69. doi:10.1016/j.neuroimage.2009.10.003.

Ryu, William S, and Aravinthan D T Samuel. 2002. "Thermotaxis in Caenorhabditis Elegans Analyzed by Measuring Responses to Defined Thermal Stimuli." *The Journal of Neuroscience : The Official Journal of the Society for Neuroscience* 22 (13): 5727–33. doi:20026542.

Schrödel, Tina, Robert Prevedel, Karin Aumayr, Manuel Zimmer, and Alipasha Vaziri. 2013. "Brain-Wide 3D Imaging of Neuronal Activity in Caenorhabditis Elegans with Sculpted Light." *Nature Methods* 10 (10): 1013–20. doi:10.1038/nmeth.2637.

Seelig, Johannes D, M Eugenia Chiappe, Gus K Lott, Anirban Dutta, Jason E Osborne, Michael B Reiser, and Vivek Jayaraman. 2010. "Two-Photon Calcium Imaging from Head-Fixed Drosophila during Optomotor Walking Behavior." *Nature Methods* 7 (7): 535–40. doi:10.1038/nmeth0211-184b.

Segall, J E, S M Block, and H C Berg. 1986. "Temporal Comparisons in Bacterial Chemotaxis." *Proceedings of the National Academy of Sciences of the United States of America* 83 (23): 8987–91. http://www.pubmedcentral.nih.gov/articlerender.fcgi?artid=387059&tool=pmcentrez&rendertype=abstract.

Venkatachalam, Vivek, Ni Ji, Xian Wang, Christopher Clark, James Kameron Mitchell, Mason Klein, Christopher J Tabone, et al. 2016. "Pan-Neuronal Imaging in Roaming Caenorhabditis Elegans." *Proceedings of the National Academy of Sciences of the United States of America* 113 (8): E1082–88. doi:10.1073/pnas.1507109113.

Xu, Rui, and Donald II Wunsch. 2005. "Survey of Clustering Algorithms." *IEEE Transactions on Neural Networks* 16 (3): 645–78. doi:10.1109/TNN.2005.845141.

Yizhar, Ofer, Lief E Fenno, Thomas J Davidson, Murtaza Mogri, and Karl Deisseroth. 2011. "Optogenetics in Neural Systems." *Neuron* 71 (1). Elsevier Inc.: 9–34. doi:10.1016/j.neuron.2011.06.004.

Zariwala, Hatim a, Adam C Miller, Serge Faumont, and Shawn R Lockery. 2003. "Step Response Analysis of Thermotaxis in Caenorhabditis Elegans." *The Journal of Neuroscience : The Official Journal of the Society for Neuroscience* 23 (10): 4369–77. http://www.ncbi.nlm.nih.gov/pubmed/12764126.

2 NAVIGATIONAL STRATEGIES UNDERLYING PHOTOTAXIS

2.1 PREFACE

The following chapter is adapted from Chen, X., & Engert, F. (2014), "Navigational strategies underlying phototaxis in larval zebrafish", Frontiers in Systems Neuroscience, 8(March), 1–13, http://doi.org/10.3389/fnsys.2014.00039. I conceived the project, designed and performed the experiments, and analyzed the data. Florian Engert discussed the data and wrote the manuscript with me. Florian Engert supported the project.

2.2 INTRODUCTION

Quantitative insights into how the brain transforms sensory input to motor output are essential to understanding the neuronal basis of complex behavior. Ideally, a well-designed behavioral assay in combination with careful analysis can reveal a sequence of relatively simple algorithms that underlie these complex transformations (Marr 1982). These algorithms can then serve as testable hypotheses for studying the physiological properties of the underlying neuronal circuitry.

An interesting and important class of behaviors that is well-suited for such algorithmic analysis is taxis - an innate behavioral response to a directional stimulus or gradient of stimulus intensity. Examples of such stimuli and their respective taxes are light (phototaxis) (Sawin et al. 1994), chemicals (chemotaxis) (Louis et al. 2008), temperature (thermotaxis) (Mori and Ohshima 1995) and gravity (geotaxis) (Toma et al. 2002). The movement may be directed toward the stimulus (positive taxis) or away from it (negative taxis).

In order to achieve taxis behavior, an organism needs to compare samples of sensory information to inform its directional movement, but this comparison can be made in space or in time, and therefore, two general types of strategies for taxis behavior can be distinguished. Spatial strategies involve instantaneous comparisons between stimuli intensities at different points in space, while temporal strategies compare stimulus intensity at successive moments in time. Fraenkel and Gunn (Fraenkel and Gunn 1961) term the spatial and temporal strategies "tropotaxis" and "klinotaxis", respectively. A classic example of temporal taxis is the "biased random walk" strategy in bacteria chemotaxis (Segall, Block, and Berg 1986). An *E. coli* bacterium compares the chemical concentration at different times, and when it is moving away from an attractant like a food source, the tumbling frequency increases. Phototaxis, on the other hand, provides an intuitive example of a spatial strategy. Whenever an image is formed, light intensities at different points of the visual field can be compared and this can directly influence the animal's direction of travel. In comparison, temporal strategies for phototaxis are largely understudied, with a few exceptions such as the negative phototaxis of the blowfly larva *Calliphora* (Fraenkel and Gunn 1961) and dark photokineses in blind fish by means of deep brain photoreceptors (Fernandes et al. 2012). However, studies of temporally based decisions can be highly informative and necessarily include certain forms of memory, since each sample of sensory input needs to be compared to at least one previous set. An interesting question to ask is whether a vertebrate with binocular vision, such as the larval zebrafish, also employs temporal strategies in phototactic behavior. Such behaviors might be observed in natural environments when an animal enters a shadow, where the sudden darkening of the surroundings represents a temporal decrease in luminosity.

Larval zebrafish demonstrate positive phototaxis, that is, they are attracted by light and are averse to darkness (Brockerhoff et al. 1995; Orger and Baier 2005). As demonstrated by Burgess et al. (Burgess, Schoch, and Granato 2010), larval zebrafish respond to localized illumination by first turning toward the light source and then swimming forward. Another study showed that when a larval zebrafish is presented a left/right illumination contrast (black/white with sharp border at midline) that is stabilized relative to the fish's orientation, it turns robustly towards the white side (Huang et al. 2013). This shows that a purely spatial difference in luminosity is sufficient to elicit phototactic behavior in larval zebrafish, but leaves unresolved the question whether purely temporal changes in luminosity also contribute to phototactic behavior.

In order to develop a comprehensive understanding of phototaxis, we isolated its purely temporal component by presenting only spatially uniform stimuli - light and dark. To that end, we developed a novel "Virtual Circle" assay in which a virtual circular border (invisible to the fish) is defined within a uniformly illuminated arena. The lights are turned off when the fish crosses the border (leaving the circle), and are turned on again when the fish returns to within the circle. Despite the fact that the fish has no direct spatial information about the location of the virtual border, we find that its trajectory is remarkably well contained within the interior of the circle (or other geometric shapes as implemented in variants of this assay).

Since larval zebrafish swim in discrete bouts, this behavior can be modeled using discrete algorithms that transform the binary visual input (uniform light/uniform darkness) into specific swim properties. Analysis of the fish trajectories reveals four algorithms that modulate the swim turns (bouts) based on recent sensory and motor history: (1) the turning-angle magnitude is modulated by a light transition; (2) the (left/right) direction of turns following a light switch

depends on the direction of the previous turn. Computer simulations show that these first two algorithms are sufficient to ensure that a fish spends most of its time within the virtual border. The latter two algorithms suggest usage of memory of up to 10 bouts (~10 sec): (3) the cumulative angle during a dark interval modulates the turning direction of the subsequent bouts in light and (4) the probability of the fish changing the turning direction after entering the dark depends inversely on the duration of the preceding light interval. Algorithms (3) and (4) explain more complex properties of fish behavior like their general affinity to the virtual border and their ability to consistently turn in the direction that most quickly returns them to the virtual circle. These four algorithms inform us about how the larval zebrafish brain transforms purely temporal stimuli into a spatially well-defined behavior. In summary, this study characterizes temporal phototaxis in a vertebrate, and shows that this complex behavioral trait, which might appear to require an internal representation of space, can actually emerge from a small number of relatively simple computational rules.

2.3 TEMPORAL VERSUS SPATIAL PHOTOTAXIS

In order to test whether phototaxis consists of both spatial and temporal processing, we performed two simple assays: a spatial comparison assay and a temporal comparison assay. In the spatial comparison assay, a diffusive white screen surrounded by a black ring is placed beneath the arena (a transparent dish) and illuminated from below (**Figure 2.1A**). As expected, we find that a freely swimming fish stays within the (illuminated) center circle and avoids crossing into the dark area. We call this the "spatial comparison" assay because the fish can see the scattered light from the white area from all directions; as it is approaching the dark area, it can use this visual information to avoid crossing the border.

In the temporal comparison assay, named in the following the "Virtual Circle Assay" or "VC assay" (**Figure 2.1B**), we define a circular "virtual border" (that is invisible to the fish) in the center of a circular arena that is uniformly illuminated with white light through a diffusive screen. The fish starts inside the virtual circle, but as soon as it swims out of the circle, the light is switched off and the fish experiences complete darkness; when the fish returns, the whole field illumination is restored. Throughout the assay, the fish only perceives temporal changes of uniform white or uniform black visual inputs. We found that fish employ a variety of strategies to efficiently return to the virtual circle when plunged into darkness. The trajectory of the fish is therefore predominantly confined within the virtual border. This effect can also be observed when shapes other than a circle are used. **Figure 2.2A** shows examples of fish navigating in different virtual contexts with similar success.

The quantification of this behavior is greatly facilitated because larval zebrafish swim in discrete bouts (at a frequency of ~1 bout per second). A bout is characterized by a short burst of tail-oscillations, followed by an interbout period where the tail does not move (Budick and O'Malley 2000). In our assay, the position and heading direction of the fish is tracked smoothly with a high-speed infrared-sensitive camera. Because the heading direction oscillates together with the tail, bouts can be robustly detected by thresholding the change in heading-directions (**Figure 2.1C** lower panel; the corresponding velocity is shown for comparison in the upper panel). The complex trajectory of the fish can thus be dissected into a chain of discrete bouts for quantitative analyses.

We are most interested in trajectory segments close to the virtual border (**Figure 2.1D**), since these comprise the immediate response to changes in illumination. The most prominent feature we observed is that after exiting the virtual circle and experiencing darkness, the fish

quickly returns to the virtual circle. The average probability of returning within 3 bouts is 0.86 ± 0.02 (mean ± SEM, n = 32 fish, **Figure 2.1E**).

Figure 2.1. Spatial versus temporal phototaxis.

(A) Larval zebrafish prefer light over darkness in the spatial comparison assay. Upper panel: a diffusive (scattering) white screen surrounded by an opaque black ring is placed beneath the arena (a transparent dish) and illuminated from below. Lower panel: the full trajectory of a fish over a session of 8 min. Right panels: close-up views of trajectory segments close to the border. 3 example segments are shown (rotated into the same orientation), with swim direction indicated by the red, green and blue arrowheads; circular border indicated by the dashed red line. Note that the fish does not cross the border. **(B)** Temporal comparison assay, i.e. the Virtual Circle (VC) assay. The uniform illumination is turned off when the fish exits the virtual circle (dashed red circle, invisible to fish), and turned on again when the fish returns. Close-up view as in (A), additionally with yellow dots marking the point where the fish exits the virtual circle. **(C)** Larval zebrafish swim in distinct bouts. Upper panel shows the velocity of the fish over time. Lower panel: bouts are determined by thresholding the angular velocity (i.e. per-frame change of heading angle); red/green circles mark the start/end of bouts, dashed red lines mark the thresholds. **(D)** Trajectory segments close to the virtual border are extracted from the VC assay, with the point where fish exits the border aligned to the yellow dot. 3 example segments are shown in red, green and blue, with swim direction indicated by arrowhead. **(E)** The probability of each fish returning to light within 3 bouts of exiting the virtual circle, summarized as a histogram for all 32 fish. Dashed cyan line indicates population mean.

(Figure 2.1 continued)

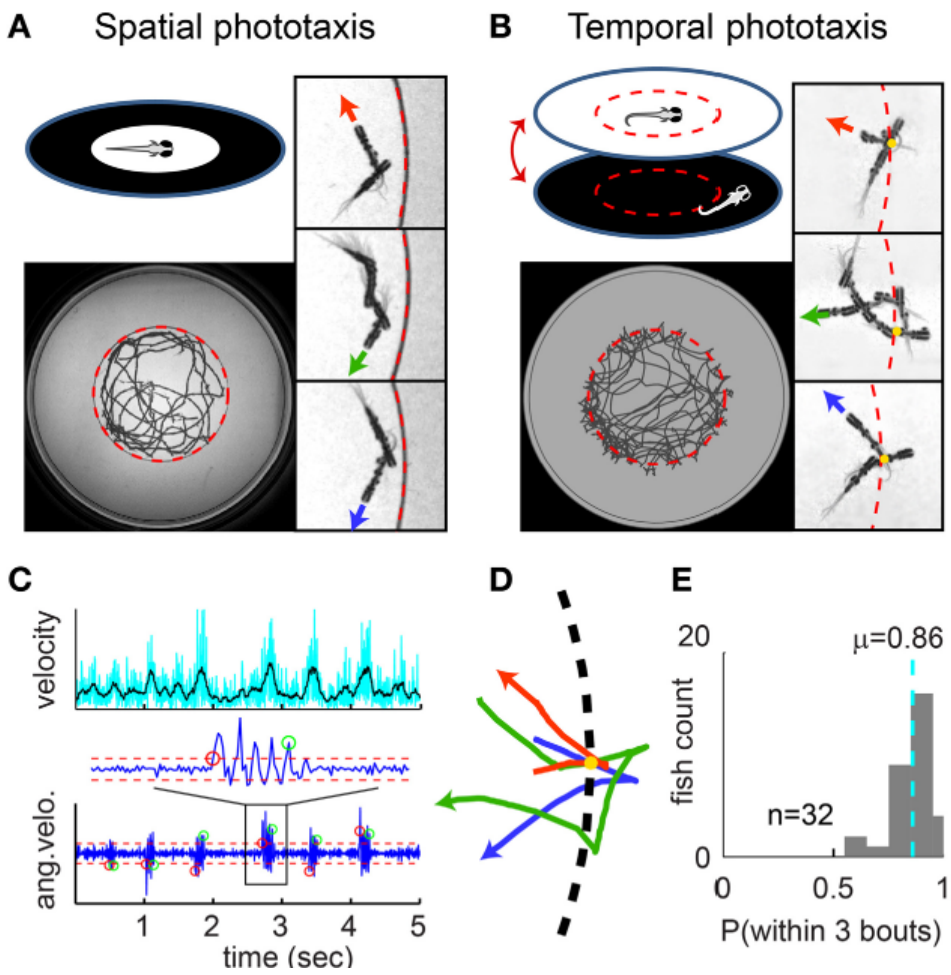

Figure 2.2. Variants of the Virtual Circle assay. Related to Figure 2.1.

(A) Shape variants of the VC assay. Left: a square-shaped virtual border. Example trace from a single fish shows that the trajectory is tightly restricted to within the border. Right: a more irregularly shaped virtual border. Traces from two fish are overlaid (note that each fish only reached the edge of the arena once). Insets: shape of virtual borders, with white area indicating location for (uniform) light-on, and dark areas for light-off. **(B)** Variant of VC assay with a temporal light gradient at the border (as opposed to a sharp transition). The ring-shaped area between the two dotted white circles is virtually defined as the transition zone: the illumination of the arena is spatially uniform at all times but changes in intensity while the fish is within the transition zone. When the fish is within the inner dotted circle, illumination is at the brightest; as the fish approaches the outer circle, the illumination dims, and gradually transitions into complete darkness when the fish reaches or is beyond the outer circle. Note that fish usually turns around before reaching complete darkness. **(C)** Larval zebrafish prefer light over real shadows (mostly temporal darkening). Upper left panel: the light source comes from below the arena, and a ring-shaped piece of material that blocks visible light (but transmits infrared light) is positioned under the arena, i.e. a strong shadow is created for the ring-shaped area. Lower left panel: trajectory of a fish over a session of 6 min. The fish mainly stays within the center circle of the dish where they can see the light source; when it crosses the border into the shadow area it quickly returns back to the circle. Insets show 3 trajectory segments (rotated into same orientation), direction indicated by the red, green and blue arrowhead, yellow dots mark the points where fish enters the shadow (crossing the border that is marked by dashed red line). Note similarity to the VC assay.

(Figure 2.2 continued)

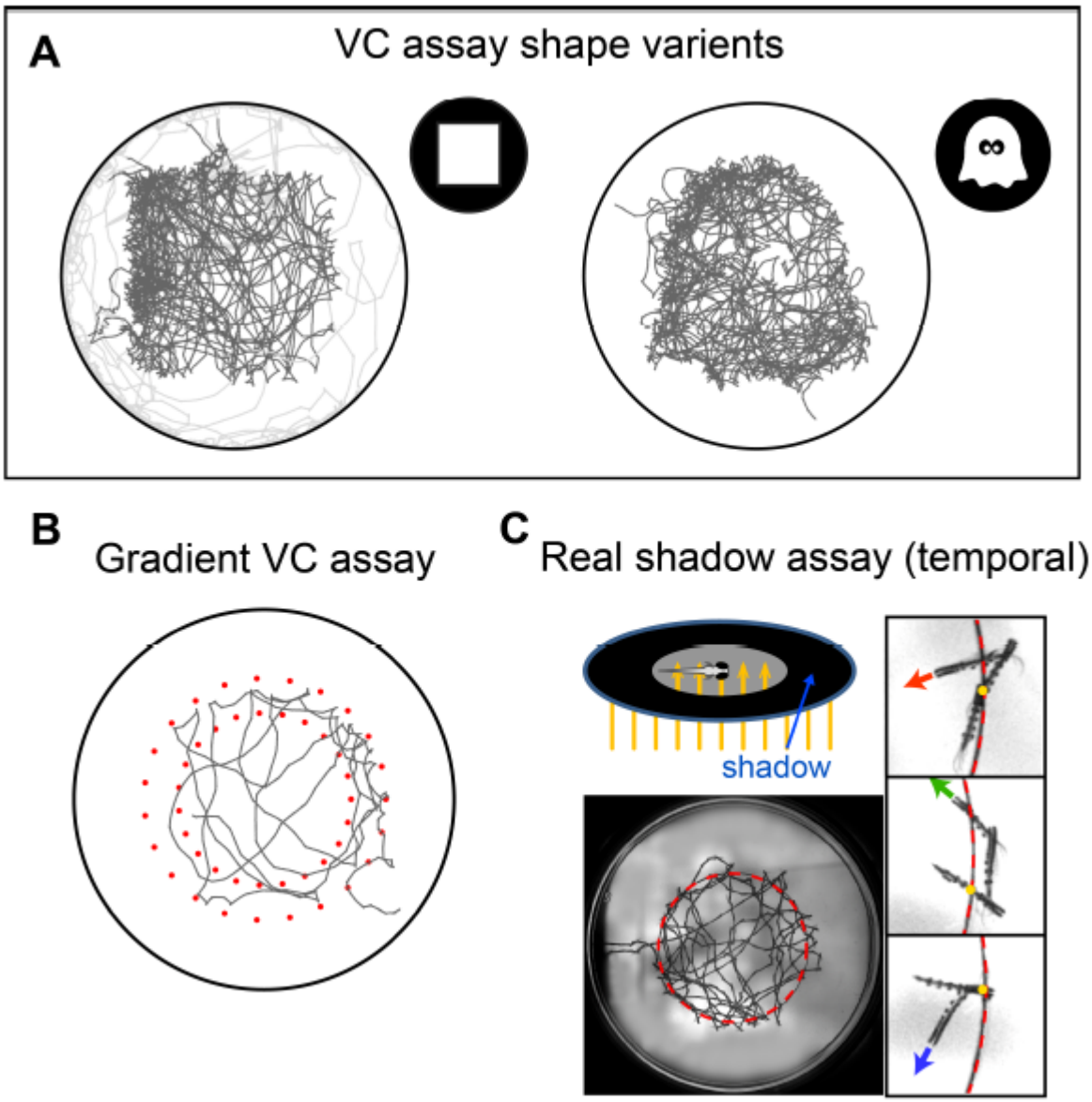

2.4 TURNING-ANGLE DISTRIBUTIONS IN LIGHT, DARK AND AT TRANSITIONS

In order to explain this remarkably high success rate, we examined the fish's navigation strategies by tracking the angles between successive bouts (turning angles). While in light (within the virtual circle), fish mostly swim forward or make small angle turns, whereas after a light-to-dark transition, the average turning angle is increased significantly (**Figure 2.3A**). Larval zebrafish are known to respond to a dark flash with a large-angle turn (Burgess and Granato 2007), but this single-step reflex alone does not ensure that they escape the dark area. If the fish is still in the dark after the first turn, subsequent turns are also important.

To investigate the fish's response over several turns, we summarized the turning angle distributions for each of several turns after light-to-dark or dark-to-light transitions for all fish (**Figure 2.3B**; 2 examples for single fish shown in **Figure 2.4B**). The results suggest that the determination of turning angle magnitudes is modified by the light-switching experience; the effect is strongest immediately after the switching and diminishes to baseline over at least 3 bouts.

The top histogram in yellow (left panel, first row) shows all turns performed in the light (n=30464), and serves as an estimate of the baseline swimming activity. The top histogram in purple (right panel, first row) shows all turns performed in the dark (n=10124). As noted previously, the first turn after the Light-to-Dark transition, labeled "LD1", is typically a large angle turn. Subsequent turns in dark, "LD2" and "LD3", are also large angle turns but their size decreases steadily (**Figure 2.3C**, purple line). Once the fish returns to the virtual circle, it must cease making large angle turns to avoid exiting it again. Indeed, the first turn after the Dark-to-Light transition, labeled "DL1", is smaller than turns in dark, but still slightly larger than

subsequent turns (**Figure 2.3C**, yellow line). Beyond 3 bouts in light or dark, turning angle magnitudes resemble those during baseline swimming activity (**Figure 2.3B,** bottom row).

We have thus described a set of relatively simple behavioral rules that modulates the turning angles directly based on the light transitions. We will henceforth refer to this set of rules as "Algorithm I [Angle]" to distinguish it from three further sets of rules which are discussed later. To test the functional relevance and contribution of these algorithms we built a simple computational model that allows us to test how much of the more complex features of the behavior these algorithms can explain.

Since larval zebrafish swim in discrete bouts, the model simulates the trajectory of a fish bout by bout. The dimensions of the simulated arena and virtual circle are designed to match the real VC assay. The displacement for a bout is approximately constant for real fish, and is held constant in the simulation. For each bout, the light state (on/off) is determined based on the updated position (in relationship to the virtual border in the simulation), and the turning angle of the next bout is determined by the algorithms.

This first version of the simulation implements Algorithm I [Angle], by drawing turning angles from different distributions depending on the light transitions. **Figure 2.3D** shows a representative sample trajectory each for the real fish and the simulation. To quantify and compare the degree that the fish trajectory is confined within the virtual border, we computed the average probability of the fish (real or simulated) returning to the light within 3 bouts (**Figure 2.3E**). A control simulation without specific algorithms is also performed, where all turning angles are drawn from a single generic turning-angle distribution (pooled from all turns from all fish). This control probability is only 0.05 ± 0.003 (mean ± SEM). With Algorithm I [Angle]

implemented, the probability reaches 0.64 ± 0.006, which is still significantly smaller than the probability in real fish (0.86 ± 0.02, as shown in Figure 2.1G).

Figure 2.3. Turning-angle distributions in the light, in the dark and at transitions.

(A) Turning-angle distributions from an example fish. Upper panel: all turns in light. Lower panel: the first turn after the Light-to-Dark transition (LD1) is usually a large angle turn. **(B)** Turning-angle distributions from all 32 fish, for bouts in light (left panel) and in dark (right panel). The top two histograms summarize all turns made in light (left) and in dark (right), respectively. "DL*n*": the *n*-th turn after a Dark-to-Light transition. DL4+: all subsequent turns in the dark. "LD": respective turns in response to a Light-to-Dark transition. Histograms framed in red correspond to the single-fish polar plots in (A). **(C)** Mean turning angle - after excluding center peaks - of the *n*-th turn after transitions, extracted from (B). **(D)** Example trajectories of real and simulated sessions (using Algorithm I [Angle], i.e. turning-angle distributions in B) for the Virtual Circle assay. Fish trajectory is shown in grey; dashed red circle marks the virtual border. Traces after the fish reached the edge of the arena and before it returned to within the virtual borders are not shown (see *Experimental Procedures*). **(E)** The average probability of returning to light within 3 bouts of exiting the virtual circle (similar to Figure 2.1G), compared between real fish (n=32), a control simulation ("ctrl", n=100) that implements a generic turning-angle distribution pooled from all turns, and the simulation (n=100). [Mean ± SEM, $p<0.001$ (paired t-test) for all pairs.]

(Figure 2.3 continued)

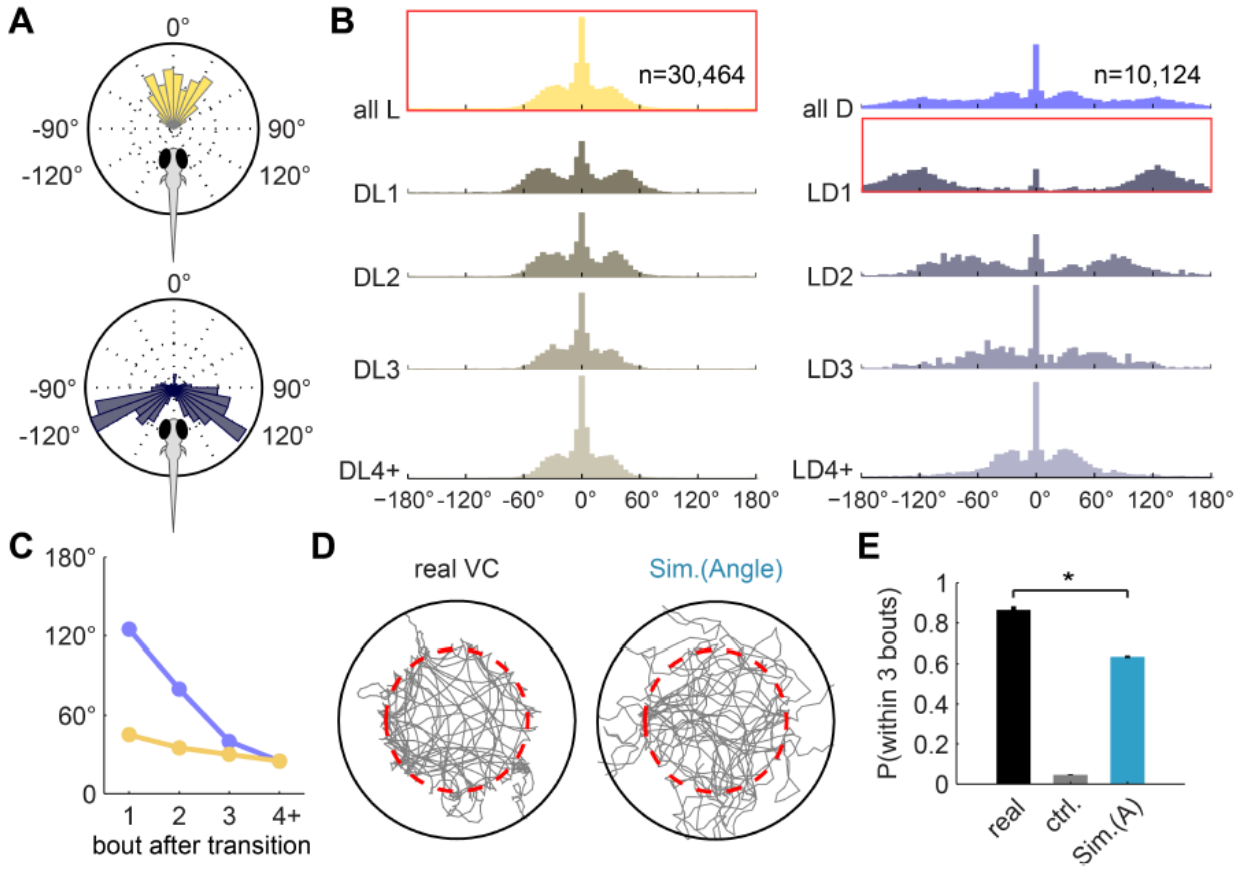

Figure 2.4. Supplementary analyses for Figure 2.3.

(A) Magnitude of turning angle of first turn after Dark shows slow decay over time. There is a decay of the response strength to Dark Flashes due to habituation. Most sessions were conducted for 15 min, but even towards the end of the longer sessions (30 min), on average the fish still responds with large angle turns to the onset of Dark Flashes. **(B)** Sample turning angles distributions for individual fish, compare to Figure 2.3B. 2 examples are shown in 2 rows, respectively.

(Figure 2.4 continued)

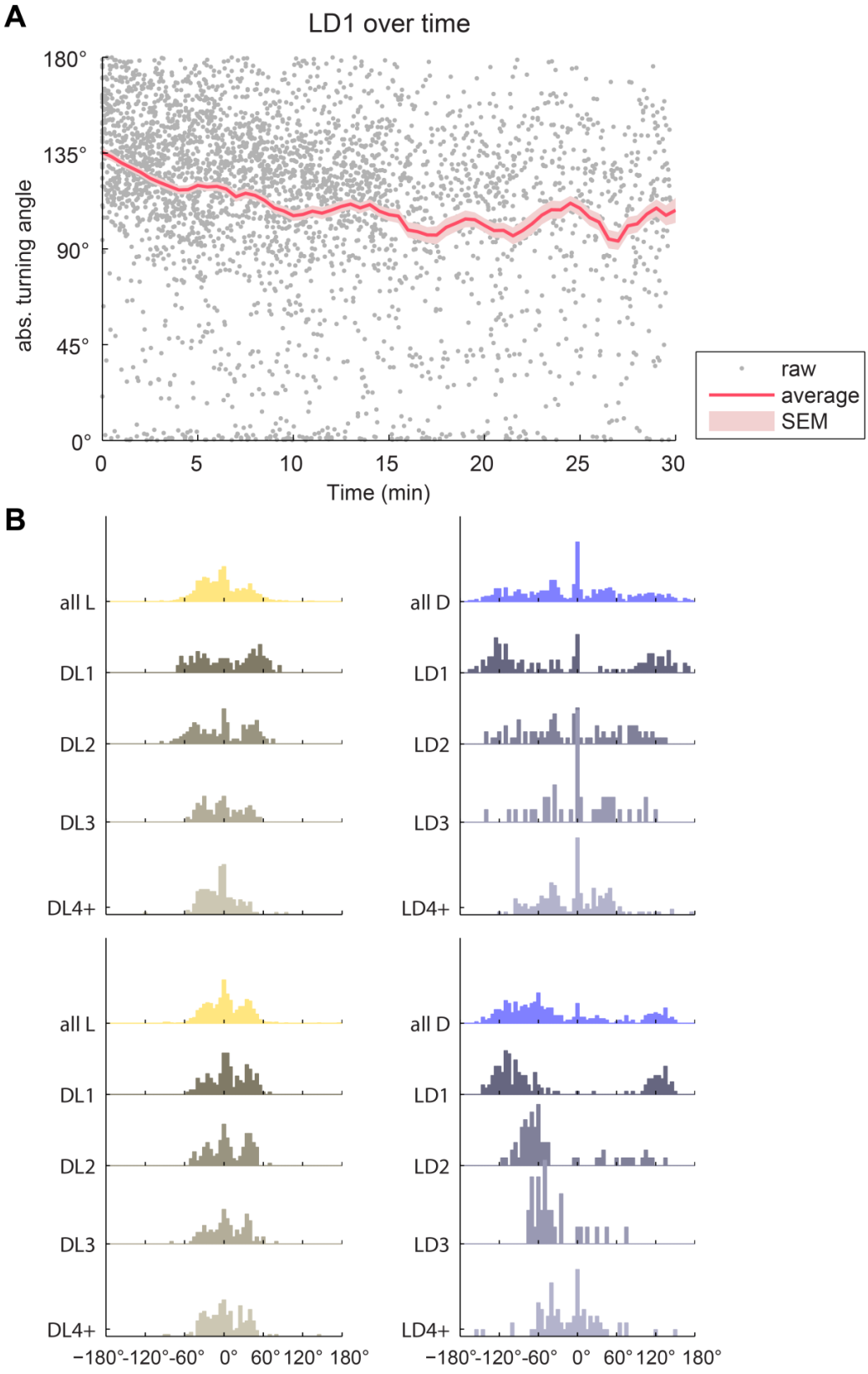

2.5 HISTORY-DEPENDENT TURNING MODULATION AROUND LIGHT TRANSITIONS

We have shown that a fish responds to a sudden decrease in light intensity with a large angle turn. If the first large-angle turn does not lead the fish back to the virtual circle, it continues to make turns of large magnitudes. But are there rules for the left/right direction of these turns? For example, do fish continuously turn in one direction to return to the virtual circle, or do they turn randomly? To answer these questions, we analyzed the dependence of turn direction on the recent turning history. We found that fish are more likely to turn in the direction opposite to the previous turn immediately after a light transition, and tend to turn in the same direction otherwise.

For our analysis, we plotted a series of turning correlation matrices for different categories of turns to evaluate the relationship between a given turn and the turn immediately preceding it. The matrices are heat-map presentations of data summarized for all fish, normalized such that each fish is represented equally. For a set of two consecutive turns, the angles of the first turn and second turn are mapped onto the horizontal and the vertical axes, respectively.

In order to quantify this correlation, we also define a "lock-index," which is positive for two consecutive turns in the same direction ("locked") and negative for two turns in opposite directions ("flipped"). The value of the lock-index can range from -1 to 1, with 1 standing for maximally "locked" (identical turning magnitudes in the same direction) and -1 for maximally "flipped" (identical turning magnitudes but opposite direction). **Figure 2.5A** maps the values of the lock-index onto a correlation matrix. The average lock-indices for each fish are summarized in a histogram displayed above each of the correlation matrices.

Figure 2.5B shows the correlation of all pairs of consecutive turns in light (left panel) and in dark (right panel). In light, fish mostly perform small angle turns; in dark, turns are frequently of larger angle, but in both cases, pairs of consecutive turns are mostly correlated or "locked", as also shown in the lock-index histograms on top of the matrices. We further examined the relationship between consecutive turns surrounding the light transitions (**Figure 2.5E-F**). Consider a sequence of events in which the fish leaves the border (into the dark) and then returns to the circle (back into light). (1), the turns spanning the Light-to-Dark transition (LD0 and LD1) are predominantly "flipped" (**Figure 2.5E**, left panel). (2), immediately after this Light-to-Dark transition, the first two bouts in dark (LD1 and LD2) are strongly "locked" large-angle turns (**Figure 2.5E**, right panel). (3), for the Dark-to-Light transition (**Figure 2.5F**), DL0 and DL1 are strongly "flipped", and (4), DL1 and DL2 are "locked". Effectively, it appears that the "lock" and "flip" turns could contribute to a fish staying close to the virtual border (as illustrated in **Figure 2.5K**). All together, we term these 6 groups of correlations between 2 consecutive turns "Algorithm II [Lock/Flip]".

To test whether these correlations depend on the shape of the virtual border, we conducted playback (Dark-Flash) experiments that essentially served as a yoked control for the VC assay. In the playback experiment, we deliver the temporal sequence of light transitions experienced by a fish in the VC assay to a different (naïve) animal. Specifically, we collected the statistics of light and dark durations that an animal experiences during the VC assay (**Figure 2.5D**), and draw from these two distributions to produce sequences of dark flashes to present to fish in the playback experiment (**Figure 2.5H**). In order to mimic the motion triggered nature of the VC assay, light changes are only delivered when the fish initiates a bout. Comparing the trajectories of the two experiments (**Figure 2.5C, G**), we observe that for playback, the locations

at which large-angle turns occur is distributed randomly in space, and unsurprisingly, the overall trajectory is not confined. However, the “lock” and “flip” matrices generated from playback experiments are indistinguishable - in direction as well as magnitude (**Figure 2.5I, J**) - from the VC experiment described in **Figure 2.5E, F** (magnitude is also shown separately in **Figure 2.6A**). Together, the playback data show that these history-dependent turning modulations are robust and most likely innate features, which exist regardless of the existence of the virtual border.

If Algorithm II [Lock/Flip] is added to Algorithm I [Angle] in the simulation, fish show an improved localization within the virtual border, which generates a much closer match to the statistics of real fish (**Figure 2.5L, M, N,** compare to **Figure 2.3D, E**). Nevertheless, Algorithm II [Lock/Flip] alone, in the absence of Algorithm I [Angle], does not contribute significantly to the fish’s performance (**Figure 2.6B-C**).

Figure 2.5. Turning modulation around light transitions.

(A) Value map of "lock-index" for correlation matrices (B, E, F, I, J). For a pair of consecutive turns, "locked" turns (2 turns in the same direction) populate the white diagonal (correlation), and "flipped" turns (2 turns in opposite directions) the black diagonal (anti-correlation). The lock-index ranges from -1 to 1, -1 being "flipped" (with identical turning magnitudes) and 1 being "locked". **(B)** Correlation matrices for consecutive turns, data pooled from all 32 fish. Left panel: all pairs of consecutive turns in light. Most are small angle turns, and fish have a small bias for "lock". Right panel: all pairs of consecutive turns in dark. Most large angle turns are "locked" in the same direction. Above each matrix: corresponding histograms of average lock-indices for each fish, calculated with (A). **(C)** Sample trajectory of Virtual Circle experiment. Traces after the fish reached the edge of the arena and before it returned to within the virtual borders are colored in light grey. **(D)** Distribution of duration of stimuli (Dark intervals or Light intervals, respectively), pooled from all fish. **(E, F)** Correlation matrices with corresponding histograms similar to (B), but for different specific categories of turns. **(E)** For 2 groups of turns around Light-to-Dark transitions, as indicated on axes. Note that the pair of turns surrounding the transition is "flipped", and the pair immediately afterward is "locked". **(F)** Similar to (E), but for turns around Dark-to-Light transitions. **(G-H)** Playback experiment: visual stimuli from VC assay (Dark Flashes) played-back to naïve fish (see text). **(G)** Sample trajectory of the playback experiment. **(H)** Actual distribution of stimuli duration of the playback experiment, from 27 fish. **(I, J)** Compare to (E, F), but from the playback experiment. The similarity to (E, F) indicates that the lock-flip tendencies do not depend on a specific geometry of the virtual border. **K,** Illustration of a model in which both "lock" and "flip" turns tend to lead the fish back towards the virtual border.

(Figure 2.5 continued)

L, Example session from a simulation (displayed as in Figure 2.3D) that implements both Algorithm I [Angle] (from Figure 2.3B) and Algorithm II [Lock/Flip] (from B, E, F). **M,** The average probability of returning to light within 3 bouts (expansion of Figure 2.3E). Compared between real fish (n=32) and the two simulations (n=100 each). Simulations are labeled by the algorithms implemented: "A" = Algorithm I [Angle], "LF" = Algorithm II [Lock/Flip]. [Mean ± SEM, $p<0.001$ (paired t-test) for all pairs.] **N,** Probability that a fish returns to light within *n* bouts, mean ± SEM plotted as a function of *n*, color-coded as in (M).

(Figure 2.5 continued)

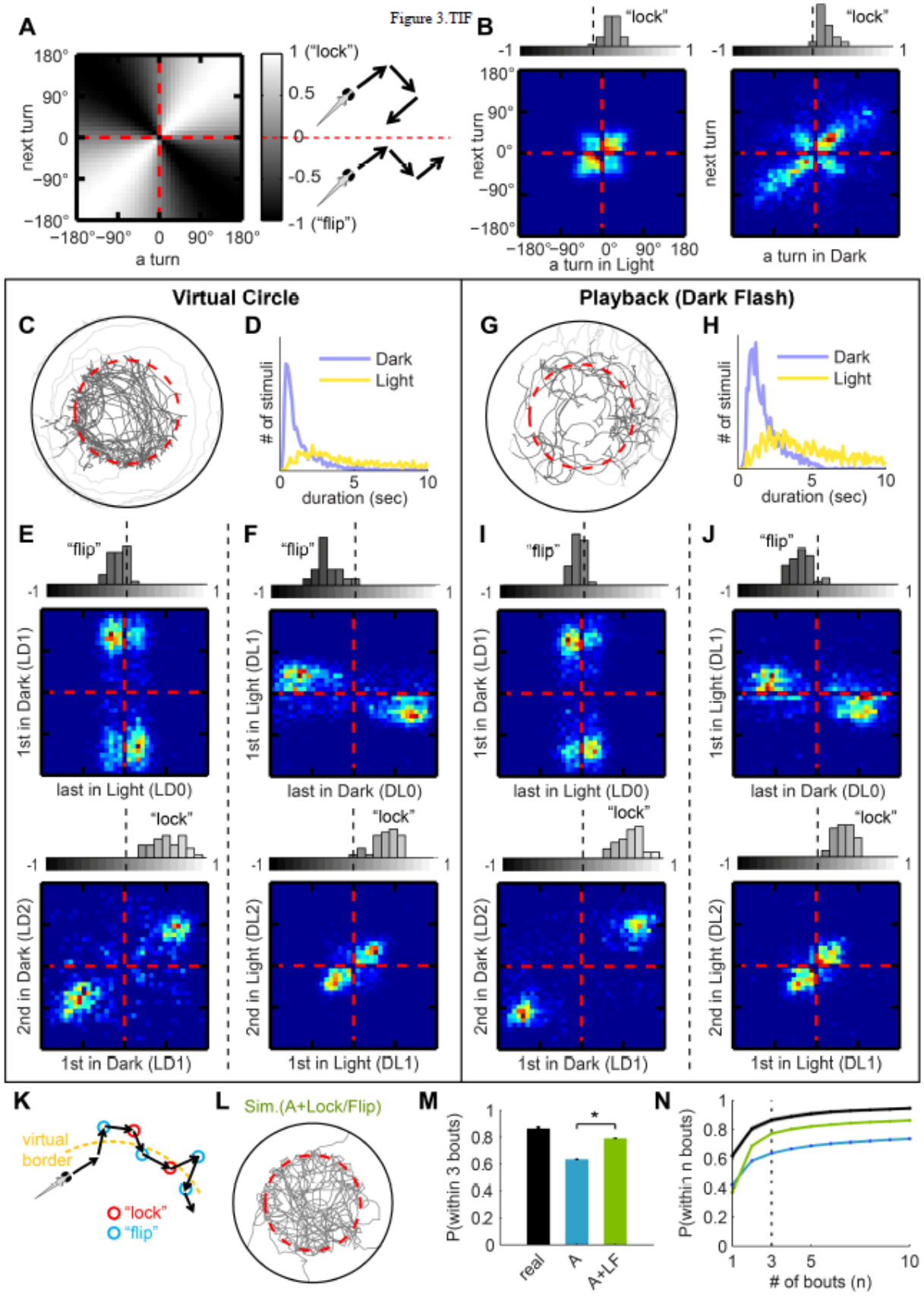

Figure 2.6. Supplementary analyses for Figure 2.5.

(A) Turning angle distribution from playback experiments; compare to Figure 2.3B. **(B)** Comparison of probability of returning to the virtual circle within 3 bouts, augmenting Figure 2.5L. We show a new simulation, "LF" (yellow bar), that implements the generic turning-angle distribution as in the **control** simulation, plus Algorithm II [Lock/Flip]. The resulting probability of returning within 3 bouts (0.07 ± 0.004, mean ± SEM) is barely higher than in the control simulation. This shows that Algorithm I [Angle] is necessary for later simulations incorporating Algorithm II. **(C)** Compare to Figure 2.5N, color-coded as in (B).

(Figure 2.6 continued)

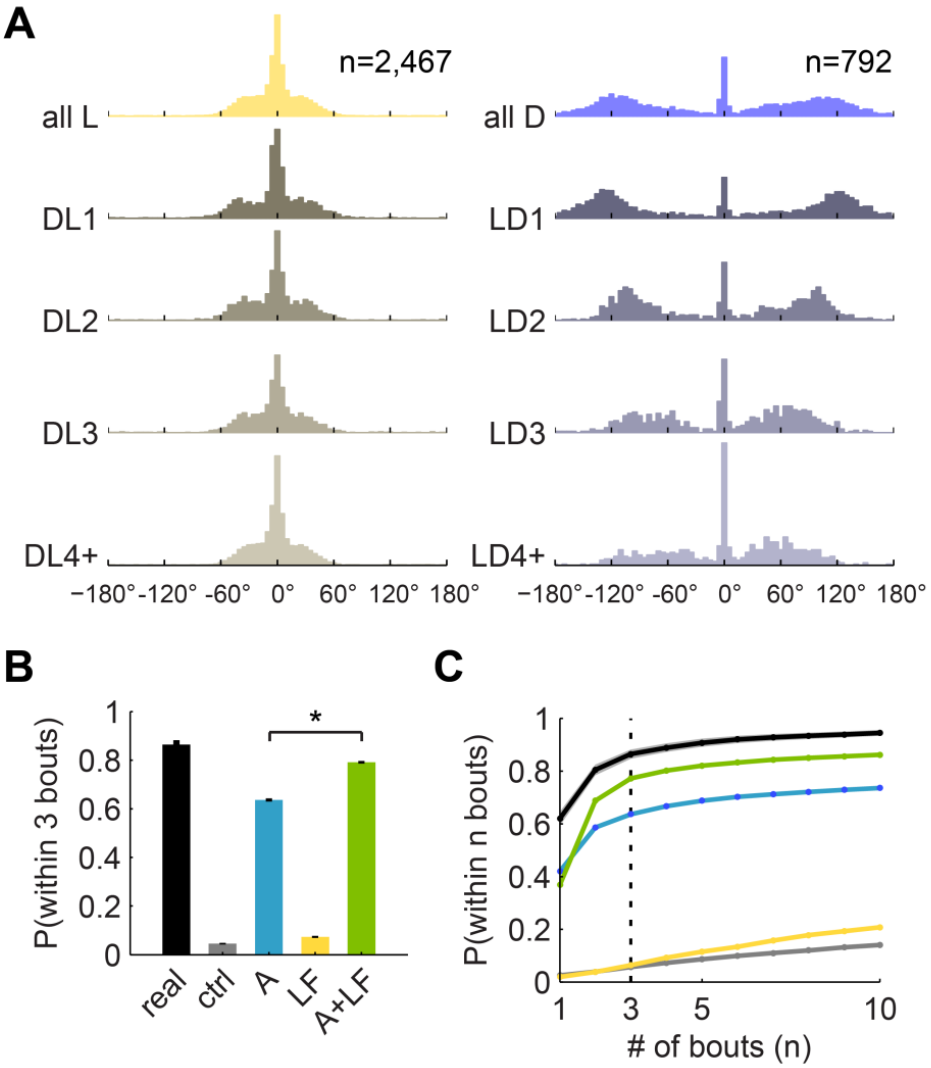

2.6 AFFINITY TO THE VIRTUAL BORDER CAN BE SIMULATED BY TURNING-ANGLE INTEGRATION

The pooled trajectories of the VC assay revealed a "border hugging" feature (**Figure 2.7A**) that was not captured by the simulation. The fish seems to repeatedly exit and enter the virtual circle as it navigates along the virtual border, almost as if it were "bouncing" off the border (highlighted blue trajectory segment). To quantify and compare this enhanced activity near the border, we first calculate the relative trajectory density near the virtual border (**Figure 2.7B**, first 3 bars). For real fish, this relative density at the border (1.14 ± 0.03, mean ± SEM, n=32) is significantly larger than expected from a uniform distribution (see **Figure 2.8A**). The density for the simulation with Algorithm I+II (0.95 ± 0.007, n=100) is slightly higher than for the simulation with Algorithm I alone (0.88 ± 0.007, n=100), but is still significantly lower than for real fish. We therefore searched for an algorithm that would recapture this high density at the border. We know that Algorithm I and II only use information of the previous one bout in the swimming history. Thus, we tested whether the inclusion of more than one bout in history leads to an improvement of the simulation.

As such, Algorithm III [Bounce] was inspired by analyzing the cumulative turning angle over all successive bouts between light transitions. For real fish, the cumulative angle turned over a given light interval is "flipped" in relation to the cumulative angle turned over the preceding dark interval (**Figure 2.7C**). This pattern is not well captured in the previous versions of the simulation (**Figure 2.7D, E**). In Algorithm III, each turn in light is therefore biased such that their cumulative angle approaches (with opposing sign) the cumulative angle of the preceding dark period. The implementation of Algorithm III resulted in a cumulative correlation

matrix that closely resembles that of real fish (compare **Figure 2.7F** and 2.7**C**). Importantly, in the presence of previous algorithms (**Figure 2.8C**), this simulation fully recaptures the "border-hugging" feature described in **Figure 2.7B** (last bar: 1.15 ± 0.008, mean ± SEM, n=100; trajectory shown **Figure 2.8B**).

Figure 2.7G gives an intuition for how the flipping of the cumulative angles leads to a trajectory that frequently crosses the virtual border: the underlying pattern is that the trajectory curve on one side of the virtual border is loosely mirrored on the opposite side. Also note that in the correlation matrix, the data points strongly cluster between the "flip" (anti-correlation) diagonal and the horizontal axis, demonstrating that as expected for a circle (instead of a straight line), the cumulative angle turned in light is usually slightly smaller in magnitude than in dark.

Figure 2.7. Affinity to the Virtual Border.

(A) Trajectory of a real fish, example trajectory segment highlighted in blue. Note that the trajectory density is much higher close to the virtual border (dotted red line). **(B)** Quantification of the relative bout density close to the virtual border, and comparison between real fish and different simulations. Simulations are labeled by the algorithms implemented: "A" = Algorithm I [Angle], "LF" = Algorithm II [Lock/Flip], "BO" = Algorithm III [Bounce]. Reference level (=1) is the normalized baseline bout density if the trajectory were uniformly distributed within the Virtual Circle. (Quantification see Figure 2.8A.) **(C-F)** Correlation between the cumulative angle turned during a light interval and during the preceding dark interval, again shown by matrices as in Figure 2.5B. **(C)** For real fish, strong **clustering** is shown close to the "flip" diagonal. **(D)** For the simulation with Algorithm I [Angle], there is no strong "lock"/"flip" bias. **(E)** In the simulation including Algorithm II [Lock/Flip], clustering in the "lock" quadrants is stronger than for real fish. **(F)** In the simulation including Algorithm III [Bounce], the simulated fish are constrained to match the "flip" pattern of real fish, and the resulting matrix confirms that the similarity to real fish is achieved. As shown in the last bar of (B), the addition of this algorithm restores the high bout density of real fish in the simulation. **(G)** Illustration of Algorithm III [Bounce]. If the fish exits the virtual border at approximately the same angle (relative to the border) each time, the fish may frequently cross the virtual border. That would require the heading direction of the two purple bouts to be approximately parallel, and the angle of the turn in dark (marked with the purple arc) should have equal magnitude but opposite direction as the sum of the 3 following turns in light (marked with orange circles).

(Figure 2.7 continued)

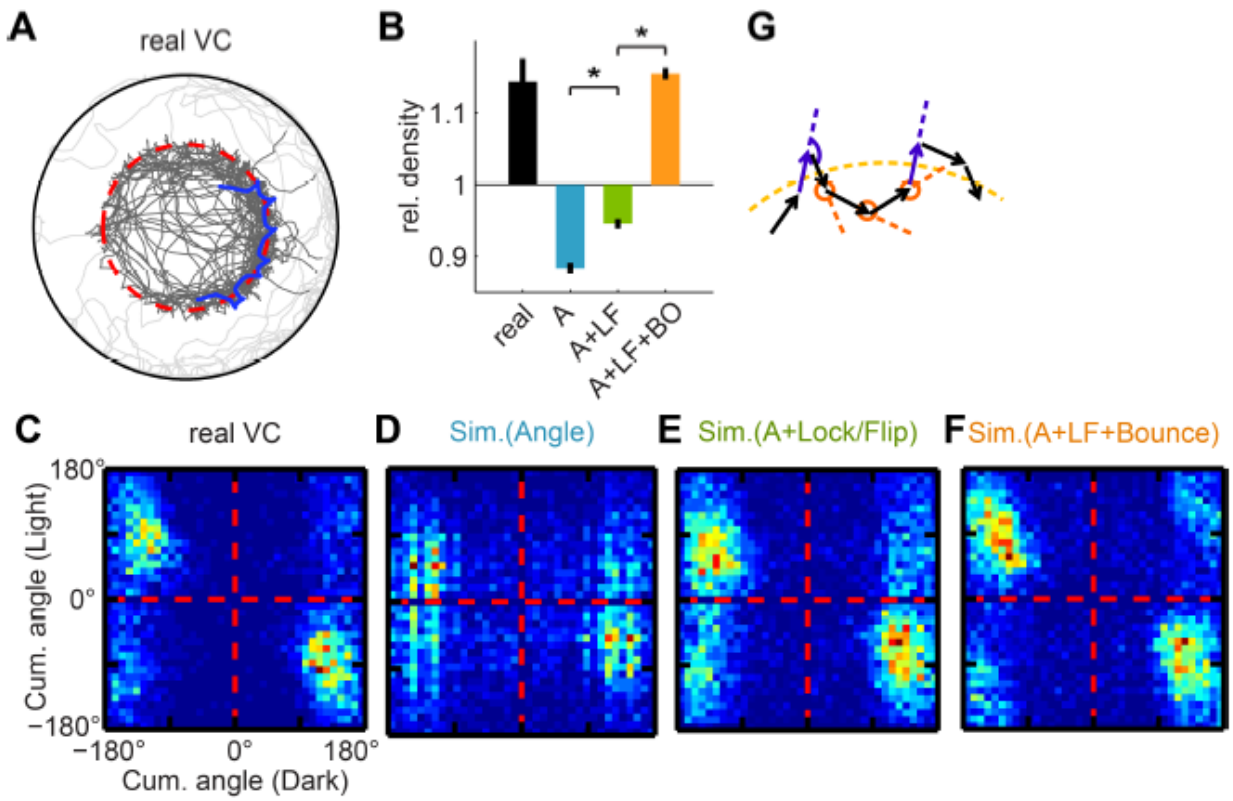

Figure 2.8. Supplementary analyses for Figure 2.7.

(A) Radial bout density for VC assay and simulations, supplementing Figure 2.7B. Horizontal axis: distance from center (radius), "R" notes the radius of the virtual border, "edge" the radius of the arena. Red line indicates the reference bout density as a function of radius, assuming uniform density of bouts within the virtual border and zero outside. The bout density ρ is defined for the cyan shaded range as the ratio of the simulated value (area in gray) to the reference value (area under red curve). To avoid systemic biases because of poor confinement to the virtual border (as in the simulation only with Algorithm I [Angle]), the bouts from trajectory segments where the fish did not return to the virtual border within 3 bouts are not included for this quantification. **(B)** Example trajectory of the simulation implementing Algorithm III [Bounce]. **(C)** Quantification of the relative bout density close to the virtual border, augmenting Figure 2.7B. Simulations are labeled by the Algorithms implemented. The purple bar shows that Algorithm II [Lock/Flip] still contributes significantly in the presence of Algorithm III [Bounce]. **(D)** Simulated relative density close to the virtual border, with the ratio of left versus right turns manipulated (this simulation includes Algorithms I and II, but not III). 0 on the horizontal axis indicates all turns are right turns, and 1 on the axis indicates an equal mix of left/right turns. Positive biases for left turns (values >1 on the horizontal axis) are symmetrical but not shown.

(Figure 2.8 continued)

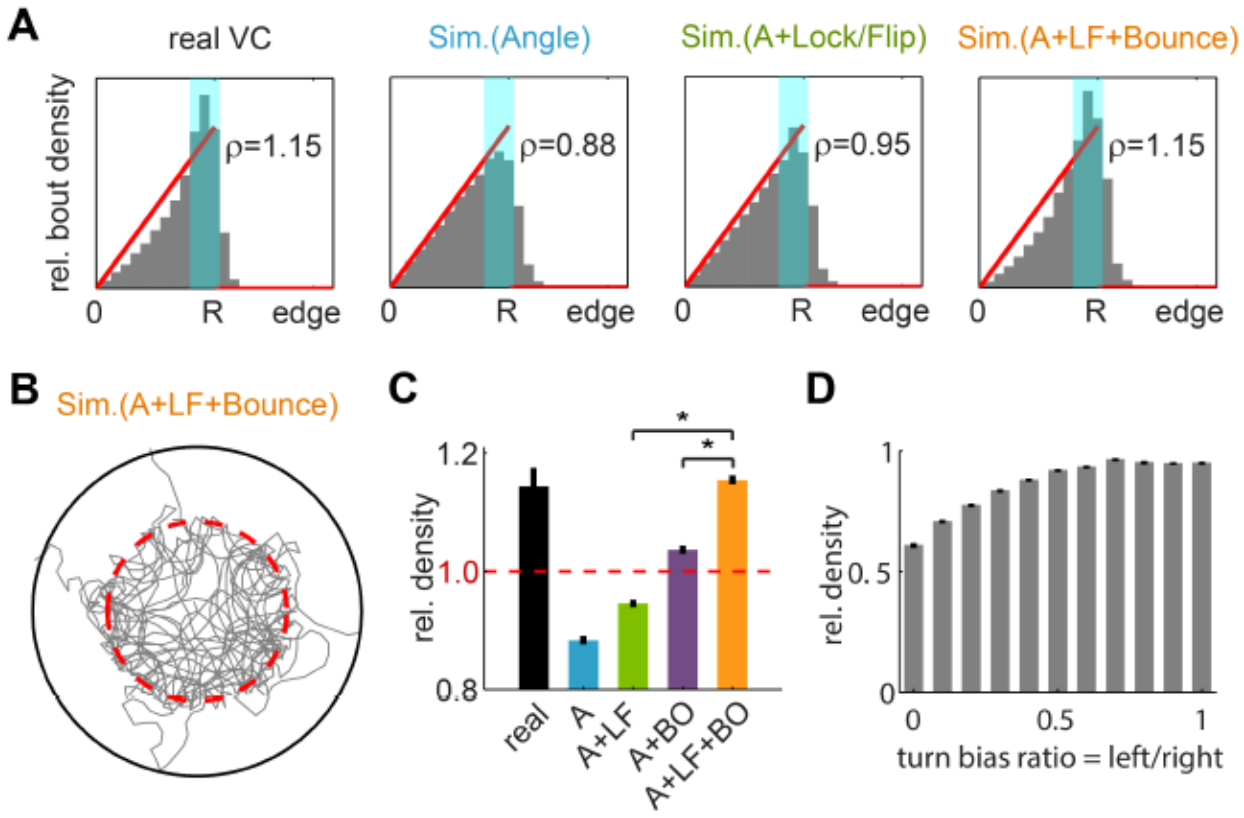

2.7 CHOICE OF EFFICIENT TURNING DIRECTION SUGGESTS SOPHISTICATED NAVIGATION ABILITY

If we only consider the first turn after the Light-to-Dark transition (LD1), in most cases, turning left or right is not equally efficient for returning to the virtual circle (**Figure 2.9A**). For a fish approaching the virtual border at an angle indicated by the blue arrow, we count a turn in the direction of the green arrow as an "efficient" turn, and one in the direction of the red arrow as an "inefficient" one. To quantify this "efficiency" for a given fish, we calculate the probability that an LD1 turn is in the "efficient" direction. Given that the virtual border is completely invisible to the fish, if the fish were to make turns in a random direction, the average "efficiency" would be 0.5.

To our surprise, we found that for the population of fish tested, fish turn into the "efficient" direction 70% of the time (**Figure 2.9B**, "efficiency" = 0.69 ± 0.02, mean ± SEM, n=32). In order to control for residual spatial visual cues as a possible explanation for this phenomenon, we designed a "Spotlighted Virtual Circle" experiment (**Figure 2.9C**). A white circle (the "spotlight") is projected onto the otherwise black screen and is always centered at the fish while the fish is swimming within the virtual border. Here again, the projector is turned off and the arena is left in complete darkness when the fish exits the border. We found that the probability of "efficient" turns is unaffected by these more stringent conditions (**Figure 2.9D**, 0.68 ± 0.02, mean ± SEM). Therefore, we can conclude that the fish is not informed by spatial visual cues in the VC assay to guide its behavioral choices.

The three algorithms described thus far do not reproduce this "efficiency" (**Figure 2.9E**, first 4 bars; mean ± SEM for Angle: 0.50 ± 0.007; Angle + Lock/Flip: 0.49 ± 0.005; Angle +

Lock/Flip + Bounce: 0.50 ± 0.005). Therefore we added another algorithm, Algorithm IV [Efficiency], to fully explain the observed behavior. In this algorithm, the strong tendency of fish to "flip" between the last turn in light (LD0) and the first turn in dark (LD1) is relaxed depending on the time spent in light (number of bouts executed) before this transition into dark. Indeed, we find that in real fish a "lock" or a "flip" is equally likely if the last interval in light lasted for many (>~10) bouts, a feature that is not captured by previous algorithms (**Figure 2.9F**). Intuitively, if the fish swam for a long time within the circle, it will approach the border at more random angles and a "flip" strategy is not likely to be more "efficient" than chance.

Algorithm IV did not offset the overall LD0~LD1 lock-index (as shown in the correlation matrix in **Figure 2.10A**), but its addition to the simulation resulted in a significant increase of the "efficiency" (0.59 ± 0.005, mean ± SEM, **Figure 2.9E**, last bar), which accounts for half of the difference between real fish and chance level. Additionally, we show in **Figure 2.10B** that Algorithm III contributes indirectly to the "efficiency" (the "efficiency" is compromised to 0.56 ± 0.006 in its absence). We also examined the lock-index trend for the 2 bouts around the entry to the light, and there was no significant dependence on the length of the preceding dark interval (**Figure 2.10C**).

One additional explanation for this surprising ability of the fish to turn into the correct direction might be that the fish - by dead reckoning - accumulates information about the actual location of the virtual circle throughout the assay and then uses this information to gradually improve efficiency. In order to test this hypothesis, we compared the fish's performance at the very beginning of the VC assay with its overall performance. The efficiency calculated from the first two minutes of each session (0.72 ± 0.02, mean ± SEM; **Figure 2.10D-F**) is already indistinguishable from the overall value. This suggests that while the fish must integrate some

simple information about the recent swimming history to make efficient choices, it is not required for the animal to form a spatial representation of the virtual circle.

Figure 2.9. Choice of efficient turning direction suggests sophisticated navigation ability. **(A)** Illustration of "efficient" versus "inefficient" turns. For a fish approaching the virtual border (dashed yellow line) along the direction indicated by the blue arrow, in order to return to the light, a turn in one direction (green arrow) is more "efficient" than in the other direction (red arrow). Dashed black line: radial direction. **(B)** Histogram of the per-fish "efficiency", summarized for all fish in the VC assay. The 50/50 probability (pure chance) is indicated with a dashed red line. The dashed cyan line marks the mean of the distribution (0.69 ± 0.016, mean ± SEM, n=32). **(C)** "Spotlighted" Virtual Circle experiment, to control for potential asymmetries in the visual field that can be used as visual cues. The projected spotlight is centered at the fish at all times, except when the fish exits the virtual border (dashed red line) and the light is turned off. **(D)** Histogram of the per-fish "efficiency", for 30 fish from the "Spotlight" Virtual Circle experiment. The mean of this population (0.68 ± 0.016, mean ± SEM, n=30) is unchanged compared to (B). **(E)** The average "efficiency" compared between real fish and different simulations. Simulations are labeled by all the algorithms implemented: "A" = Algorithm I [Angle], "LF" = Algorithm II [Lock/Flip], "BO" = Algorithm III [Bounce], "E" = Algorithm IV [Efficiency]. Dashed red line indicates the value of pure chance. None of the first 3 simulations (blue, green and orange) produce an "efficiency" that is statistically different from chance. Only the simulation applying Algorithm IV, as described in (F), enhances the "efficiency" significantly to 0.59 ± 0.005 (mean ± SEM). **(F)** The lock-index for the last turn in light (LD0) and first turn in dark (LD1), plotted as a function of the length of the immediately preceding interval in light. Note that for the previous simulations, the lock-index does not change significantly with the length of the preceding light interval. For the simulation with Algorithm IV [Efficiency], the turning direction of the first turn in dark (LD1) is constrained so that this lock-index curve (in red) mimics the curve from real fish (in black).

(Figure 2.9 continued)

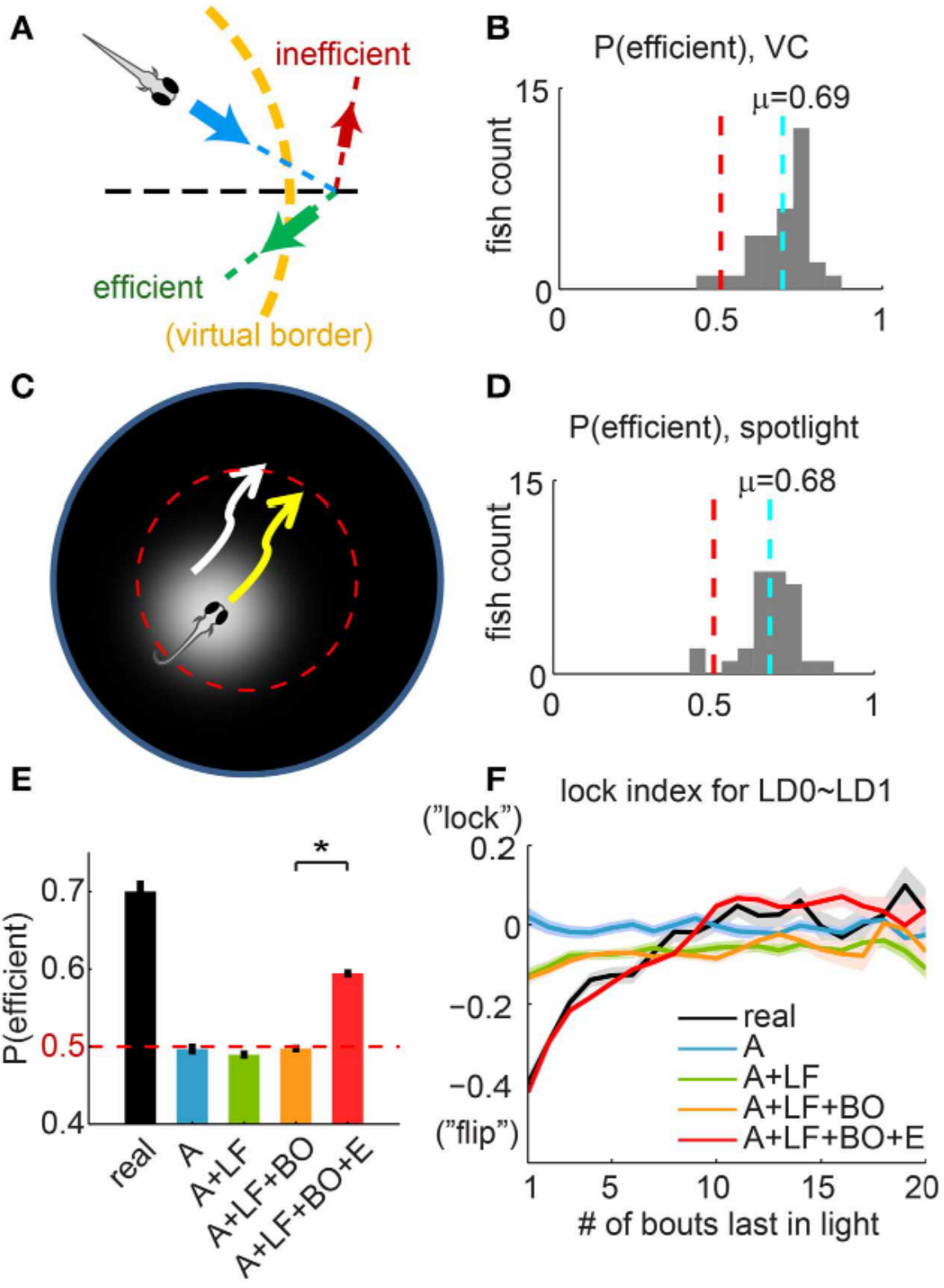

Figure 2.10. Supplementary analyses for Figure 2.9.

(A) Correlation matrix of LD0~LD1 for the simulation with Algorithm IV [Efficiency] is very similar to the matrix from real fish (Figure 2.5(E) first panel). **(B)** The average "efficiency" compared between real fish and different simulations, augmenting Figure 2.9E. Since Algorithm IV [Efficiency] depends on the "flip" of LD0~LD1, Algorithm II [Lock/Flip] is not permutated separately from Algorithm IV. The brown bar suggests that even though Algorithm III [Bounce] is not sufficient to enhance the "efficiency" alone, it still contributes significantly in the presence of Algorithm IV. **(C)** Similar to Figure 2.9(F) but for DL0 (last turn in dark) versus DL1 (first turn in light). No significant change is seen in the real fish (black curve), and matching the black curve better (red curve) does not have significant effects on the simulation. **D-(F)** Data analyzed for only the first 2 minutes from all VC sessions. [For first 2 min of each session, P(within 3 bouts) = 0.96±0.01, mean±SEM, not shown in figure.] **(D)** Turning angle distributions in light (left) and dark (right); compare to Figure 2.3B. **(E)** Correlation matrix of cumulative angles; compare to Figure 2.7C. **(F)** Histogram of the per-fish "efficiency" (0.72 ± 0.02, mean ± SEM), compare to Figure 2.9B.

(Figure 2.10 continued)

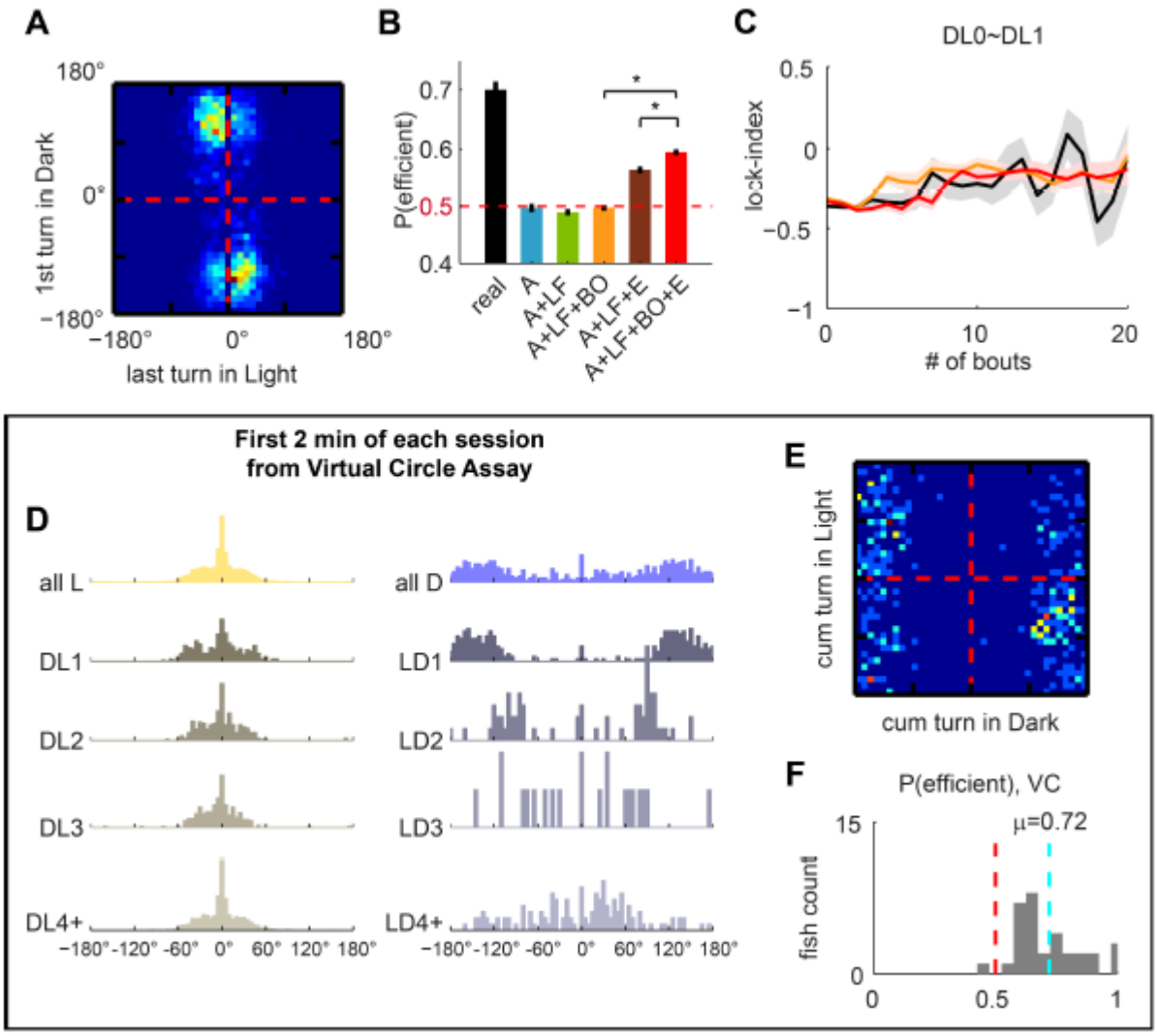

2.8 DISCUSSION

To the best of our knowledge, this is the first study to explore the temporal aspects of phototaxis in the larval zebrafish. Here we extract a series of simple temporal algorithms that explain most of the animal's behavioral statistics. These algorithms range from hard-wired turning modulations to temporal integration strategies that suggest advanced navigation abilities. We were able to extract these algorithms due to two key features of the Virtual Circle assay. First, the visual input is a series of binary events (Light/Dark) in time; in other words, the visual information is encoded purely temporally, as it is spatially uniform at all times. Second, larval zebrafish swimming can be described in discrete bouts, which enables us to describe the algorithms in discrete behavioral units.

The visual input does not provide direct spatial information, yet the fish can avoid dark areas in space; therefore the fish must rely on temporal integrations, i.e. some form of memory, to implement the 4 behavioral algorithms discussed in Figure 2.3, 2.5, 2.7 and 2.9, respectively. Here we summarize the 4 memory requirements for the VC assay in **Table 1**. *(1) Time since light transition.* The first memory requirement is the retention of light-switching events. For the turning-angle distributions (Algorithm I), the effect of the light switches lasts over several bouts (bout frequency is ~1 per second). For Algorithm IV, which enhances the efficiency, the gradual decay of the "flip" tendency for the first turn in Dark suggests retention of the light-switching event over up to 10 bouts (~10 sec). *(2) Direction of last turn.* Larval zebrafish are able to retain the turning direction of the previous turn to inform the choice of direction of the present turn. This is supported by Algorithm II, the lock/flip correlation of the turning angles of two

consecutive turns. Algorithm IV [Efficiency] also depends on this memory requirement, since it is based on the "flip" around the light-off transition. *(3) Cumulative angle.* This form of memory is required by Algorithm III [Bounce], which ensures that the cumulative (total) angle made in a light interval is similar in amplitude (but in the opposite direction) as the cumulative angle in the preceding dark interval. *(4) Higher order (spatial processing).* In Figure 2.9, the unexpected "efficiency" of the fish in returning to the virtual circle is only partially explained by simulations using relatively simple algorithms. The unaccounted part of the "efficiency" may invite thoughts on path integration (Müller and Wehner 1988) or spatial memory, but a more likely scenario would be one that involves additional simple algorithms of the sort described in this study.

Table 1. Summary of behavioral Algorithms and the corresponding memory requirements.

Algorithms / Memory Requirements	I [Angle] (Fig.2.3)	II [Lock/ Flip] (Fig.2.5)	III [Bounce] (Fig.2.7)	IV [Efficiency] (Fig.2.9)
Time since light transition	●			●
Direction of last turn		●		●
Cumulative angle			●	
Higher order (spatial				●

Under natural conditions, fish will usually not experience sharp step functions in light intensity. Rather, transitions are likely to be of a more gradual nature. To test whether this would affect the general features of the behaviors described here, we implemented temporal light

gradients that may better represent natural light stimuli. In this gradient version of the VC assay, the uniform illumination dims gradually as the fish approaches the virtual border. We find that here also fish exhibit general turning behavior that results in high occupancy within the virtual border (**Figure 2.2B**). This serves as a proof of principle that larval zebrafish can use broadly effective temporal navigation strategies for temporal gradients of varied steepness. In addition, we show that a real ring-shaped shadow (as compared to a virtual one), also confines the fish to the center area in a very similar way (**Figure 2.2C**).

For isolated dark flashes in larval zebrafish, Burgess et al. reported turning angles of 150°±30° (mean ± S.D.) (Burgess and Granato 2007), while for our VC assay, the LD1 turning angles are 113°±42°, significantly smaller in magnitude. However, in the VC assay, dark flashes occur more frequently (averaging once every ~8 seconds) than in Burgess et al., which might result in habituation effects that could explain this discrepancy (**Figure 2.4A**). Indeed, when we analyze the initial response strength in the VC assay we find that these turns show no difference to those reported by Burgess et al. (144°±31° for the turn after the first dark flash for each session, mean ± S.D.).

Upon closer inspection of **Figure 2.3B**, we also observe a trimodal distribution of turns in light: slightly left, straight forward, and slightly right (Figure 2.3B left column). Given the lack of directional stimuli in our assay, this swimming pattern may support a locomotion control model that distinguishes a forwards swimming mode from a turning mode (Huang et al. 2013).

For most of this study, we presented pooled data from all animals, and one may question whether individual left/right turning biases may contribute to features like the “border hugging”. We therefore manipulated the left/right bias of all turns in a simulation (that includes Algorithms

I, II but not the “Bounce” Algorithm III). We found that while a turning bias of medium strength does not affect the bout density at the border, a strong bias actually decreases this density (**Figure 2.8D**), which argues against individual left/right biases being an underlying cause.

Fernandes et al. (Fernandes et al. 2012) described a related light-seeking behavior in blind zebrafish larvae via deep brain photoreceptors as “an undirected hyperactivity in darkness, which results in the aggregation of organisms into a lit area”, and termed it “dark photokinesis”. This finding begs the question of whether the temporal phototaxis in our study could result from such simple diffusional trapping. The main argument against that is that undirected hyperactivity in darkness is a highly inefficient method for light-seeking, an observation confirmed by the analysis of Fernandes et al.. In contrast, the phototactic behavior observed in our experiments shows remarkable efficiency that requires more complex rules.

Most of the behavioral features that emerged out of the VC assay serve to better avoid darkness, but the enhanced activity close to the virtual border (**Figure 2.7**) seems to be an exception and calls for a novel explanation of its adaptive advantage. We speculate that this frequent crossing of the border is of exploratory nature, and can help an animal to escape from the confinements of aversive stimuli (shadows). Such exploratory tendencies are well recognized in other animals; in rodents for instance, an increase of exploratory behavior is used as an indicator of decreased anxiety (Crawley 1985).

The majority of the temporal algorithms discovered in larval zebrafish are likely innate, as opposed to learned. The playback experiments (**Figure 2.5G-J, Figure 2.6A**), as well as the lack of performance improvement over time within one session (**Figure 2.10F**) strongly support this notion. Furthermore, we used very young animals (5-7 days old), and although they already

demonstrate a rich repertoire of behaviors, associative learning for 5-day-old larvae is very difficult at best. This suggests that these temporal strategies are not shaped by experience and that fish employ these very same strategies in navigating their habitat around natural shadows.

Finally, the larval zebrafish is well suited to further dissect these kinds of behaviors at the neuronal level (Portugues and Engert 2009; Friedrich, Jacobson, and Zhu 2010; McLean and Fetcho 2011) since it lends itself readily to whole-brain functional imaging at single-cell resolution (M. B. Ahrens et al. 2012; M. Ahrens et al. 2013) and optical monitoring and manipulation of neural activity in a behaving animal (Douglass et al. 2008; Orger et al. 2008; Arrenberg, Del Bene, and Baier 2009; Wyart et al. 2009; Chow et al. 2010; Schoonheim et al. 2010; Warp et al. 2011; Akerboom et al. 2012; M. B. Ahrens et al. 2013).

2.9 Material and Methods

2.9.1 Fish and Behavioral Setup

Wild-type zebrafish (*Danio rerio*, WIK strain) larvae 5-7 days-post-fertilization are used for the free-swimming experiment. Experiments are conducted on single fish during daytime hours. The entire experimental setting (not including the computer) is enclosed in a light-tight rig. The circular arena is made of a standard (transparent) petri dish 100mm in diameter, with the side walls taped black (to reduce thigmotaxis, i.e. the preference for walls). White light from a Dell DLP projector is projected from below onto a diffusive screen placed directly under the dish, although for the original Virtual Circle experiments a white LED which provides even illumination was used. The screen and dish are illuminated with infrared from below. For Figure 2.1A and Figure 2.2C, images were captured with an infrared-sensitive CMOS camera (Mikrotron, MC1362) at 30 Hz, and the minimum intensity projections of fish trajectories are

shown (on smoothened background image). For all other experiments, we used a different infrared-sensitive high-speed camera (AVT Pike F-032) that captures the motion of the fish at 208 frames per second. A custom program written in C# was used for all behavioral experiments. Online tracking of the location and heading direction of the fish was employed for both the administration of closed-loop experiments and data recording. For the playback experiments, online bout-determination uses the same method as in data analysis as shown in Figure 2.1E (thresholding the change of heading direction).

Fish were reared on a 14/10 hr light/dark cycle at 28°C. Animal handling and experimental procedures were approved by the Harvard University Standing Committee on the Use of Animals in Research and Training (Cambridge, MA).

2.9.2 Behavioral Assays

2.9.2.1 "Virtual Circle"

The virtual border is defined as a circle of half the radius of the dish and concentric with the dish; it is only implemented in the programming code and is invisible to the fish. The light is on and only is on when the location of the fish (determined by automatic online tracking) is within the borders. (Light on: uniform white projection onto a circular area that is larger than the arena; Light off: instead of projecting "black" from the projector, the LED's in the projector are turned off, so the arena is in complete darkness.) Before a session start, fish are transferred to the arena and are allowed to adapt for 10 min. A fish at the edge (side wall) of the dish may spend a significant amount of time along the edge (thigmotaxis); therefore, when the fish swims out of an "exit line" very close to the edge (defined in the computer and invisible to the fish), the lights are turned on, and the experiment would be paused. The experiment resumes again when the fish

swims back to the center (within an "entry line" that is defined within the virtual border). Trajectory during pauses are not analyzed. Each fish is tested for a session of 15 min or 30 min in length including pausing time (n=32 fish).

2.9.2.2 "PLAYBACK" DARK FLASHES

The duration of the intervals in light, and intervals in dark, respectively, are pooled from all fish in the VC assay into 2 corresponding probability distributions. For the Playback experiments, we draw from these two distributions alternatingly, to produce a sequence of Dark Flashes alternating with light intervals to present to naïve fish. To mimic the feature that in the VC assay, light switches only occur when the fish is moving, we also perform online bout-determination in the Playback experiments, and the light switches are only triggered when the fish is making a bout. More specifically, we extracted from the VC data that on average, a light switch is triggered 50 milliseconds after a bout-start is determined online, so we subtract 50 milliseconds from every interval in the sequence produced for the Playback experiments, and during the experiment, the light switches are triggered 50 milliseconds after a bout-start is determined. Effectively, the Playback experiment serves as a "yoke" control to the VC assay; collectively these fish receive the equivalent visual input as the fish in the VC assay (same duration/frequency of Dark Flashes but shuffled).

Similar to the VC assay, when fish reach the edge of the arena, the experiment is paused, and we use a visual projection to encourage them to return to the center of the arena: a white circle (on black background) is projected to the center of the arena to attract the fish by phototaxis. This phototaxis attraction is not necessary for the VC assay as they rarely come to the

edges, but in the Playback experiment it happens so often that without this attraction, the average interval between Dark Flashes may be too long to compare with the VC assay.

2.9.3 Data Analysis

All data analysis was performed with custom code written in MATLAB, Mathworks (code available in Supplementary Material). For bout determination (Figure 2.1C), the threshold is determined empirically. For the turning angle distributions in Figure 2.3B, all histograms are normalized to have the same area - regardless of sample size for the different categories. The sample sizes for the categories “all L”, “DL1”, “DL2”, “DL3”, “DL4+” are 30464, 3386, 3234, 2878, 20974, respectively, and for “all D”, “LD1”, “LD2”, LD3”, “LD4+” are 10124, 3386, 1292, 658, 4788, respectively.

The correlation matrices in Figure 2.5 are normalized to represent each fish equally. The lock-index is calculated similar to a dimensionless correlation value. For a single pair of consecutive turns, lock-index = $x \cdot y \cdot 2/(x^2+y^2)$, where x, y are the turning-angles of the 2 turns, respectively. The value map shows the lock-index of all combinations of two binned turning-angles in grayscale in a 2D array. The lock-index reaches its minimum and maximum (-1 and 1) when the amplitudes of the 2 turning angles are identical. For Figure 2.8A, the calculation of the density at the border is based on all trajectories but the segments where the fish gets “lost”, because if the fish leaves the virtual circle frequently (as in the “basic” simulation), the density at the border is naturally diluted compared to a fish that is tightly confined within the virtual circle. For this calculation, trajectory segments where the fish doesn’t return to the virtual border within 3 bouts are excluded, for the data from real fish as well as the 3 simulations.

2.9.4 Simulation

All simulations are custom written in MATLAB (source code available in Supplementary Material). Since larval zebrafish swim in discrete bouts, we constructed a discrete model that simulates the trajectory of a fish bout by bout. The dimensions of the simulated arena and virtual circle are designed to match the real VC assay. The displacement for a bout are approximately constant for real fish, and is hold constant in the simulation. The simulated fish starts in the center of the simulated arena (within the virtual border), and a heading-direction is randomly assigned. Then for each bout, light on/off is determined based on the updated position (in relationship to the virtual border in the simulation); the turning angle of the next bout is determined by algorithms as described below. If the fish reaches the outer bound of the arena, the simulation "restarts" from a random location within the virtual border. For each set of parameters, the simulation is performed for n=100 sessions.

Mainly, 4 progressive versions of simulations have been performed: the "basic", "lock-flip", "bounce" and "efficient" version, respectively. Except for the "basic" version, each simulation is based on the previous version, only with new algorithms added.

The "basic" version, implementing Algorithm I, only uses the gray-shaded turning angle distributions from Figure 2.3B (without any history-dependent modulations). For each bout, first the program determines which category this bout belongs to (e.g. "first turn after light-on", or "beyond 4^{th} turn after light-off"), then draws an angle from the corresponding probability distribution (corresponding normalized histogram).

The "lock/flip" version, implementing Algorithms I+II, incorporates the "lock/flip" patterns from Figure 2.5B, E, F. Given a bout in the "lock/flip" simulation, the signed turning angle of the next bout is obtained by drawing randomly from the marginal probability

distribution (given the turning angle of the current bout) from the probability matrices obtained by normalizing Figure 2.5B, E, F.

For the “bounce” version, implementing Algorithm I+II+III, the cumulative angle turned in a dark interval is calculated after the fish re-enters the circle, and as the trajectory is simulated bout by bout in the light, the cumulative angle turned in light is kept updated, and the direction of the next turn is adjusted to approach the desired angle – the cumulative angle turned in dark but with reverse sign. Only the direction and not the magnitude of the turns are adjusted, so this does not affect the turning angle distributions; and only the turns at least 3 bouts after the Dark-to-Light transition are adjusted, so this also does not violate the Algorithm II [Lock/Flip].

For the “efficient” version, implementing Algorithm I+II+III+IV, the only addition is an array of probabilities that modifies the probability of LD0~LD1 flipping as a function of the preceding light interval length. This probability array is manually adjusted to fit the equivalent probability array for the VC assay (Figure 2.9F).

To be more specific, to implement Algorithms III and IV, (1) the angles were preliminarily determined only using Algorithms I+II; (2) then the left/right direction is either flipped or unchanged. In Algorithm III, step (2) assigns the direction so that the new turn is always (probability of 1) in the direction that favor the cumulative angle to approach (with opposing sign) the cumulative angle of the preceding dark period. In Algorithm IV, step (2) assigns the direction so that the new turn would be a "LD0~LD1 flip" with a probability that is equal to the corresponding probability from real fish (implemented in the code is essentially a 1-dimensional array of probabilities, as a function of time spent in light, taking the values as the red curve in Figure 2.9F).

2.10 ACKNOWLEDGMENTS

We would like to thank A.F. Schier and J.R. Sanes for valuable comments on the manuscript, Tim Dunn for sharing the behavioral tracking code, Leung-Hang Ma, Ruben Portugues and other members of the Engert laboratory for helpful discussions, and Aaron Kuan for numerous discussions and comments on the manuscript. This work was supported by NIH Grants awarded to F. E. (5R01DA030304-02 and 1DP1OD008240-01).

2.11 REFERENCES

Ahrens, MB, MB Orger, DN Robson, JM Li, and PJ Keller. 2013. "Whole-Brain Functional Imaging at Cellular Resolution Using Light-Sheet Microscopy." *Nature Methods* (March). doi:10.1038/NMETH.2434.

Ahrens, Misha B, Jennifer M Li, Michael B Orger, Drew N Robson, Alexander F Schier, Florian Engert, and Ruben Portugues. 2012. "Brain-Wide Neuronal Dynamics During Motor Adaptation in Zebrafish." *Nature* 485 (7399) (May 24): 471–7. doi:10.1038/nature11057.

Ahrens, Misha B., Kuo Hua Huang, Sujatha Narayan, Brett D. Mensh, and Florian Engert. 2013. "Two-Photon Calcium Imaging During Fictive Navigation in Virtual Environments." *Frontiers in Neural Circuits* 7 (June). doi:10.3389/fncir.2013.00104.

Akerboom, J., T.-W. Chen, T. J. Wardill, L. Tian, J. S. Marvin, S. Mutlu, N. C. Calderon, et al. 2012. "Optimization of a GCaMP Calcium Indicator for Neural Activity Imaging." *Journal of Neuroscience* 32 (40) (October 3): 13819–13840. doi:10.1523/JNEUROSCI.2601-12.2012.

Arrenberg, Aristides B, Filippo Del Bene, and Herwig Baier. 2009. "Optical Control of Zebrafish Behavior with Halorhodopsin." *Proceedings of the National Academy of Sciences of the United States of America* 106 (42) (October): 17968–73. doi:10.1073/pnas.0906252106.

Brockerhoff, SE, JB Hurley, U Janssen-Bienhold, SC Neuhauss, W Driever, and JE Dowling. 1995. "A Behavioral Screen for Isolating Zebrafish Mutants with Visual System Defects." *Proceedings of the ...* 92 (November): 10545–10549.

Budick, S a, and D M O'Malley. 2000. "Locomotor Repertoire of the Larval Zebrafish: Swimming, Turning and Prey Capture." *The Journal of Experimental Biology* 203 (Pt 17) (September): 2565–79.

Burgess, Harold a, and Michael Granato. 2007. "Modulation of Locomotor Activity in Larval Zebrafish During Light Adaptation." *The Journal of Experimental Biology* 210 (Pt 14) (July): 2526–39. doi:10.1242/jeb.003939.

Burgess, Harold a, Hannah Schoch, and Michael Granato. 2010. "Distinct Retinal Pathways Drive Spatial Orientation Behaviors in Zebrafish Navigation." *Current Biology : CB* 20 (4) (February): 381–6. doi:10.1016/j.cub.2010.01.022.

Chow, Brian Y, Xue Han, Allison S Dobry, Xiaofeng Qian, Amy S Chuong, Mingjie Li, Michael a Henninger, et al. 2010. "High-Performance Genetically Targetable Optical Neural Silencing by Light-Driven Proton Pumps." *Nature* 463 (7277) (January): 98–102. doi:10.1038/nature08652.

Crawley, J N. 1985. "Exploratory Behavior Models of Anxiety in Mice." *Neuroscience and Biobehavioral Reviews* 9 (1) (January): 37–44.

Douglass, Adam D, Sebastian Kraves, Karl Deisseroth, Alexander F Schier, and Florian Engert. 2008. “Escape Behavior Elicited by Single, Channelrhodopsin-2-Evoked Spikes in Zebrafish Somatosensory Neurons.” *Current Biology : CB* 18 (15) (August): 1133–7. doi:10.1016/j.cub.2008.06.077.

Fernandes, António M, Kandice Fero, Aristides B Arrenberg, Sadie a Bergeron, Wolfgang Driever, and Harold a Burgess. 2012. “Deep Brain Photoreceptors Control Light-Seeking Behavior in Zebrafish Larvae.” *Current Biology : CB* (September 18): 1–6. doi:10.1016/j.cub.2012.08.016.

Fraenkel, G. S., and D. L. Gunn. 1961. *The Orientation of Animals*. Dover, New York.

Friedrich, Rainer W., Gilad a. Jacobson, and Peixin Zhu. 2010. “Circuit Neuroscience in Zebrafish.” *Current Biology* 20 (8) (April): R371–R381. doi:10.1016/j.cub.2010.02.039.

Huang, Kuo-Hua, Misha B. Ahrens, Timothy W. Dunn, and Florian Engert. 2013. “Spinal Projection Neurons Control Turning Behaviors in Zebrafish.” *Current Biology* (August). doi:10.1016/j.cub.2013.06.044.

Louis, Matthieu, Thomas Huber, Richard Benton, Thomas P Sakmar, and Leslie B Vosshall. 2008. “Bilateral Olfactory Sensory Input Enhances Chemotaxis Behavior.” *Nature Neuroscience* 11 (2) (February): 187–99. doi:10.1038/nn2031.

Marr, David. 1982. *Vision: A Computational Approach*. San Francisco: Freeman & Co.

McLean, David L, and Joseph R Fetcho. 2011. “Movement, Technology and Discovery in the Zebrafish.” *Current Opinion in Neurobiology* 21 (1) (February): 110–5. doi:10.1016/j.conb.2010.09.011.

Mori, I, and Y Ohshima. 1995. “Neural Regulation of Thermotaxis in Caenorhabditis Elegans.” *Nature* 376 (6538): 344–8.

Müller, M, and Rudiger Wehner. 1988. “Path Integration in Desert Ants, Cataglyphis Fortis.” ... *of the National Academy of Sciences* 85 (July): 5287–5290.

Orger, Michael B, and Herwig Baier. 2005. “Channeling of Red and Green Cone Inputs to the Zebrafish Optomotor Response.” *Visual Neuroscience* 22 (3): 275–81. doi:10.1017/S0952523805223039.

Orger, Michael B, Adam R Kampff, Kristen E Severi, Johann H Bollmann, and Florian Engert. 2008. “Control of Visually Guided Behavior by Distinct Populations of Spinal Projection Neurons.” *Nature Neuroscience* 11 (3) (March): 327–33. doi:10.1038/nn2048.

Portugues, Ruben, and Florian Engert. 2009. “The Neural Basis of Visual Behaviors in the Larval Zebrafish.” *Current Opinion in Neurobiology* 19 (6) (December): 644–7. doi:10.1016/j.conb.2009.10.007.

Sawin, Elena P, Laurence R Harris, Ana R Campos, and Maria B Sokoiowski. 1994. "Sensorimotor Transformation from Light Reception to Phototactic Behavior in Drosophila Larvae." *Journal of Insect Behavior* 7 (4): 553–567.

Schoonheim, Peter J, Aristides B Arrenberg, Filippo Del Bene, and Herwig Baier. 2010. "Optogenetic Localization and Genetic Perturbation of Saccade-Generating Neurons in Zebrafish." *The Journal of Neuroscience : the Official Journal of the Society for Neuroscience* 30 (20) (May): 7111–20. doi:10.1523/JNEUROSCI.5193-09.2010.

Segall, J E, S M Block, and H C Berg. 1986. "Temporal Comparisons in Bacterial Chemotaxis." *Proceedings of the National Academy of Sciences of the United States of America* 83 (23) (December): 8987–91.

Toma, Daniel P, Kevin P White, Jerry Hirsch, and Ralph J Greenspan. 2002. "Identification of Genes Involved in Drosophila Melanogaster Geotaxis, a Complex Behavioral Trait." *Nature Genetics* 31 (4) (August): 349–53. doi:10.1038/ng893.

Warp, Erica, Gautam Agarwal, Claire Wyart, Drew Friedmann, Claire S. Oldfield, Alden Conner, Filippo Del Bene, Aristides B. Arrenberg, Herwig Baier, and Ehud Y. Isacoff. 2011. "Emergence of Patterned Activity in the Developing Zebrafish Spinal Cord." *Current Biology* 22 (2) (December): 93–102. doi:10.1016/j.cub.2011.12.002.

Wyart, Claire, Filippo Del Bene, Erica Warp, Ethan K Scott, Dirk Trauner, Herwig Baier, and Ehud Y Isacoff. 2009. "Optogenetic Dissection of a Behavioural Module in the Vertebrate Spinal Cord." *Nature* 461 (7262) (September): 407–10. doi:10.1038/nature08323.

3 BRAIN-WIDE MAPPING OF FUNCTIONAL NEURONAL GROUPS

3.1 PREFACE

The following chapter is adapted from a preliminary manuscript in preparation. I conceived the project, designed and performed the main analysis, and will be co-first author with Yu Mu who designed the experimental protocols, collected the data and performed the preprocessing. Yu Hu and Aaron Kuan conceived and performed analyses and interpreted the data. Owen Randlett and Maxim Nikitchenko performed the registration to the standard brain. I wrote the current version of the manuscript with helpful inputs from Yu Mu and Aaron Kuan, and help from Yu Mu on the method section. Florian Engert and Misha Ahrens conceived experiments and analyses, interpreted the data and supported the project. I would also like to acknowledge Takashi Kawashima for help with the preprocessing analysis, Caroline Wee for reading the manuscript, and members of the Engert lab for helpful discussions.

3.2 INTRODUCTION

Understanding the functional organization of the brain requires the recording and interpretation of neural activity from large populations of neurons. Recent advancements in functional imaging technology, including the development of sensitive fluorescent reporters of neuronal activity (Akerboom et al. 2012; Chen et al. 2013) and fast imaging techniques (Fahrbach et al. 2013; Bouchard et al. 2015; Tomer et al. 2012), have made simultaneous recording of large brain areas possible in many animal models (Schrödel et al. 2013; Prevedel et al. 2014; Peron et al. 2015; Lemon et al. 2015). In the case of the larval zebrafish, the transparency of the animal makes it a prominent model for brain-wide optical interrogation of the nervous system (Orger et al. 2008; Friedrich, Jacobson, and Zhu 2010; Orger 2016; Ahrens et al. 2012; Portugues et al. 2014), and with light-sheet imaging techniques, the majority of the ~100,000 neurons in the brain can be imaged simultaneously at the single-cell resolution in a behaving animal (Panier et al. 2013; Ahrens et al. 2013).

Such large-scale simultaneous imaging greatly facilitates the discovery of functional interactions between neurons across the brain. In sequential (non-simultaneous) imaging, it is difficult to compare neural responses across imaging planes that are not directly related to externally measurable references like sensory inputs or behavior, which presumably precludes a large part of the neural activity repertoire of a brain in its natural state. Yet, given the fast technical advances in simultaneous imaging, our comprehension of all neural circuits that can be monitored is still vastly outpaced by our data collection capacity. To extract information from these large datasets, the importance of focusing on a specific behavioral context or a candidate circuit is incontestable. But just as traditionally a neural anatomist would benefit from observations across the brain, with modern imaging, a broad characterization of brain-wide activity would also greatly aid hypothesis generation.

These brain-wide functional datasets are not only complex in nature, but also large in volume (sometimes terabytes per experimental session), which poses significant challenges to their analysis and interpretation. One practical approach for such analysis is to focus on the size challenge, by increasing computational power to efficiently process the data with cluster computing (Freeman et al. 2014). But arguably, for most biological questions, the amount of relevant information is not nearly as big as the raw data (Engert 2014), and once extracted, the lasting quest would be to explore and interpret such condensed datasets. In our study, we used nucleus localized GCaMP reporters that make cell segmentation more tractable. Although an exact one-to-one correspondence of our automatically segmented ROIs to neurons is not guaranteed, this scheme produces a robust description of brain-wide activity on the single cell level, while reducing the size of the dataset from several terabytes to a few gigabytes.

Our gigabyte-sized datasets still contain roughly 50,000-100,000 cells with thousands of time points and are inconvenient to inspect. While common dimensionality reduction methods (Cunningham and Yu 2014) are good for simplifying data by mapping them into lower dimensional space, it is difficult to visually examine more than 2 or 3-dimensions at once, especially when most dimensions in feature space only have highly abstract interpretations. For neural activity data, the time-series carries rich information yet is very intuitive for neuroscientists. To retain interpretability, we therefore chose cluster analysis as our main data compression method, which aims to reduce the number of examples by grouping objects that are similar together without compressing information along the time dimensions. Clustering analysis is especially suitable for large-scale analysis of complex datasets because by design, it is essentially exploratory analysis with little or no prior knowledge (Xu and Wunsch 2005). The

resulting clusters, or populations of neurons grouped by functional similarity, will be the main units we use to examine neural activity in this study.

The fact that thousands of clustering algorithms have been published (Jain 2010) underlines the difficulty in designing a general purpose clustering algorithm. To develop an unsupervised clustering method customized to our needs, we considered a number of features of the data. The first one is that a large fraction of neurons lack well-defined membership to any cluster. Thus, we effectively pruned the data to extract the most representative groups of active neurons. Another feature is that it is unclear what the ground truth of clustering structure would be; the clustering outcomes at this stage are mainly simplifications to aid conceptual interpretation of the data. We note that the relationship between such clusters is highly complex: they are hierarchical, often continuous, and highly heterogeneous - cluster sizes easily span three orders of magnitude for a given criteria. We therefore implemented our method with a graphical user-interface (GUI) for easy data exploration, so that any clustering result can, and necessarily should be, viewed in the context of functional activity.

After screening for functional groups in individual fish, the next step is to compare them across animals, and to examine them with proper anatomical references. Conceptually, anatomical comparisons are much easier than functional comparisons. For anatomical comparisons, we registered the image stacks to the recently developed "Z-Brain" atlas for larval zebrafish (Randlett et al. 2015) that contains molecular labels and definitions for anatomical regions. To compare clusters across fish, we first screen for clusters that occupy comparable anatomical space across fish. After that, functionally conserved clusters can be selected based on their relationship to the stimulus or behavior, or some other characteristic identified from manual inspections.

The results of our unsupervised clustering contain both clusters highlighting known anatomical structures and many previously uncharacterized functional neuronal groups. These groups would then represent network elements, and be of great interest for many types of downstream analysis. We further characterized these clusters in relation to the sensory-motor pathway, and examined the functional relationship between pathways activated by different stimuli. To illustrate our method's utility in generating biologically interesting hypotheses, we applied it to study the anterior hindbrain region, which is a great candidate for a central site for sensory-motor transformation and integration.

3.3 DATA COLLECTION AND PREPROCESSING

Using an imaging system reported previously (Vladimirov et al. 2014) (Figure 3.1A), we recorded the activity of practically all neurons in the larval zebrafish brain simultaneously, while presenting various visual stimuli and recording "fictive" behavior. Fictive swim signals are detected by extracellular recordings of the descending axial motor neurons on each side of the tail, and then reconstructed into fictive swim bouts (Masino and Fetcho 2005; Ahrens et al. 2012). Figure 3.1B shows the projections of a functional imaging stack, with abundant calcium activities at the single cell resolution present in most regions of the brain. The fish are labeled with GCaMP6f that is localized to the cell nucleus. The nuclear localization greatly facilitates automatic cell segmentation (Figure 3.1C, details see method section). The activity traces of individual neurons were automatically extracted for approximately ~80,000 neurons segmented per fish ($8.0\times10^4 \pm 1.6\times10^4$ ROIs, n = 18), which accounts for the vast majority of neurons in the brain (examples from one imaging plane in the midbrain in Figure 1d) with the exception of the most ventral part. For each fish, data was recorded at ~2 volumes/sec for ~30 min ($4.1\times10^3 \pm 1.5\times10^3$ time frames, n = 18 fish).

To efficiently explore this large volume of data, we developed a custom interactive platform in MATLAB. Among its many functions, basic examples include regression (Figure 3.2A-B), clustering (Figure 3.2C), ordering by features (Figure 3.2D) and their combination (Figure 3.2E-F). This software also allows for manual anatomical selection, set operations and easy organization and storage of identified clusters. Almost all of the analysis implemented in this paper have been integrated into the software, and can also be flexibly applied to new data.

Figure 3.1. Data collection and cell segmentation.

(**A**) Illustration of experimental setup. For this light-sheet imaging preparation there are two laser beams scanning from the front and side of the fish (but avoiding the eye area). The fictive behavior is recorded with two extracellular suction electrodes placed on each side of the tail. Inset on the right illustrates the decoding of the fictive behavior from the raw signals. Illustrations adapted from Freeman et al. 2014 (optics) and Ahrens, Huang, et al. 2013 (fictive behavior). (**B**) Average calcium activity in pseudo-colors, for one example animal. (**C**) Results of automatic cell segmentation based on nucleus-localized calcium indicator. GCaMP6f was expressed panneuronally under the *elavl3* promotor. Inset shows good coverage of segmented ROI's (red dots) within one imaging plane (total number of segmented ROI's in this animal: 92,538). (**D**) Example neuronal activity of (putative) single neuron ROI's within an imaging plan in the tectal region in the midbrain. Shown above the calcium traces is a bar illustrating the stimulus (with phototactic stimuli alternating with white background), and plotted at the bottom of the panel is the recorded fictive behavior (with three lines indicating left turns, forward swims and right turns from top to bottom). Scale bars, 50 μm.

(Figure 3.1 continued)

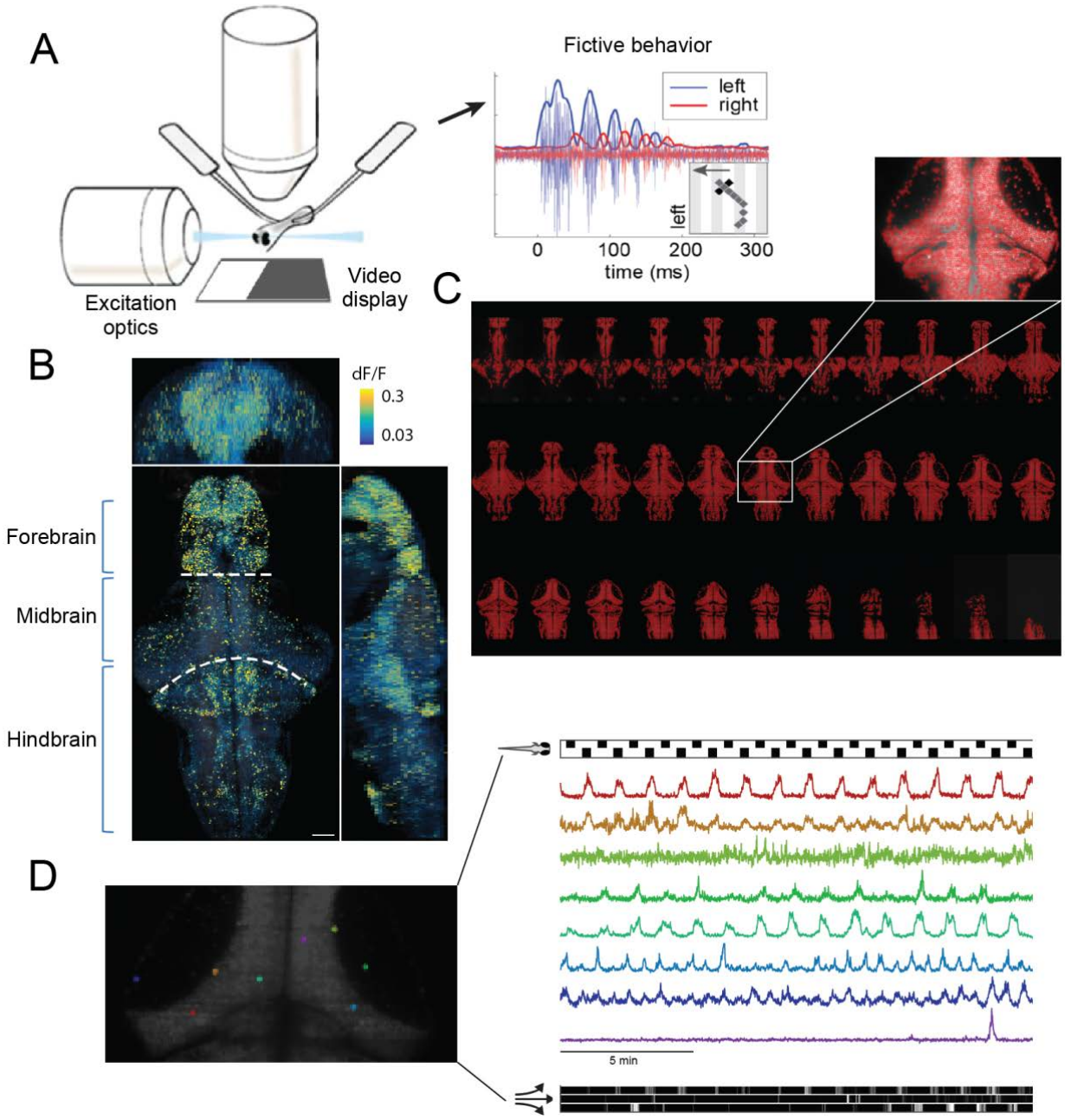

Figure 3.2. Basic utilities of custom interactive GUI for data exploration.

(**A**) Motor regressors (for left, right turns, respectively) were used to extract any cell that is correlated to the regressor beyond a chosen threshold, shown as a top-view projection. (**B**) Regression to stimulus regressors (for rightward phototactic stimulus, leftward phototactic stimulus and white background, respectively) identifies corresponding cells (beyond a chosen correlation threshold). (**C**) A direct application of k-means clustering, with k = 20 (distance measure: correlation). Resulting clusters are shown in different colors for this visualization. (**D**) Hierarchical clustering is subsequently used on the result of k-means clustering to rank clusters displayed in the GUI, and their relationship is displayed as a dendrogram. (**E**) Refine clusters with regression. After clustering, regression is performed on all cells in the brain with the average activity trace of a chosen cluster as regressor. Since the results of this regression include any cells that are similar to this cluster (to varying degrees depending on the threshold), this approach is useful to check for the completeness or the shape of a cluster. (**F**) Combining stimulus-locked statistics with clustering. In this example, we ranked neurons by the variance of their calcium activity across different trials of repeated stimulus presentations. Shown here is a selection of low variance neurons, further divided into 20 k-means clusters and ranked with hierarchical clustering for ease of visualization.

(Figure 3.2 continued)

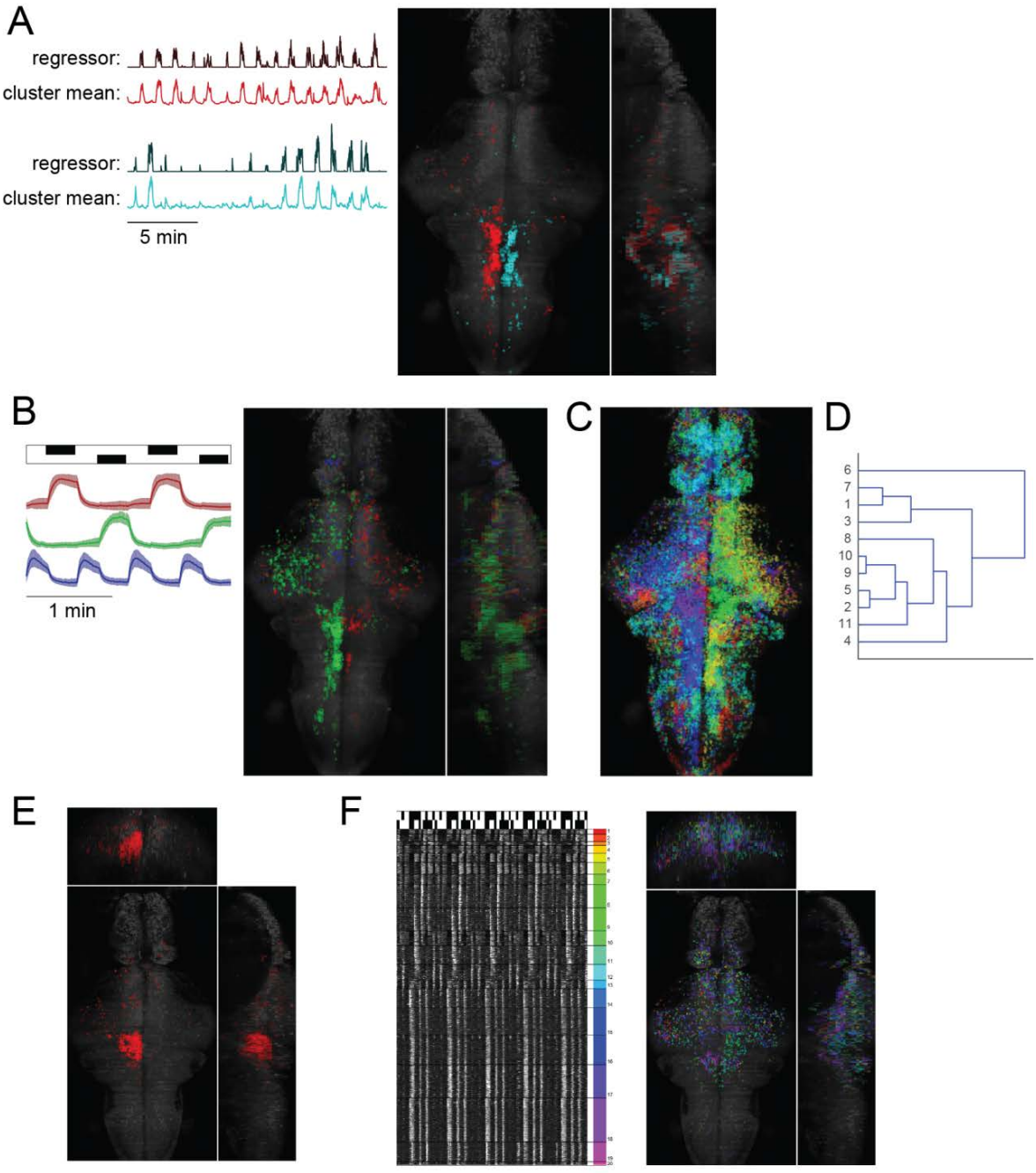

3.4 WHOLE-BRAIN AUTOMATED FUNCTIONAL CLUSTERING OF NEURONS

We devised an unsupervised clustering algorithm to extract the most representative groups of active neurons (see method section for details). Figure 3.3A shows an example of the resulting collection of clusters when applied to all cells in a single animal (Figure 3.4B). Note that the majority of the cells in an animal are actually not included in the cluster results (approximately 70-90% are excluded, varying across fish and dependent on the clustering stringency parameter discussed below). The clusters are ranked by hierarchical clustering (as in Figure 3.2D; colored in order in Figure 3.3A). The Pearson correlation coefficient matrix between all clusters in Figure 3.3B reveals various degrees of similarity between some groups of clusters, while many are uncorrelated to the rest. Figure 3.3C shows that the sizes of these clusters vary from 10 cells (the lower threshold allowed by the algorithm) to hundreds or even ~ a thousand for a small number of clusters.

These two characteristic of the data suggest that the high heterogeneity across the clusters is difficult to capture and visualize with single-level clustering structures. We address this challenge in three ways: (1) hierarchical clustering is applied on these clusters; (2) individual clusters can be easily subdivided again to reveal more details; (3) we define the main parameter of the algorithm as a sliding threshold that can be tuned to the desired level of clustering "stringency". Note that in this algorithm, the number of clusters is not predetermined; rather, this stringency parameter is specified (which approximately corresponds to the Pearson correlation coefficient of neurons within one cluster), and a certain number of clusters (on the order of a hundred) emerge from the clustering criterions. Our default stringency level (threshold = 0.7) shown in Figure 3.3A-E results in clusters that have an average correlation (0.6~0.8) between cells within a cluster (Figure 3.3D), which is far higher than typical correlation values between all cells (Figure 3.4A). A two-fold cross-validation at this level also shows that the clustering result is stable: ~70% of cells are stably classified into matching clusters based on two set of time frames of data (Figure 3.3E). When a more stringent threshold is applied, the total number of cells included in any cluster decreases (Figure 3.4D), the total number of clusters decreases (Figure 3.3F), and the cross-validation result improves (Figure 3.4C). Thus, based on the user's need, one can either obtain a large number of finely distinguished clusters, or a small number of more robust clusters.

We also visualize our clustering results with an independent unsupervised data visualization method, t-SNE (Van Der Maaten and Hinton 2008) (Figure 3.3G). The clusters that are found with our method (colored as in Figure 3.3A) also correspond to more distinct features in the t-SNE map, with the cells that did not pass the clustering criterion (and hence are not included in the clustering results) congregate in the larger central area (gray dots in Figure 3.3G).

Finally, we examined the collection of clusters for artifacts. For the default stringency level (0.7), we found a few clusters with cells conspicuously lined up in one of the laser-scanning directions (Figure 3.4E). When the clustering stringency is lowered to 0.5, the results contain far more of this type of artifacts (identified automatically with screen based on the cell location distribution within a cluster, Figure 3.4F). We speculate that at this level, the clustering algorithm is too sensitive compared to the signal to noise of the data, and for many inactive cells, the systematic noise along the laser scanning direction dominates the total signal. For this reason, we consider it not fruitful to drop the threshold below this level.

Lastly, in Figure 3.5 we display several groups of clusters as examples. Figure 3.5A show the largest four clusters from the cluster results in Figure 3.3A, two of which corresponds to the left-side and right-side motor networks in the hindbrain, respectively. For Figure 3.5B, we used a cutoff in hierarchical clustering to discard the most common cluster "family", so that the most "dissimilar" clusters emerge. Most of these clusters are not coupled to either stimulus or recorded behavior. For Figure 3.5C-D, we manually examined some stimulus related clusters and compiled a list of distinct response types interactively in the GUI (phototactic stimulus in Figure 3.5C, and moving stripes to elicit the optomotor response in Figure 3.5D).

Figure 3.3. Automated clustering algorithm, main results.

(**A**) Results of the automatic clustering algorithm applied to an example fish. The total 139 clusters (6,499 cells) are ordered by hierarchical clustering, and the rainbow colors are assigned based on the resulting leaf order. (**B**) The Pearson correlation coefficient matrix between all clusters from (A), calculated with the cluster-average. (**C**) Size distribution of all clusters from the above clustering analysis. (**D**) Histogram of average correlation between cells within a cluster, for all clusters from the above clustering analysis. (**E**) Two-fold cross validation. Clusters produced from the first versus second half of the time-points of the data are matched, and a score is calculated as the fraction of number of cells that are assigned to the matched clusters over the total number of cells. This is also visualized as the total "mass" distributed along the diagonal entries. (**F**) Number of clusters as a function of clustering "stringency" threshold (which corresponds to a correlation coefficient value), for n = 15 fish (different colored lines). (**G**) Visualization with t-SNE. Clusters in (A) are colored in the same colors (in one example fish); gray data points are cells that did not pass the clustering criterion i.e. not assigned to any cluster (1:10 down-sampled in number of cells for computational efficiency), and do not appear in (A) (but shown in Figure 3.4B).

(Figure 3.3 continued)

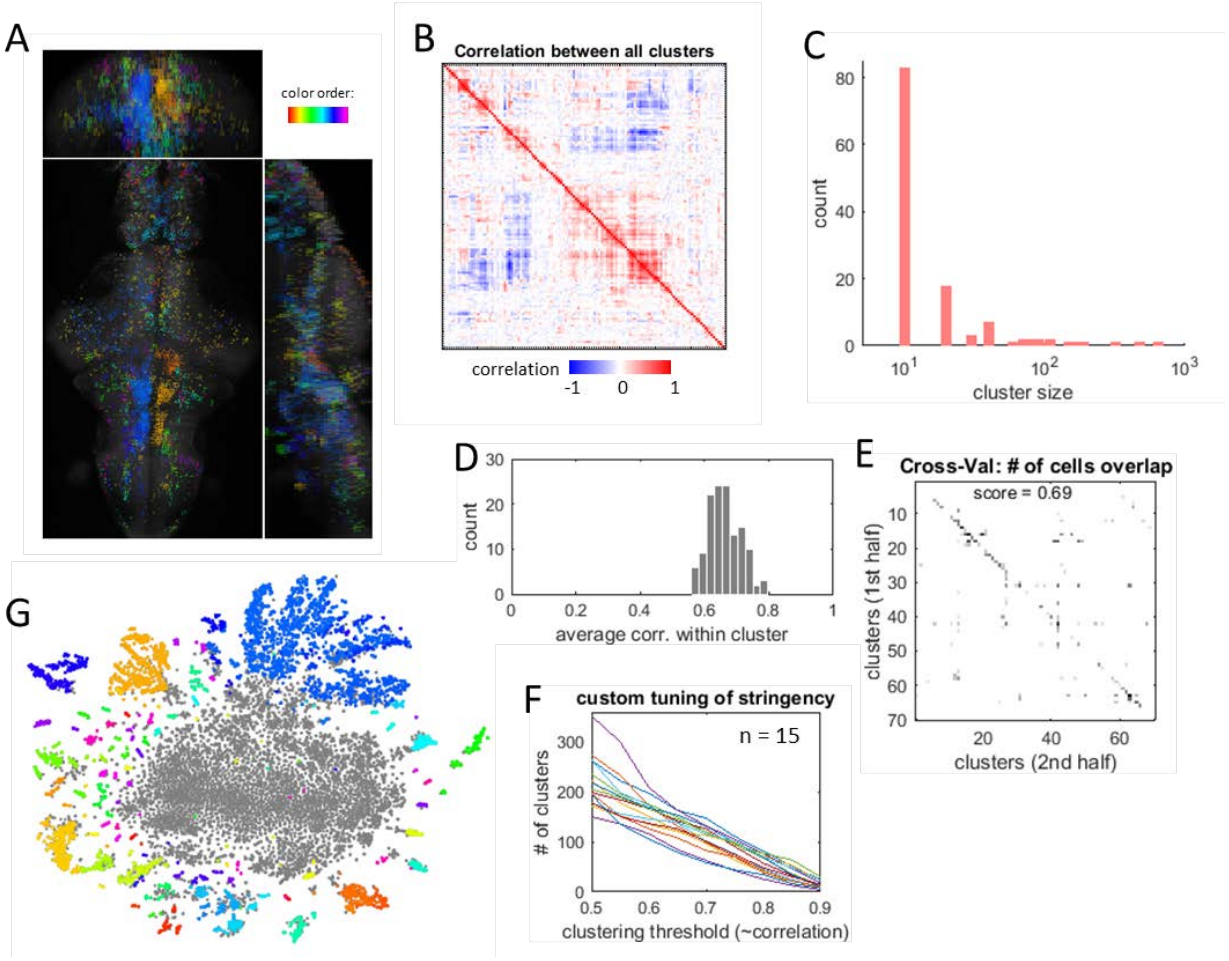

Figure 3.4. Automated clustering algorithm, supporting analyses.

(**A**) Distribution of pairwise Pearson correlation values for all cell pairs within a fish, for n = 5 fish (color lines). Dashed line indicates the distribution from a simulated Gaussian i.i.d. noise data with a matched number of time frames. (**B**) Cells included in clustering results (in red) versus cells that were not assigned any clusters based on the automatic algorithm (in gray). Z-planes are tiled ventral (upper left) to dorsal (lower right). (**C**) Two-fold cross validation scores as in Figure 3.3E, as a function of different stringency thresholds used for the automated clustering. (**D**) Total number of cells included in all resulting clusters, as a function of stringency thresholds. (**E**) Clusters from the default clustering (stringency threshold = 0.7) that are identified as artifacts. For each of the three clusters, the cells within the cluster are aligned along one dimension, which corresponds to one of the two laser scanning directions (anterior-posterior, and left-right). (**F**) Clusters identified as artifacts from clustering with threshold = 0.5. Each clusters is plotted in a random color. For (E-F), a simple script was used to screen for clusters that have very small standard deviation in any physical dimension.

(Figure 3.4 continued)

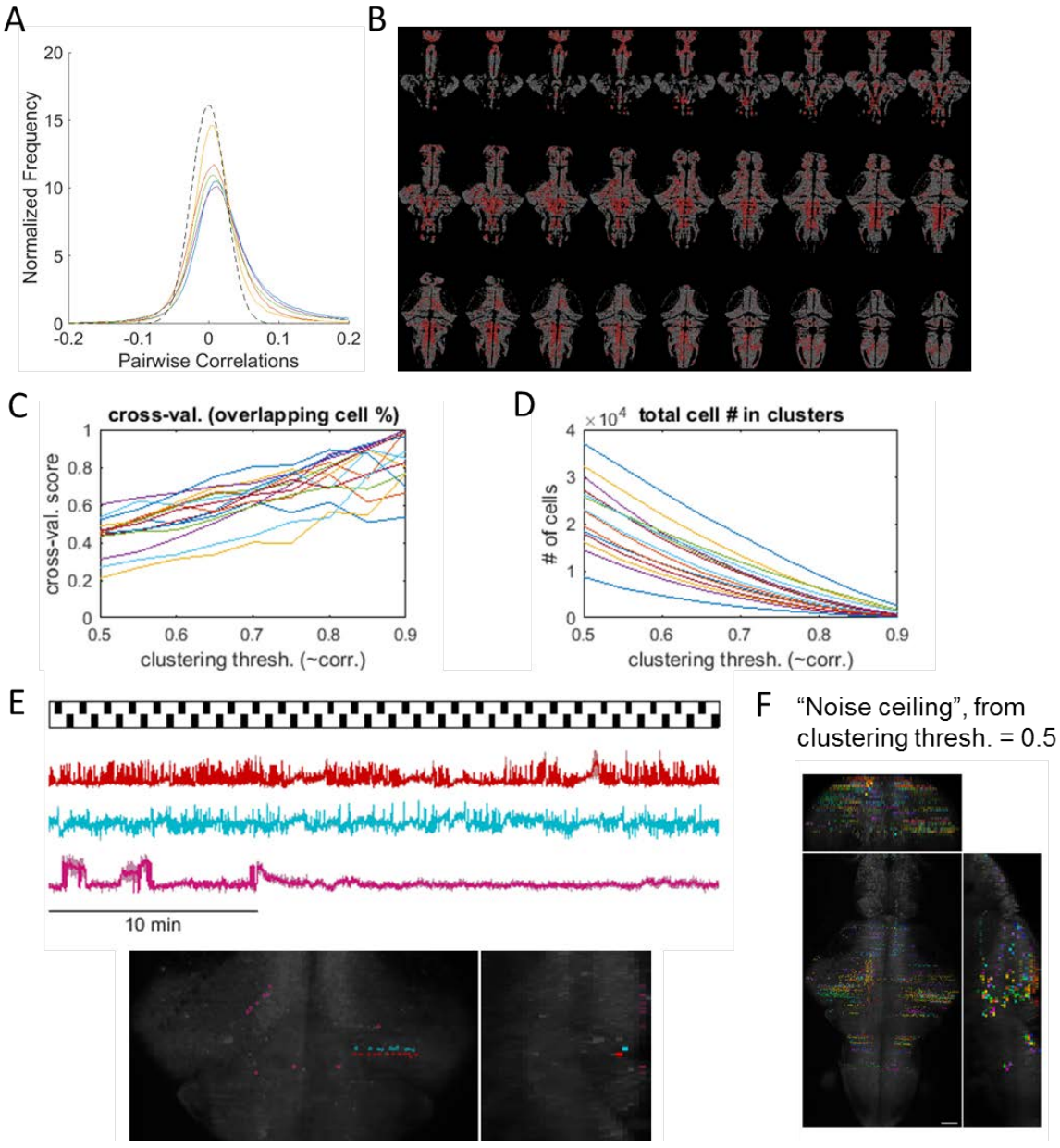

Figure 3.5. Examples of clusters.

(**A**) Top four clusters with the largest number of cells, from the automatic clustering results in Figure 3.3A. (**B**) Selection of dissimilar clusters. Hierarchical clustering of the cluster center of the automatic clustering results was applied with a similarity cutoff, and similar clusters belonging to main branches of the linkage tree were combined and excluded. The remaining smaller clusters are distinct in their activity pattern, and are less related to the stimulus or behavior (in contrast to the bulk of the clusters). (**C**) Selection of different response profiles locked to the phototactic stimuli. (**D**) Selection of response profiles locked to the optomotor response (OMR) stimulus, i.e. moving stripes, 4 directions indicated by the color in the stimulus bar on top: forward (green), backward (black), rightward (blue) and leftward (red). Clusters in (C-D) were selected and refined interactivity with the GUI.

(Figure 3.5 continued)

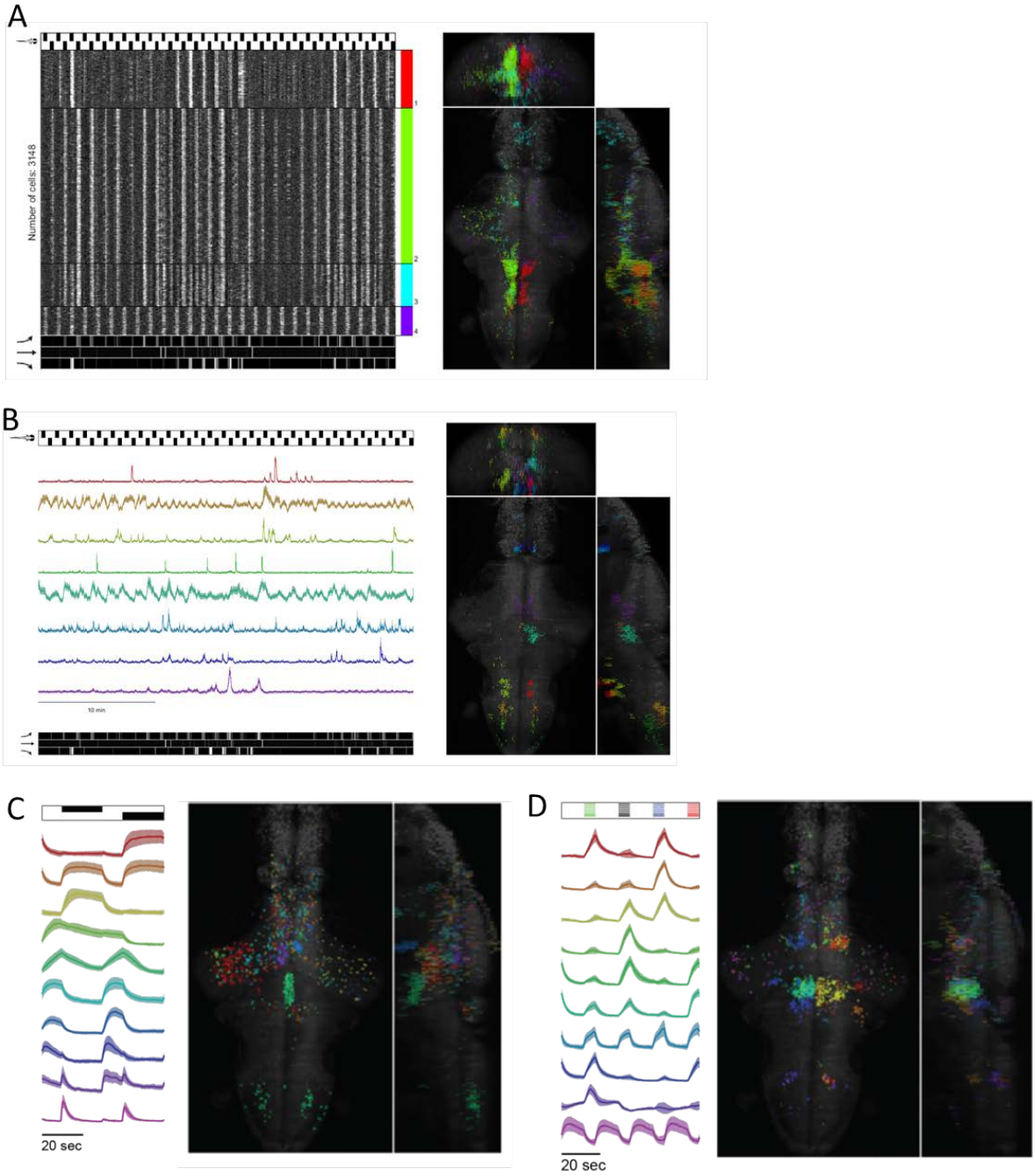

3.5 REGISTRATION OF MULTIPLE FISH TO ATLAS

In order to make comparisons between fish, we registered the individual fish together into a reference brain (Figure. 3.6A) named the "Z-Brain" (Randlett et al. 2015). This Z-Brain database contains many annotated molecular markers and masks of anatomical regions. We computed the standardized coordinates for all cells, and imported the anatomical masks into our GUI (Figure 3.6B) so that our functional clusters can be directly screened with them (examples shown in Figure 3.6C). Likewise, we can generate functional masks from functional clusters in the GUI, which could then be integrated to a functional database for future references.

To compare biologically relevant functional clusters at the population level is a much more challenging task. Conceptually, to identify clusters conserved across fish, there are two types of relationships to consider: the relationship in functional space, and in anatomical space (Figure 3.6E). One view is that in pure functional space, for a pair of clusters from two different fish, one could consider them "the same" if their neural responses are similar enough, e.g. both locked to a stimulus, a feature of the behavior, or share some other quantifiable characteristic. From another viewpoint, one might add the assumption that, biologically, structure often underlies function; even if two different brain areas exhibit similar activity patterns, because of their anatomical difference, their role in the functional network may differ significantly, thus one should consider them separate functional clusters.

We performed some exploratory analysis guided by the latter view which is more conservative. First, we assigned clusters with the automatic clustering algorithm for each fish, and extracted the standardized cell. Using a simple metric that relates to a normalized inter-cluster distance (Figure 3.6F), we exhaustively screened all pairs of clusters between different fish for clusters that occupy the comparable anatomical space (n = 18 fish). Figure 3.6H shows an example fish with all anatomically conserved clusters plotted, defined here as clusters that have anatomically comparable clusters in at least 6 other fish, out of 18 fish in total. Assessed as such, about half of the total clusters in each fish are anatomically conserved (Figure 3.6G). These clusters are also saved in the GUI and can be easily visualized interactively. Within these clusters, to further screen for clusters that are functionally comparable, one could either perform regression to any stimulus or motor regressors directly in the GUI, or (semi-)manually inspect clusters in a context of interest with the many other GUI functionalities.

Figure 3.6. Registration and comparisons across multiple animals.

(**A**) Registration of 3 individual fish into a standard brain. Maximum intensity projections for the 3 fish are shown in red, blue and green, respectively. (**B**) Projection of all anatomical masks imported into the GUI, random colors. (**C**) Example of anatomical regions, with number of cells from automatic clustering results that fall within a mask plotted for each region. (**D**) Average distance within cluster per fish, for n = 18 fish, experimental data (left) and simulated randomized control (right). Average distance between cells in a cluster was calculated for all automatically generated clusters, and the average of each fish is plotted as a data point (circle). The population average is shown with the black line (and standard error with the red lines). (**E**) Illustration of the concept of conserved clusters that we preferred. (**F**) Illustration of the distance measure we chose for assessing whether two clusters are conserved in anatomical space. (**G**) Percentage of clusters (from automatic clustering results) that has anatomically corresponding clusters in at least 6 other fish (out of the 18 fish assessed), plotted for each fish. (**H**) Example collection of anatomically conserved clusters for a single fish. Each of these clusters (displayed in different colors) has anatomically corresponding clusters in at least 6 other fish (out of the 18 fish assessed). Scale bar, 50 μm.

(Figure 3.6 continued)

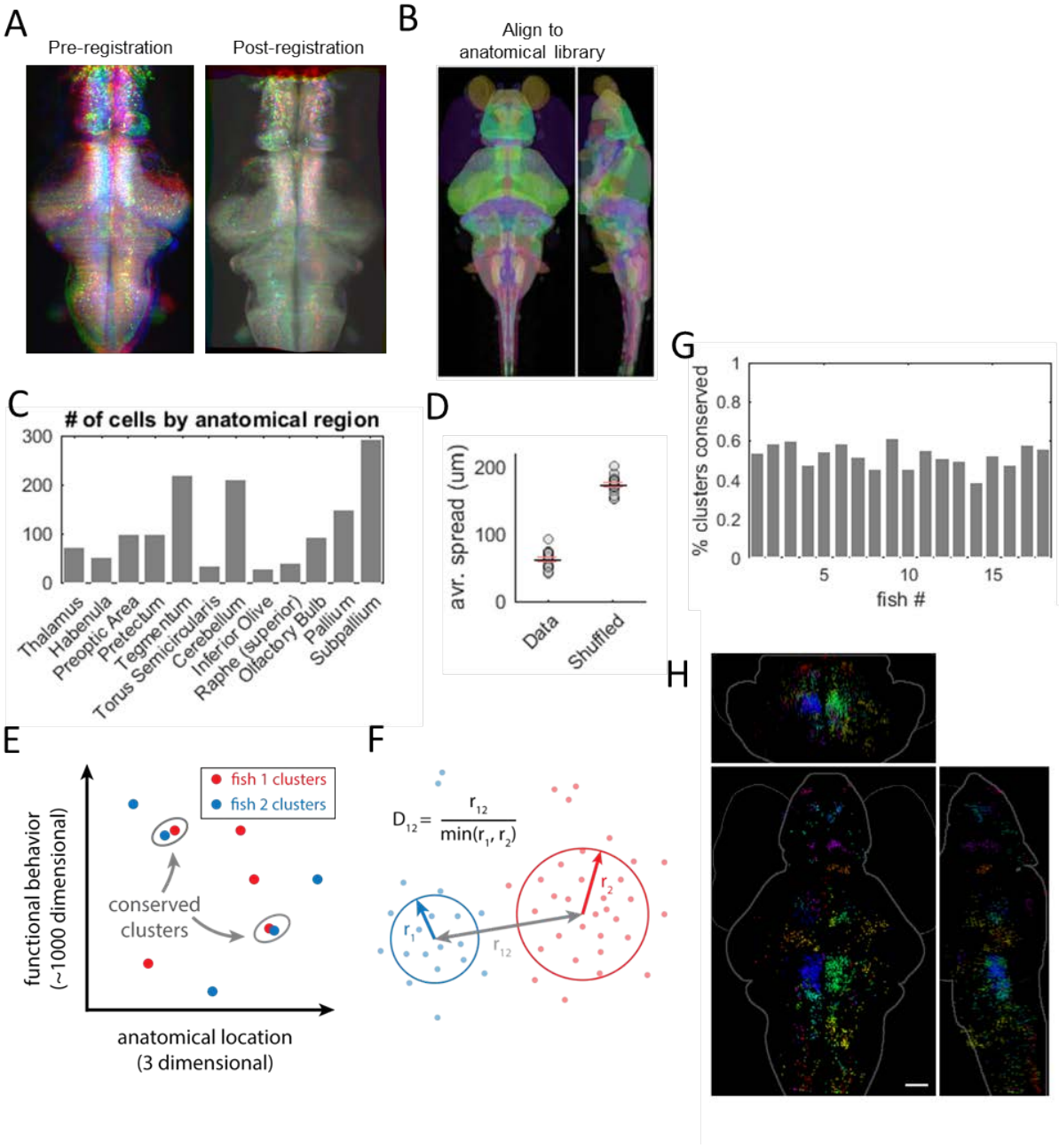

3.6 EXAMPLE OF CONSERVED CLUSTERS: PUTATIVE ABDUCENS NUCLEUS.

To demonstrate the effectiveness of our clustering approach, here we present a prominent example of functional clusters that correspond to anatomical regions that controls eye movement (Figure 3.7A) in the larval zebrafish hindbrain (Figure 3.7B). Based on the observation of functional features, we propose the identification of the putative abducens nucleus / velocity-to-position neural integrator (VPNI), and present a novel circuit hypothesis about where sensory information is integrated to generate eye movement.

Previous studies (Miri, Daie, Burdine, et al. 2011; Miri, Daie, Arrenberg, et al. 2011; Portugues et al. 2014) have located many VPNI neurons in the hindbrain by correlating neural activity to eye-tracking data, although there is some apparent discrepancy about the exact spatial distribution (which may be explained by the difference in paradigms). In our experiments, we do not have direct behavioral data on eye position, but because of the simultaneous imaging, we can directly perform single-trial analysis on the activity of large populations of neurons. Two anatomically well-defined and functionally salient clusters consistently appear in the ventral hindbrain in rhombomeres 5 and 6 for all fish (Figure 3.7C), and the activity does not correspond to either the stimulus or the fictive swimming behavior. Tightly associated with these two "core" clusters are large and more distributed networks of cells in several areas of the hindbrain, some directly dorsal to the "core" clusters (Figure 3.7D). Conveniently, in some fish, automatic clustering or regression to the average activity of the "core" clusters also reveal a pair of small clusters close to the anterior border of the hindbrain (Figure 3.7B, arrowhead), with activity highly correlated to the contralateral "core clusters". Based on our knowledge of eye control circuits that is conserved in many species (Figure 3.7A; Portugues et al. 2014), we propose that these "core" clusters are the putative abducens nucleus (ABN) in larval zebrafish that drive ipsiversive eye movements. The anterior clusters are most likely the oculomotor nuclei that receive input from the contralateral abducens nuclei and drive contraversive eye movements (Portugues et al. 2014).

The putative ABN occupies a distinct anatomical location: the caudal half in rhombomere 6 corresponds to one of the Z-Brain anatomical masks ("Rhombencephalon - 6.7FDhcrtR-Gal4 Cluster 3"). Within each side of the brain, the activity of a putative ABN is highly concerted (Figure 3.7E, arrows), and is often moderately anti-correlated to the contralateral one. The putative ABN activity diverges from the fictive motor signals during

behavioral paradigms that don't elicit stereotypical eye movements (as in this example, with phototactic stimuli presented). In such cases, they can be easily identified with the hierarchical clustering cutoff method for dissimilar clusters from Figure 3.5B. The extended ABN network can be interactively examined in the GUI, and when divided into several sub-clusters, they are dorsal to the putative ABN and relatively well separated by anatomical location (Figure 3.7D). Examination of the activity of these sub-clusters (Figure 3.7E, arrowheads) show that they show more regular features related to the stimulus, and that the activity of each of the left/right oculomotor nuclei is highly synchronous with a contralateral sub-cluster. This inspired us to propose that the ABN represents "intrinsic" oscillations that occur spontaneously and are responsible for the variability of the eye-motion, while these related dorsal networks are more integrated with sensory drives, and are responsible for the rostral projections to the oculomotor nuclei.

Figure 3.7. Example of interesting conserved clusters: putative abducens nucleus.

(**A**) Schematic model of eye-control (in many species). OMN: oculomotor nucleus. ABN: abducens nucleus. (**B**) Related neural populations in an example fish. VPNI: velocity to position neural integrator. Blue line: outline of the 'Rhombencephalon - Oculomotor Nucleus nIV' region from the Z-Brain atlas. Red line: outline of the Rhombencephalon (hindbrain). (**C**) The putative abducens nucleus (ABN). Sub-clusters are mapped to Rhombomeres 5 and 6 respectively (outline of masks from Z-Brain atlas). (**D**) ABN and associated network subdivided into 6 clusters with k-means clustering. The two clusters in blue and red are the putative ABN. Arrows: OMN. (**E**) Activity traces of the clusters from (D), colored accordingly. Stimulus and recorded fictive swimming are plotted (above and below the activity traces, respectively) for comparison. Arrows: putative ABN. Arrowheads: associated networks that appear more stimulus-related.

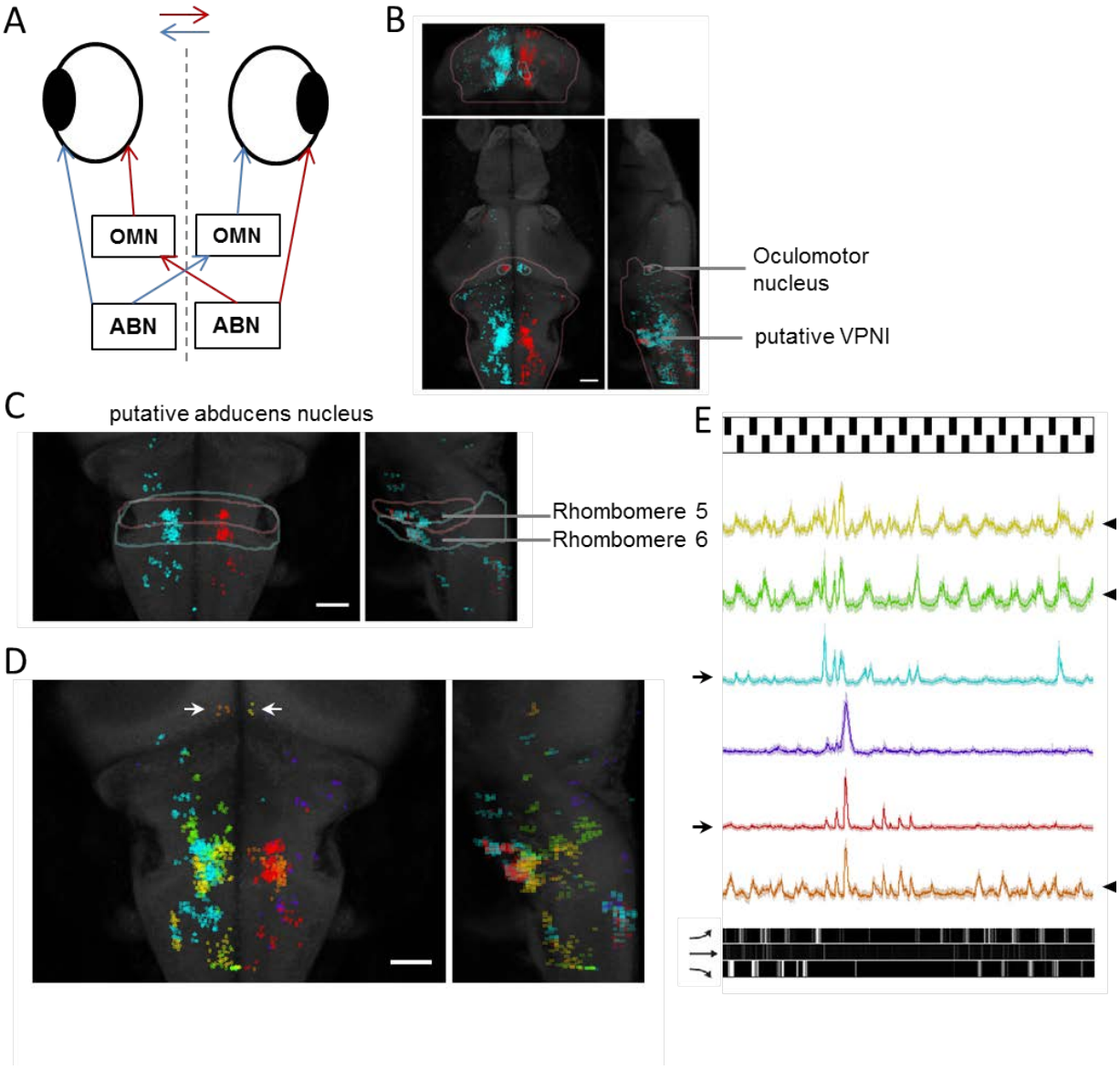
A
OMN
OMN
ABN
ABN
B
Oculomotor nucleus
putative VPNI
C
putative abducens nucleus
Rhombomere 5
Rhombomere 6
D
E

3.7 SENSORY-MOTOR MAPPING WITH MULTI-DIMENSIONAL REGRESSION

Given the richness of the data, there are obvious benefits to manually examining clusters that occur in certain anatomical regions of interest. But we can also ask questions at large-scale with simple but effective regression analysis methods (Miri, Daie, Burdine, et al. 2011). Here, we present an analysis to address a central question in systems neuroscience: the mapping of the sensory-motor pathway.

The straightforward method to use would be to perform a regression of the neuronal response to either stimulus or motor activity, and the regression coefficient would indicate how much the neural response relates to the stimulus or the motor output (Figure 3.8A). But this does not take into account the correlation between stimulus and motor. If the behavior is related to the stimulus, even a purely stimulus-locked neuron would appear to be motor-correlated. Therefore, here we first orthogonalize the regressors to each other, and use the set of ortho-normal regressors to perform a multiple linear regression analysis. Figure 3.8B shows an example of a motor regressor that is orthogonalized against the stimulus regressor. Now using a two-dimensional map, we can visualize automatic clustering results for an example fish using their stimulus and (orthogonal) motor correlation coefficients (Figure 3.8C-D). We can also ask which clusters are more involved in the sensory-motor transformation. By quantifying the two-dimensional magnitude of the stimulus and motor correlation coefficients, we can exclude clusters that are not strongly correlated to stimulus or motor, or any of their combination (Figure 3.8E, showing clusters outside of the radius in Figure 3.8C). Of particular interest are clusters that have high (orthogonalized) motor correlation but the lowest stimulus correlations: these clusters may represent the source of the behavioral variability between stimulus repetitions (Figure 3.8F). The most prominent cluster as such (Figure 3.8F, arrowhead) is one that corresponds very well to an anatomical map in the Z-Brain atlas defined from a transgenic line (Mesencephalon vglut2 cluster 1), and is located between the left and right nucMLF (nucleus of the medial longitudinal fascicle). Given the role of the nucMLF in controlling forward swimming and that electric stimulation in this area can drive swimming behavior (Severi et al. 2014; electrodes placed near the nucMLF in their experiment), it would be very interesting to further investigate the potential role of this cluster in locomotion generation.

Figure 3.8. Sensory-motor mapping with multi-dimensional regression

(**A**) Conceptual illustration of orthogonalization of the motor regressor. We note that the motor output itself is often related to the stimulus (upper panel), and compute the component of the motor regressor(s) that is orthogonal to the stimulus regressor(s) (lower panel, orange vectors). (**B**) Example of motor regressor orthogonalization. In the bottom trace, the orthogonalized motor regressor is no longer positively correlated to the stimulus. (**C**) Regression coefficients fitted with multiple-regression for all automatic clusters from a single fish. A set of orthonormal regressors are used that represent stimulus features (different directions for phototaxis and optomotor response) and orthogonalized behavior features (forward, leftward and rightward swimming). The two axes represent the average correlations from the group of stimulus regressors versus the group of (orthogonal) motor regressors. Each circle in the plot represents data from one cluster, with the size of the circle proportional to the number of cells in the cluster. The color is entirely determined by the x, y coordinates (2-dimensional colormap shown in inset) and only used to match the coloring in (D) and (E). The dashed black line is drawn at a radius of 0.3 to indicate the clusters (with a larger radial values) shown in (E). (**D**) All clusters from an automated clustering analysis for a single fish, colored according to (C) based on the stimulus and (orthogonal) motor coefficients of each cluster. (**E**) Similar to (D), but only showing the subset of clusters that have a larger combined correlation coefficient than 0.3, matching the clusters with a larger radial distance (outside of the dashed black line) in (C). (**F**) Top three clusters from (E) in terms of smallest stimulus correlation, with the best matching Z-Brain anatomical masks drawn as outlines. Arrowhead: mask for Mesencephalon vglut2 cluster 1. Arrows: pair of masks for Mesencephalon nucMLF (nucleus of the medial longitudinal fascicle). Scale bars, 50 μm.

(Figure 3.8 continued)

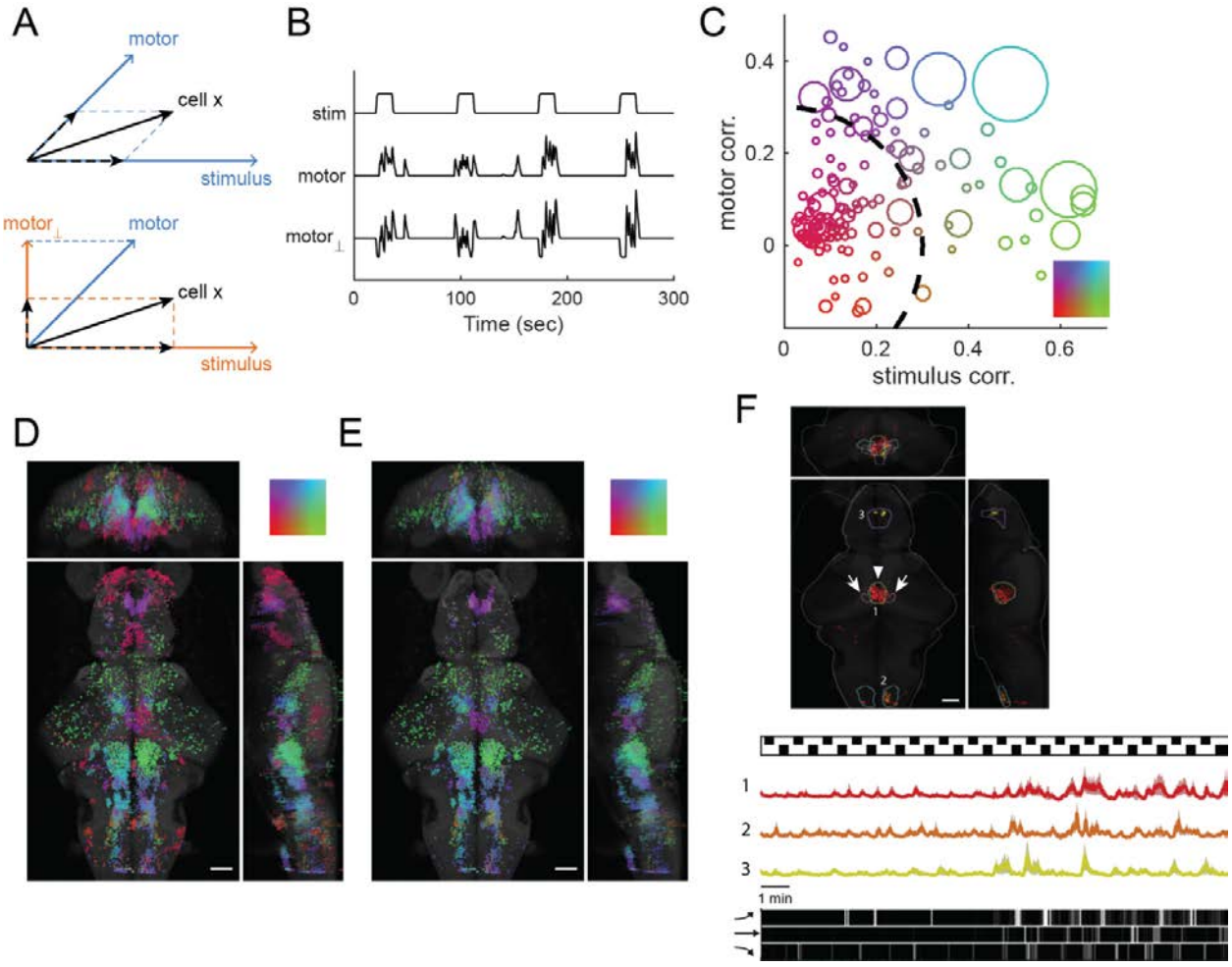

3.8 COMPARISONS OF ACTIVITY BETWEEN MULTIPLE STIMULUS CONDITIONS

An interesting biological question is how the brain responds to different stimulation conditions. One would predict that some neural populations respond selectively to different stimuli and some respond across several stimuli. For example, some early sensory areas should respond differentially, while the motor components may be activated in all swim-eliciting conditions; and it would not be surprising if some late-sensory or early-motor areas exhibit more complicated response features.

To compare the functional architecture between different stimulus conditions, we exposed a group of fish (n=6) to multiple stimulus categories sequentially: phototactic stimuli, moving stripes for the optomotor response (OMR) (Orger and Baier 2005), dark environment for spontaneous swimming (Dunn, Mu et al. 2016), dark flashes for the dark-startle response (Burgess and Granato 2007), and looming stimuli for the visual escape response (Dunn 2015). We performed automatic clustering to either the full data or on individual time-blocks with a single stimulus presented. Cross-validation of these clustering results across stimulus conditions (Figure 3.9A) show that while at least half of the clusters (associated with the default clustering stringency) are generalizable within the same stimulus category, at least 1/3 are retained across different stimuli (1/2 or above if the looming stimulus is excluded). Interestingly, clusters that are identified from the spontaneous period (constant dark background) are ≥0.5 matched with clusters obtained from phototactic stimuli, moving stripes (OMR) or dark flashes. This again highlights the power of having access to simultaneous activity to help uncover intrinsic organizational patterns among neurons. Visual inspection of the overlapping set of cells for phototaxis and OMR show that the main clusters in most brain regions are quite stable with the exception of the tectum (Figure 3.9B).

Another method to quickly compare responses between stimuli is to compare neural activity to a collection of stimulus and motor regressors, and classify cells based on their best regressor. Figure 3.9C shows that while many neural responses match best to a single stimulus type, some neurons are better classified as responsive to both phototactic and OMR stimuli. Many of these neurons are located in the anterior hindbrain, a region we will examine in more details in the next section in the context of hypothesis generation.

Figure 3.9. Comparisons of clusters between multiple stimulus conditions.

(**A**) Two-fold cross-validation (performed as in previous figures) between multiple sets of stimuli within each fish (n = 6 fish), with scores indicating the fraction of cells in matched clusters over the total number of cells. Each fish in the analysis has been presented with all 5 different stimuli (see method section for stimulus descriptions). The "all" category uses the combined data from all 5 stimulus periods. The diagonal (first item in each row) indicates the average cross-validation scores for a single stimulus condition. Color coding is redundant with the written values. (**B**) Cross-validated clusters between two stimuli (i.e. the intersection of the two sets of clusters after matching). Left panel: all clusters obtained from the phototaxis data from one fish. Right panel: cross-validation is performed on automatic clustering results for phototaxis versus clustering results for the OMR (optomotor response) stimuli; only cells that are matched in both cross-validation sets are shown, colored according to their original clusters in the left panel. (**C**) Cells classified by their best regressors, for cells that have a correlation coefficient >0.4 for their best regressors. Labels indicate the regressor that best matches the activity profile of a cell. Regression was performed with different stimulus regressors (with their combinations) and motor regressors, but only cells best matching stimulus regressors are shown. Note that the bottom two clusters (purple and magenta) matches better to stimulus combination of phototaxis plus OMR, than to either stimulus alone. Scale bars, 50 μm.

(Figure 3.9 continued)

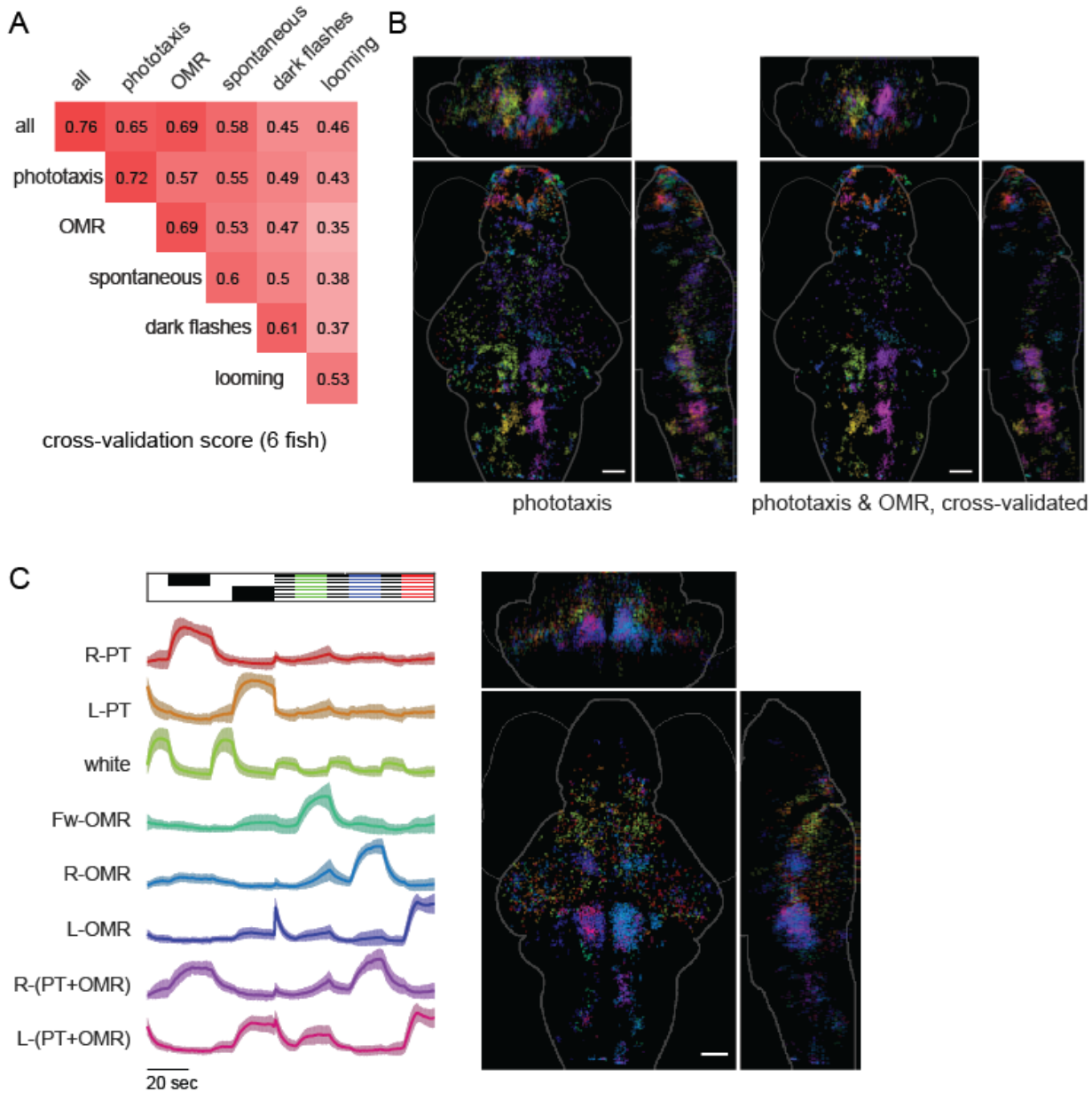

3.9 THE ANTERIOR HINDBRAIN AS AN IMPORTANT SITE FOR SENSORY-MOTOR TRANSFORMATION

Given the richness of this dataset, it will be unrealistic to exhaust all interesting phenomenon that arises; and giving an interesting phenomenon, one would benefit much more from many carefully and specifically designed experiments for a proper investigation. However, our explorative approach implemented as a GUI is ideally suited for generating hypotheses from this dataset. To demonstrate the power of our exploratory analyses, we will present some example hypotheses for a likely very important anatomical region that has been, for the large part, uncharacterized in existing studies.

From the analyses in Figure 3.8, the anterior hindbrain (AH) region, whose activity is related to both stimulus and behavior, emerges as a potentially central part of the sensory-motor pathway. When mapped to the Z-Brain atlas, the region corresponds to rhombomeres (Rhm) 1-3, and upon visual examination, functionally defined clusters are often aligned to individual rhombomeres along the rostral-caudal axis (Figure 3.10A-C). The functional clusters in Rhm-3 have been reported and characterized recently and are termed the "anterior rhombencephalic turning region" (ARTR) (Dunn et al. 2016) or the "hindbrain oscillator" (Ahrens et al. 2013). They are described as slowly fluctuating populations of neurons that relate to a short-term left/right turning bias that can be observed in a featureless environment. To examine the AH clusters in their brain-wide context, we also performed regression with these cluster means for all cells in the brain (Figure 3.10-D). Many cells are found caudal to these clusters in the hindbrain motor regions, but more interestingly, some cells in the Torus Longitudinalis (Figure 3.10D top panel, red mask) also show very similar activity to the AH clusters.

As earlier shown in Figure 3.9C, the functional clusters in Rhm-1 and Rhm-2 are strongly tuned to OMR stimuli and also phototactic stimulus features. The ARTR in Rhm-3 is also tuned to the stimulus when the behavior is mostly influenced by the stimulus. As in Figure 3.2F, we ranked the AH clusters by the variance of their activity between stimulus repetitions, so low variance (or strong periodicity) suggests that the activity is largely triggered by the stimulus. For two example fish presented with different stimuli, different AH clusters were ranked as most stimulus locked (Figure 3.10E), suggesting a possibility that the sensory motor transformation is not one of a simple relay. In fact, when we examine the activity of 4 major groups of cells – the left and right half of Rhm-1 and of

Rhm-3, respectively, we observe an interesting correlation pattern. While the two groups on the left side are highly correlated, the two groups on the right side are not correlated; but within each rhombomere, the left and right groups are strongly anti-correlated. An estimate from a population of 8 fish also yields strong average anti-correlations of -0.5±0.2 between the left and right clusters in Rhm-1. From the ARTR study (Dunn et al. 2016), we know that out of the 4 stripes (as illustrated in Figure 3.10C), the center clusters are glutamatergic and the lateral clusters are GABAergic. This is also consistent with the structural and functional ground plan of the larval zebrafish hindbrain (Kinkhabwala et al. 2010), and based on that, these glutamatergic and GABAergic stripes extend rostrally and caudally throughout the hindbrain. We therefore speculate that there is mutual inhibition not only between the left and right half of the ARTR, but also in the Rhm-1 clusters. Curiously, when we subdivide the Rhm-1 into 4 groups (2 on each side, for a different fish), we see that the two pairs on the same side are strongly correlated, but not all pairs across the midline are anti-correlated. This may be explained by having only subsets of cells in the Rhm-1 clusters connected by mutual inhibition, while other subsets may be receiving sensory relays and integrating them into the anti-correlated dynamics.

Figure 3.10. Anterior hindbrain clusters as a demonstration in hypothesis generation.

(**A**) Location of the anterior hindbrain (AH) clusters. Three Z-Brain anatomical masks for rhombomeres (Rhm) 1-3 in the Rhombencephalon (hindbrain) are also drawn for reference. Clusters were generated automatically in three steps for this fish: (1) automatic clustering was applied to phototaxis and OMR data, respectively; (2) cells that did not pass cross-validation were discarded; (3) only cells that fall within the 3 rhombomere masks were kept. (**B**) Enlarged view of the anterior hindbrain region. For clarity, two dashed lines are drawn to indicate the boundaries of the three rhombomeres (same for subsequent figure panels). Arrow: the clusters in Rhm-3 are a group of four clusters termed the "anterior rhombencephalic turning region" (ARTR) (Dunn et al. 2016) or the "hindbrain oscillator" (Ahrens et al. 2013). Arrowhead: raphe nucleus, which exhibits very different activity patterns from the other clusters in this inset. (**C**) Cartoon model of the AH clusters (without the raphe). (**D**) Activity in other areas of the brain that are closely related to the AH. Top panel: Torus Longitudinalis (shown by mask anterior to the hindbrain). Bottom panel: clusters more caudal in the hindbrain, including the Inferior Olive (arrow). (**E**) AH clusters ranked by their periodicity in regard to the stimulus, quantified by the variance of functional activity across stimulus repetitions. For the example fish in the top panel, the left cluster in Rhm-2 is the most stimulus-locked, followed by the right clusters in Rhm-1 and Rhm-2. For another fish (bottom panel), the ARTR/HBO clusters are more stimulus-locked instead. (**F**) Relationship between four main clusters (the Rhm-1 pair and the Rhm-3 pair) for an example fish. Middle panel: The stimulus presented is a randomized sequence of phototactic stimuli and whole-field bright/dark stimuli. Right panel: correlation matrix between the 4 groups includes strong positive and negative correlations. (G) Subdivision of the pair of Rhm-1 clusters. The correlation matrix shows strong anti-correlations between the pairs, but also a curious lack of anti-correlation between 2 sub-clusters. Scale bars, 50 μm.

(Figure 3.10 continued)

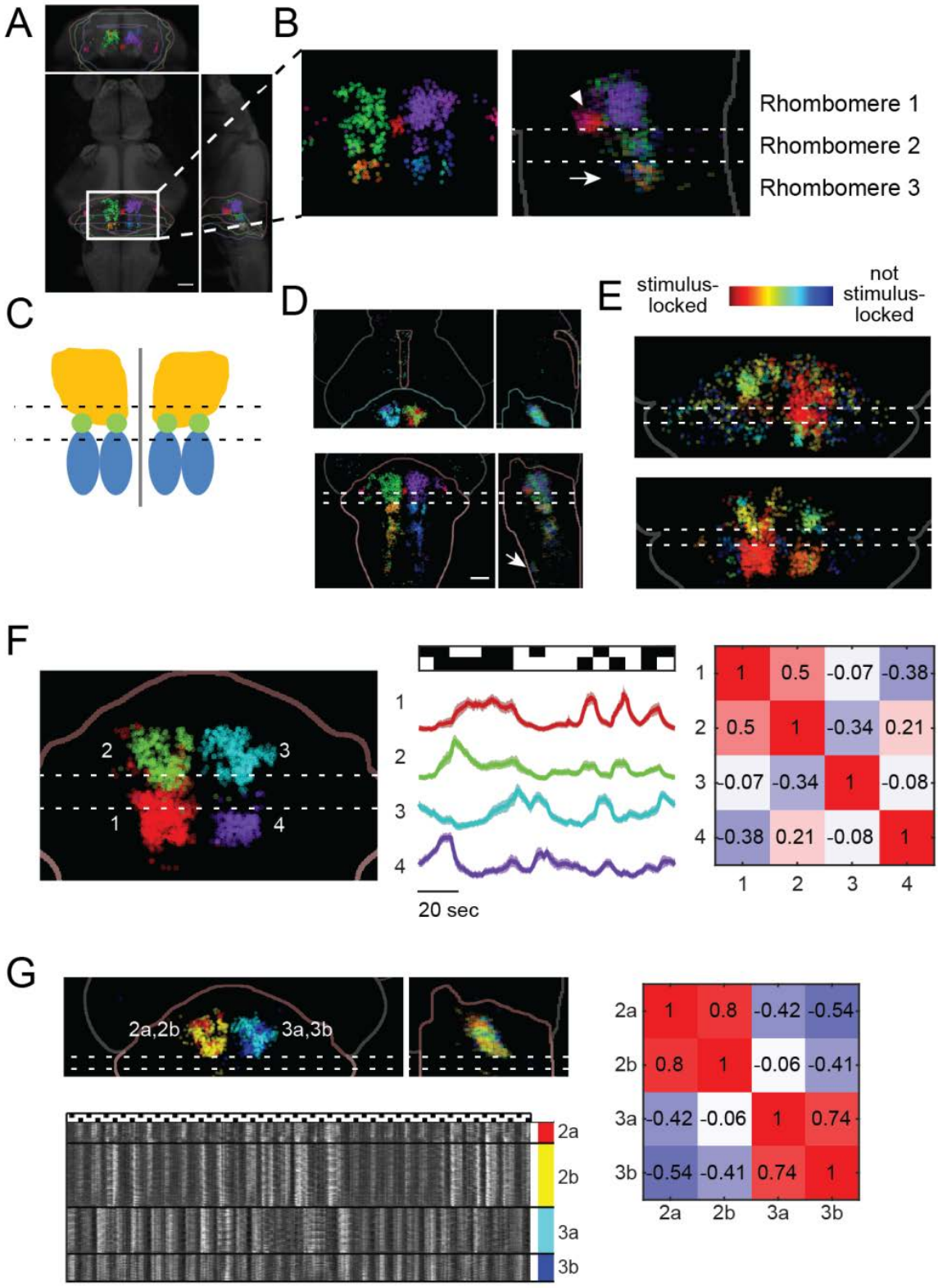

3.10 DISCUSSION

In this paper, we presented the methods and results of our extensive exploration of a large-scale, high-quality functional dataset. We developed a customized unsupervised clustering method to reveal a rich collection of functional clusters (on the order of a hundred per animal) that facilitates our understanding of the functional organization of the brain. We constructed an interactive software platform for detailed explorations of these clusters, and the user can combine the various methods introduced in this chapter with flexibility and tailor the analysis to their specific interest. The dataset and our interactive software (GUI) are available upon request. Using these analytical methods, we presented several findings with detailed circuit hypotheses that invite further investigation: (1) the putative abducens nucleus and associated network for the control of eye position; (2) an anatomically well-defined region in the midbrain that represents motor variability relatively independent of sensory inputs, and may be involved in locomotion generation; and (3) anatomically well-structured functional groups in the anterior hindbrain that may be involved in integrating different stimulus types and influencing the motor circuit related to left/right turning bias. These explorations demonstrate the utility of our approach in hypothesis generation from such a complex dataset.

Our clustering algorithm is in essence a variation of hierarchical (agglomerative) clustering with a flavor of seed-based clustering and density-based clustering, preceded by effective preprocessing, and using correlation distances to determine the final number of clusters. These combined features result in robustness to high noise levels and high computational efficiency; whole-brain single-cell resolution data (~100,000 cells, ~5000 time frames) can be easily performed on a standard desktop computer on the timescale of minutes.

We believe that the results of our whole-brain automatic clustering algorithm reflect two fundamental characteristics of the functional organization of the larval zebrafish brain. (1) A high percentage of neurons do not contribute significantly to the functional diversity at the circuit level. This is suggested by our result that most neurons are not assigned to any cluster by our algorithm. Interestingly, this is especially true in areas where young neurons are added to the rapidly developing brain (Figure 3.4B). (2) The relation between functional clusters is complex and likely best described hierarchically. In Figure 3.3C we show that the sizes of the clusters can vary over 3 orders of magnitudes. On one end of the size spectrum, strong stimuli can evoke concerted responses in thousands

of neurons, often in the motor areas, but also in the midbrain or the hypothalamic areas. On the other end, we detect many small clusters with only a dozen neurons but carry highly correlated signals. We chose our minimum cluster size to be 10 neurons; while it can be reduced, we believe that circuits smaller than this are better studied with a closer experimental focus on the target.

Previous whole-brain studies in larval zebrafish have suggested that there is a precise and elaborate underlying functional architecture to the larval brain (Portugues et al. 2014; Randlett et al. 2015; Fosque et al. 2015; Orger 2016). It has also been noted that the stereotypy differs among neurons; some transgenetic labels are highly variably positioned in the tectum (Randlett et al. 2015). Our findings are consistent with such observations. We find a relatively high level of stereotypy as well as significant variability in physical location for many of our functional clusters across animals. It still remains to be determined what factors are responsible for this observed stereotypy/variability of the functional organization. We also found that functional activity in the larval zebrafish brain is often highly concerted in large areas (especially in the hindbrain), in contrast to the more variegated signals in the mammalian cortex. We speculate that this may be a feature of evolutionarily older brains that relate more to the mammalian brain stem rather than the cortex; it may also be a feature of this developmentally young brain, and it is possible that the concerted motor activity would differentiate further to allow for more nuanced motor control in the adult fish.

The collection of our functional clusters ranges from highly sensory-correlated to highly motor-correlated, although many clusters are not directly correlated to either; these clusters would have been hard to identify without being able to perform single-trial analysis, which again highlights the advantage of simultaneous recordings of whole-brain activity. This comprehensive set of clusters facilitates explorations of large-scale brain activity features, and provides a basis for further analysis such as inferring functional connectivity with more advanced statistical tools.

In parallel, semi-manual explorations can also lead to valuable insights and inspirations for generating new hypothesis. With the abducens nucleus example in Figure 3.7, we showed that we can robustly identify a large and important neural network even in the absence of corresponding behavioral recordings, which leads to detailed hypotheses about the dynamics and interactions of network elements. Similarly, the example in the anterior hindbrain (Figure 3.10) revealed interesting network organization and dynamics through the combined usage of

various methods. Such candidate circuits that arise from the exploration of this dataset will hopefully inspire hypothesis-driven studies, which can additionally employ techniques for optical manipulation, electrophysiology, viral tracing, and connectomics to promote mechanistics understandings.

The analytical methods presented here are also generally applicable to other large-scale, high-resolution functional datasets to identify functionally defined structures in the brain – a pressing step towards understanding the complete neural networks underlying brain functions.

3.11 MATERIAL AND METHODS

Light-sheet imaging

The light-sheet imaging experiments were performed as previously described (Vladimirov et al. 2014). Transgenic zebrafish, panneuronally expressing calcium indicator GCaMP6 under *elavl3* promoter and nucleus-targeted as *Tg(elavl3:H2B-GCaMP6f)* , was used for imaging. Zebrafish larvae (5 dpf – 7 dpf), were paralyzed with 1mg/ml alpha-bungarotoxin (Sigma-Aldrich), and embedded with 2% low melting point agarose in a custom made chamber which allowed for electrical recordings of fictive swimming and light-sheet laser beams illuminate the brain from the lateral and frontal directions. The majority of the brain was covered by the frontal and lateral laser beam illumination. The imaging rate was about 2 brain volumes/s (2.11 ± 0.26 Hz), and the variability came from the size of the brain (mainly because of the thickness difference). Each experiment lasted between 30 to 120 min.

Cell detection

After imaging acquisition, the time series of each plane was registered by custom-written C/CUDA software for the XY plane translation. Z-drift was corrected by first comparing patches of images with the nearby planes from the first 2 min recording, and then calculated by linear fitting the distance across the Z-planes. Only the part of experiment when the XY- or Z-drift smaller than 1 um was taking for further analysis.

Cells were detected from the averaged image. In the *Tg(elavl3:H2B-GCaMP6f)* line, calcium indicator was mainly localized in the nucleus, form a bright disk on each plane, a property facilitates neuron detection. First, GCaMP expression area was extracted by binary thresholding based on pixel intensity and local contrast. Second, each pixel was normalized locally by assigning a relative rank of intensity within a disk patch (radius = 4 μm), then further smoothed by a circular patch with radius of 1.6 μm. Center of the cell body was determined by local maximum point within circular patch with radium of 2.8 μm.

Fictive behavior recording

The fictive behavior setup has been previously described (Dunn et al. 2016). Visual stimulation patterns were generated by custom-written C# software, delivered by a projector with homogeneous red light, and projected to a diffuser which was stuck on the bottom of the imaging chamber. In the meantime, two suction glass pipettes

(~45 μm inner diameter) were attached on the skin from each side of the tail. Gentle suction was applied to help the electrical contact with the motor neuron axons was made. These electrodes record spiking from multiple motor neuron axons, providing readout of intended locomotion (Dunn et al. 2016, Ahrens et al. 2012, Masino and Fetcho, 2005). Extracellular signals were amplified with an amplifier (Molecular Devices, Axon Multiclamp 700B), fed into a computer using a National Instruments data acquisition card, and recorded by custom written C# software.

The fictive swim bouts were firstly detected as previously described (Ahrens et al. 2012, 2013), and then being used for decoding fictive turns (Dunn et al. 2016). The fictive swim bouts recorded by the left and right channel were first filtered to standard deviation within 10 ms bins, and then normalized by dividing the average of weighted swim bout amplitude. The swim bout was weighted by a normalized rising exponential function, to take into account the fact that turns affect the start of swim bouts more heavily than the end of swim bouts, so that weight the ends of swim bout more heavily will reduce the effect of turning and lead to more robust normalization of the two channels. For the same reason, to determine the fictive turn amplitude and distance, filtered and normalized fictive signals during swim bouts were weighted with a decaying exponential function (tau = [bout duration]/3) to emphasize the initial burst that determine overall turn direction. Then the turn amplitude was calculated by the difference of weighted power divided by the sum of the weighted power from both sides: $(Power_{Left} - Power_{Right})/(Power_{Left} + Power_{Right})$. The sum of the weighted power is used to measure the swim distance.

Visual stimulation

The visual stimulation consists of serial repetitions of certain patterns.

For photo-taxis, two patterns were presented: Left-Dark - Right-Bright, and Left-Bright - Right-Dark. After each pattern a period of whole field dark was presented. The dark area slightly crosses the midline in order to motivate the fish to swim towards the bright side.

For moving grating stimulation, three or four directional gratings were presented: forward, backward, left-ward, and right-ward. Forward and backward grating were moving along the body axis towards the head or the tail direction. Left- and right-ward grating were oriented 120 degrees away from the head direction, either to the left or the right side.

For spontaneous stimulation, the whole field is dark and no other visual feature was presented.

For dark flash stimulation, whole field dark and whole field light are presented alternatingly for 20 sec each.

For looming stimulation, bright background was presented, and a dot was expanded on either left or right side of the fish. Expansion lasted for 5 seconds, and followed by 25 seconds whole field bright.

MATLAB GUI

A graphical user interface (GUI) was written in MATLAB®. For each fish, the functional data loaded was one calcium trace per each segmented cell, calculated as change in fluorecence $\Delta F/F$. Also loaded are the annotated stimuli, fictive behavior, anatomical location of segmented cells (both raw and registered), anatomy stacks, and annotated Z-Brain masks. The GUI integrates most functions and analyses used in this study, including but not limited to manual cluster selection, selection based on anatomy, set operations, regression methods, cluster methods, storage of clusters, integration with the Z-Brain atlas, and various visualization and export options. The software is written with MATLAB 2016a and tested on a desktop computer with Windows 7.

Image Registration

Nonrigid image registration was done with CMTK (http://www.nitrc.org/projects/cmtk/) as for the Z-Brain atlas, described in Randlett et al. 2015. Additionally, one "bridge brain" was created by imaging the same fish both with the light-sheet microscope (used for the dataset in this study) and a confocal microscope (used for the creation of the Z-Brain atlas). Functional light-sheet datasets were first registered to the bridge brain, and the transformations from light-sheet to confocal for this bridge brain were subsequently applied to complete the registration. To obtain the anatomical location of individual cell-ROI's in the transformed coordinates, we used the CMTK built-in command "streamxform".

Automated Functional Clustering algorithm

This algorithm is custom developed to suit this dataset, and the code is embedded in the GUI. In brief, the first step is extracting functional units (each composed of a small number of neurons) by very fine-scale clustering followed by regression to the cluster centers. In the second step, the subset of functional units that are sufficiently close to each other in the functional correlation space are iteratively merged. This is followed by a third cleanup step (with another regression and a cluster size threshold) to control the quality of the clusters. This

clustering algorithm can either be applied to all cells in the brain or a chosen subset of interest, and the correlation threshold to determine clustering stringency (called "master-threshold" in the following text for convenience) can be tuned (see Results).

More specifically, to extract functional units in Step 1, the algorithm divides all cells in the input into small clusters with k-means clustering to obtain an averaged cluster size of 10 cells. (For large number of cells, the k-means is performed in two steps to speed up the computation, e.g. a first division with k=20 followed by a second division to achieve the desired average cluster size.) Regression to all cluster centers is performed for all cells by calculating the Pearson-correlation coefficient, and cells are assigned to the closest cluster center if the correlation coefficient is larger than the master-threshold. These thresholded clusters are screened with a minimum cluster size threshold of 5 cells. The resulting clusters are the "functional units" used for iterative merging.

For the iterative merging in Step 2, first the correlation distance between all pairs of cluster centers is calculated, and the pair with the smallest distance is merged to form the "seed" of the first cluster. This seed is then expanded by iteratively merging the closest functional unit to the growing cluster, until the next closest cluster does not pass the master-threshold. At this point, if the cluster is larger than the minimum cluster size threshold, this preliminary cluster is saved, and the next "seed" is identified by merging the closest pair of the remaining functional units. After this iterative merging, regression to all cluster centers is performed again as in Step 1, and a minimum cluster size threshold is applied again to obtain cleaned-up functional clusters. This entire process described above as Step 2 is repeated once sequentially to encourage convergence, but no more than once to avoid excessive merging. The final set of clusters are ranked with hierarchical clustering with Optimal leaf ordering.

Cross-Validation

We divided the data into two halves along the time dimension; in the case that multiple stimulus repetitions are present, we used an equal number of intact repetitions for the two halves. We then use the Hungarian method (Munkres assignment algorithm) to match clusters produced from the two halves of the data. A score is calculated as the fraction of number of cells that are assigned to the matched clusters over the total number of cells. This is also visualized as the total "mass" distributed along the diagonal entries.

Screen for anatomically conserved clusters

We used the following criterions to determine whether two clusters are considered occupying comparable locations in anatomical space. First, given a pair of clusters, we calculate the distance of all pairs of cells within each cluster (distance matrices noted as d_1 and d_2), and the distance of all pairs of cells between the two clusters (d_{12}). We calculate the average of the top 1/8 closest distances of d_{12}, and a sufficiently small average distance indicates significant overlap; otherwise this pair of clusters would not be considered further, nor if both clusters that are too spread out, or if the 2 clusters are >10x different in cluster size. Then a score is calculated as min(mean(d_1), mean(d_2))/ mean(d_{12}), and pairs of clusters that pass a minimum threshold of 0.5 are considered comparable in anatomical space. For a given fish, we cycle through all pairs of clusters between this fish and all other fish. For each cluster within this fish, if there are at least 6 other fish that contain at least 1 cluster that are considered comparable in anatomical space, this cluster is marked as a conserved clusters as in Figure 3.6H.

Multiple regression analysis with orthogonalized motor regressors

A set of orthonormal stimulus regressors are generated that represent stimulus features (e.g. different directions for phototaxis and optomotor response) by convolving box-car regressors with a single exponential kernel for the calcium indicator GCaMP6s (half-time 0.4 sec, peak delay 0.08 sec). Motor regressors were generated from fictive behavior features (forward, leftward and rightward swimming) and are orthogonalized against all stimulus regressors using the Gram-Schmidt Process. All cluster centers from the automated clustering results are regressed to the concatenated array of stimulus and motor regressors. The regression coefficients for the multiple stimulus regressors are averaged to obtain a "stimulus correlation" value, and the (orthogonal) motor regressors are averaged for a "motor correlation" value as used in Figure 3.8C.

3.12 REFERENCES

Ahrens, Misha B, Jennifer M Li, Michael B Orger, Drew N Robson, Alexander F Schier, Florian Engert, and Ruben Portugues. 2012. "Brain-Wide Neuronal Dynamics during Motor Adaptation in Zebrafish." *Nature* 485 (7399). Nature Publishing Group: 471–77. doi:10.1038/nature11057.

Ahrens, Misha B., Kuo Hua Huang, Sujatha Narayan, Brett D. Mensh, and Florian Engert. 2013. "Two-Photon Calcium Imaging during Fictive Navigation in Virtual Environments." *Frontiers in Neural Circuits* 7 (June). doi:10.3389/fncir.2013.00104.

Ahrens, Misha B., Michael B. Orger, Drew N. Robson, Jennifer M. Li, and Philipp J. Keller. 2013. "Whole-Brain Functional Imaging at Cellular Resolution Using Light-Sheet Microscopy." *Nature Methods*, no. March. doi:10.1038/NMETH.2434.

Akerboom, J., T.-W. Chen, T. J. Wardill, L. Tian, J. S. Marvin, S. Mutlu, N. C. Calderon, et al. 2012. "Optimization of a GCaMP Calcium Indicator for Neural Activity Imaging." *Journal of Neuroscience* 32 (40): 13819–40. doi:10.1523/JNEUROSCI.2601-12.2012.

Bouchard, Matthew B, Venkatakaushik Voleti, César S Mendes, Clay Lacefield, Wesley B Grueber, Richard S Mann, Randy M Bruno, and Elizabeth M C Hillman. 2015. "Swept Confocally-Aligned Planar Excitation (SCAPE) Microscopy for High Speed Volumetric Imaging of Behaving Organisms." *Nature Photonics* 9 (2). Nature Publishing Group: 113–19. doi:10.1038/nphoton.2014.323.

Burgess, Harold A., and Michael Granato. 2007. "Modulation of Locomotor Activity in Larval Zebrafish during Light Adaptation." *The Journal of Experimental Biology* 210 (Pt 14): 2526–39. doi:10.1242/jeb.003939.

Chen, Tsai-Wen, Trevor J Wardill, Yi Sun, Stefan R Pulver, Sabine L Renninger, Amy Baohan, Eric R Schreiter, et al. 2013. "Ultrasensitive Fluorescent Proteins for Imaging Neuronal Activity." *Nature* 499 (7458): 295–300. doi:10.1038/nature12354.

Cunningham, John P, and Byron M Yu. 2014. "Dimensionality Reduction for Large-Scale Neural Recordings." *Nature Neuroscience* 17 (11): 1500–1509. doi:10.1038/nn.3776.

Dunn, Timothy W. 2015. "Brain-Wide Neural Dynamics Underlying Looming-Evoked Escapes and Spontaneous Exploration." *Doctoral Dissertation, Harvard University*.

Dunn, Timothy W., Yu Mu, Sujatha Narayan, Owen Randlett, Eva A. Naumann, Chao Tsung Yang, Alexander F. Schier, Jeremy Freeman, Florian Engert, and Misha B. Ahrens. 2016. "Brain-Wide Mapping of Neural Activity Controlling Zebrafish Exploratory Locomotion." *eLife* 5 (MARCH2016): 1–29. doi:10.7554/eLife.12741.

Engert, Florian. 2014. "The Big Data Problem: Turning Maps into Knowledge." *Neuron* 83 (6). Elsevier Inc.: 1246–48. doi:10.1016/j.neuron.2014.09.008.

Fahrbach, Florian O, Fabian F Voigt, Benjamin Schmid, Fritjof Helmchen, and Jan Huisken. 2013. "Rapid 3D Light-Sheet Microscopy with a Tunable Lens." *Optics Express* 21 (18). Optical Society of America: 21010–26. doi:10.1364/OE.21.021010.

Fosque, Benjamin F, Yi Sun, Hod Dana, Chao-tsung Yang, Tomoko Ohyama, Michael R Tadross, Ronak Patel, et al. 2015. "Labeling of Active Neural Circuits in Vivo with Designed Calcium Integrators." *Science (New York, N.Y.)* 347 (6223): 755–60. doi:10.1126/science.1260922.

Freeman, Jeremy, Nikita Vladimirov, Takashi Kawashima, Yu Mu, Nicholas J Sofroniew, Davis V Bennett, Joshua Rosen, Chao-Tsung Yang, Loren L Looger, and Misha B Ahrens. 2014. "Mapping Brain Activity at Scale

with Cluster Computing." *Nature Methods*, no. july (July). doi:10.1038/nmeth.3041.

Friedrich, Rainer W., Gilad a. Jacobson, and Peixin Zhu. 2010. "Circuit Neuroscience in Zebrafish." *Current Biology* 20 (8). Elsevier Ltd: R371–81. doi:10.1016/j.cub.2010.02.039.

Jain, Anil K. 2010. "Data Clustering: 50 Years beyond K-Means." *Pattern Recognition Letters*. Vol. 31. doi:10.1016/j.patrec.2009.09.011.

Kinkhabwala, Amina, Michael Riley, Minoru Koyama, Joost Monen, Chie Satou, and Yukiko Kimura. 2010. "A Structural and Functional Ground Plan for Neurons in the Hindbrain of Zebrafish." *PNAS*, 1–6. doi:10.1073/pnas.1012185108/-/DCSupplemental.www.pnas.org/cgi/doi/10.1073/pnas.1012185108.

Lemon, William C, Stefan R Pulver, Burkhard Hoeckendorf, Katie Mcdole, Kristin Branson, Jeremy Freeman, and Philipp J. Keller. 2015. "Whole-Central Nervous System Functional Imaging in Larval Drosophila." *Nature Communications* 6 (May): 7924. doi:10.1038/ncomms8924.

Masino, Mark a, and Joseph R Fetcho. 2005. "Fictive Swimming Motor Patterns in Wild Type and Mutant Larval Zebrafish." *Journal of Neurophysiology* 93 (6): 3177–88. doi:10.1152/jn.01248.2004.

Miri, Andrew, Kayvon Daie, Aristides B Arrenberg, Herwig Baier, Emre Aksay, and David W Tank. 2011. "Spatial Gradients and Multidimensional Dynamics in a Neural Integrator Circuit." *Nature Neuroscience* 14 (9). Nature Publishing Group: 1150–59. doi:10.1038/nn.2888.

Miri, Andrew, Kayvon Daie, Rebecca D Burdine, Emre Aksay, and David W Tank. 2011. "Regression-Based Identification of Behavior-Encoding Neurons during Large-Scale Optical Imaging of Neural Activity at Cellular Resolution." *Journal of Neurophysiology* 105 (November 2010): 964–80. doi:10.1152/jn.00702.2010.

Orger, Michael B, and Herwig Baier. 2005. "Channeling of Red and Green Cone Inputs to the Zebrafish Optomotor Response." *Visual Neuroscience* 22 (3): 275–81. doi:10.1017/S0952523805223039.

Orger, Michael B, Adam R Kampff, Kristen E Severi, Johann H Bollmann, and Florian Engert. 2008. "Control of Visually Guided Behavior by Distinct Populations of Spinal Projection Neurons." *Nature Neuroscience* 11 (3): 327–33. doi:10.1038/nn2048.

Orger, Michael B. 2016. "The Cellular Organization of Zebrafish Visuomotor Circuits." *Current Biology* 26 (9). Elsevier Ltd: R377–85. doi:10.1016/j.cub.2016.03.054.

Panier, Thomas, Sebastián a Romano, Raphaël Olive, Thomas Pietri, Germán Sumbre, Raphaël Candelier, and Georges Debrégeas. 2013. "Fast Functional Imaging of Multiple Brain Regions in Intact Zebrafish Larvae Using Selective Plane Illumination Microscopy." *Frontiers in Neural Circuits* 7 (April): 65. doi:10.3389/fncir.2013.00065.

Peron, Simon, Jeremy Freeman, Vijay Iyer, Caiying Guo, and Karel Svoboda. 2015. "A Cellular Resolution Map of Barrel Cortex Activity during Tactile Behavior." *Neuron* 86 (3). Elsevier Inc.: 783–99. doi:10.1016/j.neuron.2015.03.027.

Portugues, Ruben, Claudia E Feierstein, Florian Engert, and Michael B Orger. 2014. "Whole-Brain Activity Maps Reveal Stereotyped, Distributed Networks for Visuomotor Behavior." *Neuron* 81 (6). Elsevier Inc.: 1328–43. doi:10.1016/j.neuron.2014.01.019.

Prevedel, Robert, Young-Gyu Yoon, Maximilian Hoffmann, Nikita Pak, Gordon Wetzstein, Saul Kato, Tina Schrödel, et al. 2014. "Simultaneous Whole-Animal 3D Imaging of Neuronal Activity Using Light-Field Microscopy." *Nature Methods* 11 (7): 727–30. doi:10.1038/nmeth.2964.

Randlett, Owen, Caroline L Wee, Eva a Naumann, Onyeka Nnaemeka, David Schoppik, James E Fitzgerald, Ruben

Portugues, et al. 2015. “Whole-Brain Activity Mapping onto a Zebrafish Brain Atlas.” *Nature Methods* 12 (September): 1–12. doi:10.1038/nmeth.3581.

Schrödel, Tina, Robert Prevedel, Karin Aumayr, Manuel Zimmer, and Alipasha Vaziri. 2013. “Brain-Wide 3D Imaging of Neuronal Activity in Caenorhabditis Elegans with Sculpted Light.” *Nature Methods* 10 (10): 1013–20. doi:10.1038/nmeth.2637.

Severi, Kristen E., Ruben Portugues, João C. Marques, Donald M. O’Malley, Michael B. Orger, and Florian Engert. 2014. “Neural Control and Modulation of Swimming Speed in the Larval Zebrafish.” *Neuron*, July, 1–16. doi:10.1016/j.neuron.2014.06.032.

Tomer, Raju, Khaled Khairy, Fernando Amat, and Philipp J Keller. 2012. “Quantitative High-Speed Imaging of Entire Developing Embryos with Simultaneous Multiview Light-Sheet Microscopy.” *Nature Methods* 9 (7). Nature Publishing Group: 755–63. doi:10.1038/nmeth.2062.

Van Der Maaten, L J P, and G E Hinton. 2008. “Visualizing High-Dimensional Data Using T-Sne.” *Journal of Machine Learning Research* 9: 2579–2605. doi:10.1007/s10479-011-0841-3.

Vladimirov, Nikita, Yu Mu, Takashi Kawashima, Davis V Bennett, Chao-Tsung Yang, Loren L Looger, Philipp J Keller, Jeremy Freeman, and Misha B Ahrens. 2014. “Light-Sheet Functional Imaging in Fictively Behaving Zebrafish.” *Nature Methods* 11 (9): 1–2. doi:10.1038/nmeth.3040.

Xu, Rui, and Donald II Wunsch. 2005. “Survey of Clustering Algorithms.” *IEEE Transactions on Neural Networks* 16 (3): 645–78. doi:10.1109/TNN.2005.845141.

4 GENERAL DISCUSSION

This thesis can be described by two themes: that of exploration and reduction, both on complex behavior and whole-brain functional data. In this final chapter, I will discuss implications and cautions that come with such approaches, and potential directions that will sustain this unbounded exploration.

4.1 UNIQUENESS OF BEHAVIORAL ALGORITHMS AS HYPOTHESES

In chapter 2, we extracted several behavioral algorithms from the behavioral data, and suggested that they would form useful hypotheses during direct investigations of the neural mechanisms (for example using calcium imaging). One might object that the algorithms we proposed may not represent the "true" algorithms employed in the fish brain. That is, even though these algorithms are sufficient to reproduce certain behaviors, there may be distinct algorithms that also reproduce these behaviors that turn out to be a better representation of the actual neural circuitry. This objection is exactly why the algorithms are presented as hypotheses rather than conclusions based on the data. However, here I would like to discuss why one might consider the proposed algorithms likely to be correct, at least within the scope that the algorithms are implied in.

First of all, the first and second algorithms are completely determined by the statistics of observed data. In these algorithms, the turning angle distributions and paired turning angle distributions are taken directly from the observed data. In this case, all possible alternative algorithms must produce the same distribution of turning angles, and they would be consistent with our hypothesis in the dimensions (of behavioral statistics) that we examined. For example, for the second algorithm, instead of our proposed algorithm that describes the relationship

between two consecutive bouts, one could describe an alternative hypothesis that accounts for three consecutive bouts; and this new hypothesis should not conflict with the old one when only examining two out of three consecutive bouts. Now, in creating a simulation, we had to make specific decisions about how to implement the algorithm. For example, algorithm I treats the first three turns after a light-dark transition with distinct statistics, and groups all other turns together as equivalent. Surely we are not suggesting that the fish implements a hard cut-off like this, but rather that the essence of the calculation is captured by this particular implementation, at least to the extent that it is relevant to our chosen measurement of the behavioral output (in this case, the probability of returning to the virtual circle within three bouts; Figure 2.3E, Figure 2.5M).

In the third and fourth algorithms, there is perhaps more room for possible alternatives. Here the behavioral algorithms are conjectured rules that causally affect certain behavioral statistics, rather than a direct measured distribution of these statistics themselves. However, the effect of these algorithms on their relevant behavioral statistics in the simulation matches the real data. In the third rule I suggest that an equalization of cumulative turning angle causes the fish to spend more time near the virtual border, and the relevant behavioral statistics is the relationship between consecutive cumulative angles ("flipped"), as shown in Figure 2.7F. In the fourth rule I suggest that a modulation of turning statistics based on how long ago the fish crossed the virtual border causes it to make more efficient turns, and the relevant behavioral statistics is the lock-index of the last turn in dark versus first turn in light as a function of number of bouts last spent in light, as shown in Figure 2.9F. It is entirely possible that there are other behavioral statistics that are important to the behavior, and approximating those with alternative hypotheses would generate the desired phenotype in the simulation. However, those alternative hypotheses would also need to reproduce the behavioral statistics that our hypothesis dealt with. Therefore, as for

the first and second rule, they would be consistent with our hypothesis in these dimensions that we chose to approximate. I believe this is a relatively strong constraint on hypothesis generation, and in the case of the third algorithm, because the algorithm in our chosen dimension reproduces the behavioral phenotype as we quantified it (radial bout density), it is unlikely that a different dimension would generate a significant impact in the quantification that we chose; although it is possible to assess the affinity to the virtual border with different quantification measures, for which different algorithms may be proposed.

In general, we tend to base our hypotheses on the principle of efficient calculations, and we avoided algorithms that depend on complex data structures (such as a spatial representation of the virtual circle) or large memory caches (such as cumulative vector sum of all swim bouts). This approach is not necessarily always correct – there may be evolutionary constrains that do not align with this "simplistic" approach. But generally speaking, it is probably true that very verbose algorithms are evolutionarily prohibitive.

In summary, it is probably best to take the algorithms suggested in Chapter 2 as general guidelines to the sorts of computations we expect the fish to be performing, as opposed to direct models of the neuronal circuit. The algorithms are constrained by many aspects of behavioral output and a general bias towards computational simplicity, but are lacking constraints from anatomical and functional circuit data. When such data is available, we might be able to achieve a grounded understanding of the specific neural implementations; and I believe that at least some aspects of our proposed hypotheses would be proven to be relevant.

4.2 Definition and implication of functional clusters

In chapter 3, we presented a custom clustering method that would extract on the order of a hundred functional clusters from the whole-brain functional data. Here I would like to clarify the definition of these clusters and briefly discuss their implications.

Simply defined, a "cluster" is a group of objects that are similar, and cluster analysis groups objects into clusters such that that objects within a cluster are more similar, by some criterion, to each other than to those in other clusters.

Different cluster methods vary in many aspects. One aspect is how many objects will be included in clusters. Take the Fisher's Iris flower data set for example. All the data points in this data set belong to one of the three related flower species, and different clustering algorithms can be tested against this ground truth. In contrast, density-based clustering method mark points in low-density regions as outliers, and only assign clusters to point that have many nearby neighbors. Our method certainly has the characteristics of density-based clustering, as a minimum cluster size threshold is applied after a regression to cluster centers, and the majority of data points are not included in the final results.

Another aspect is the whether the cluster results are described as a single- or multi-scale structure. Multiscale structure is known to be implied in complex systems such as the brain, and has been suggested to confer adaptability and robustness (Shimono and Beggs 2015). Hierarchical clustering uses either a "bottom up" agglomerative approach, or a "top down" divisive approach to generate clusters as one moves up/down the hierarchy. Our clustering approach is clearly agglomerative (iteratively merging functional units), and although we did not explicitly report the full hierarchical relationship between functional units, the sliding cluster stringency threshold is an implicit cutoff of the hierarchical tree to generate one single-scale set of clusters. As we stated in chapter 3, the functional clusters we obtained should be examined in

their context in functional space, for which our GUI is especially well-suited. In other words, the direct results of our cluster algorithm provide a useful scaffold for accessing the large and diverse pool of neural activity profiles. Essentially, we would therefore consider our functional clusters as functional ROI's (region of interest). Just as ROI segmentation in anatomical space, the space not included in ROI's also contain information that may be useful to some degree, yet the ROI's represent the most informative subset for convenience of downstream analysis. By definition as a region of *interest*, there is also no need for a ground truth in ROI segmentation. On this note, we would also like to point out the strong parallel between our algorithm and a common method for ROI segmentation in functional imaging data that aims to isolate individual neurons (Portugues et al. 2014; Bianco and Engert 2015). That method calculates the correlation between anatomically connected pixels based on their functional activity, and grows ROI's from adjacent pixels that are strongly correlated. In our method, we eliminated all anatomical constraints, but consider proximity in the purely functional space.

4.3 Analysis on individual animals versus population analysis

In both chapter 2 and 3, I have shown example data from single animals and distributions or averages from the population. I have not performed rigorous statistical analysis on the individual differences between animals, but this is not to say that they have not been observed or are not deemed significant or potentially fruitful in this data. Given more time and efforts, the following observations may expand to interesting avenues of research.

For free-swimming behavior, one salient aspect of individual difference of left/right turning preferences is addressed in the last section of this chapter (Figure 4.1A; data was originally collected for chapter 2). I have also observed significant individual differences in habituation to dark flashes, swimming speed and bout frequency, latency and turning amplitude

of dark flashes, whether they spend more time close to the virtual border, and as shown in Figure 2.9B and D, differences in the "efficiency" of the turning direction as the fish exits the virtual circle. I suspect that several of these factors listed here are linked, and a simulation with these additional features implemented will likely provide us with more detailed insights.

For the imaging data, I have observed variations in organization of functional clusters across animals; this includes detection of certain functional clusters, exact anatomical size and location of functional clusters, variation in stimulus-type tuning (e.g. some fish respond most strongly to moving stripes, others to looming stimuli), how much the behavior is correlated to a stimulus, how much total motor activity occurred, and whether left turns or right turns are more salient for certain stimuli. The work in chapter 3 is a first study to comprehensively explore the brain-wide neural activity, and has not dealt with any modeling of neural circuits. But given an interest in characterizing specific neural circuitries, I believe that focusing on data from single animals would be highly useful, as circuit elements within an animal may interact and depend on each other strongly, while averaging across fish may obscure these relationships. It is also a salient strength of this dataset that the data quality allows for single trial analysis, and this strength would be mostly lost if averaging across fish (which likely obscures and confounds more features than averaging across trials).

4.4 Neural substrates of temporal phototaxis

In chapter 2, I described a behavior that requires temporal integration of light changes and the motor sequence of the fish to obtain the observed behavioral phenotype. To my knowledge, history dependence of motor outputs in larval zebrafish had not been formally described before my work. In a very recent study (Dunn et al. 2016), a similar dependence of turning direction on past behavior has been described for spontaneous explorations of a

featureless environment. The authors characterized the typical length of such chains of unidirectional turns as approximately 5-10 bouts, which corresponds to about 5-10 seconds. In my study, I mainly reported the correlation in turning direction between two consecutive bouts, but I have certainly observed significant (although rapidly decaying) correlation for longer bout sequences, both for spontaneous swimming and for bouts immediately after an abrupt decrease in illumination. It is most likely that the underlying mechanism for the history dependence that I described is shared with this study.

This underlying circuit, termed the "anterior rhombencephalic turning region" (ARTR) or "hindbrain oscillator" (Ahrens et al. 2013), consists of 2 stripes of neurons on each side of the midline in the anterior hindbrain. The activities of the left and right populations oscillate at a slow frequency, are strongly anti-correlated, and are related to the left/right turning bias. In the whole-brain data from chapter 3, I have observed that the hindbrain oscillator is not only active during spontaneous swimming, but is also active during most stimulus periods. Especially, it is often locked to a turning inducing stimulus (for example, moving gratings for the optomotor response).

In my Virtual Circle assay, I have observed that when the lights are turned off, the first bout in dark is in the opposite direction of the previous bout, but the second bout in dark is strongly correlated to the direction of the first bout in dark. When the lights are turned on again, the first bout in light is also in the opposite direction of the last bout in dark. I speculate that this translates to the switching of the hindbrain oscillator activity: when the lights are turned off, the inactive side of the hindbrain oscillator quickly becomes active, and stays active for at least a few seconds if the environment stays dark. If the darkness is lifted, the currently inactive side (which is the side that was active before the lights were turned off) would be activated again at

the expense of the currently active side (because of the strong anti-correlation, which is presumably mutual inhibition implemented by the two lateral stripes that are GABAergic). This would explain the "lock/flip" properties described in chapter 2, and also the fourth algorithm, which is basically a flip rule with a ~10 sec decay time (we know that the range of decay times for the hindbrain oscillator may exceed 10 sec). Although, this mechanism may not shed light onto the third behavioral algorithm, which likely require angle integration, nor onto the discrepancy between the "correct turning" performance and the simulation with the four behavioral rules.

To experimentally verify the underlying mechanism of the Virtual Circle per se may be more difficult, since the assay is developed for freely swimming fish, and is much harder to perform on tethered fish. The obstacles for the two most common tethered preparations are: for head-embedded and tail-free fish, the baseline spontaneous swimming frequency is very low, which is suboptimal for navigational behaviors; for the fictive preparation, precise decoding of small fictive angles is difficult. In addition, any tethered preparation would be very difficult since a virtually navigating fish would need to "comprehend" a "virtual circle" embedded in a virtual environment. It may be possible to label the candidate neurons for the underlying circuit with activity reporters suitable for free-swimming fish, like Aequorin (Naumann et al. 2010), MAP-mapping (Randlett et al. 2015) or CaMPARI (Fosque et al. 2015).

Although practically, it may be more fruitful to model the activity of the hindbrain oscillator and related circuits, given the whole-brain dataset where the stimulus is a randomized sequence of phototactic, whole-field white or whole-field black stimuli. This dataset contains information about both spatial and temporal changes in illumination in each half of the visual

field, as well as decoded fictive swims. Then this model could be applied to simulate the performance in the virtual circle assay.

4.5 FUTURE DIRECTIONS AFTER WHOLE-BRAIN FUNCTIONAL CLUSTERING

The study in chapter 3 clearly does not even come close to exhausting the usual information in such datasets. Many statistical modelling approaches and decoding analysis can be applied on the data; one can try inferring directional functional connectivity; various theories on population coding could be tested.

The data is recorded with the calcium indicator located to the cell nucleus, which compromises the temporal resolution of the reported calcium dynamics. If cytosolic GCaMP is used instead, high quality cell segmentation that avoids signal cross-talk from neural processes (Pnevmatikakis et al. 2016) may be computationally expensive for data of such large scales. Future improvements of calcium indicators and voltage sensors would also further improve the quality of the data and enable the investigation of questions that previously are reserved for electrophysiological studies.

The data we used are not deconvoluted with the calcium kernel, since a deconvolution step is not important for clustering, and it can take much effort to do it properly. But for interpretation of neural dynamics, deconvolution of the signal would be useful.

The screening for conserved clusters can certainly be conducted better with careful curation of the pre-screened clusters, aided by anatomical expertise. Just as machine vision is not yet a match for human vision, biological expertise and human insights would doubtlessly add value to automated analyses.

Lastly, all the candidate circuits presented in chapter 3 are evidently great directions for hypothesis-driven future studies.

Asymmetry in hindbrain neural activity

There is one more hypothesis that I have not addressed in chapter 3. From preliminary analyses, I have sometimes noted pointed asymmetries in the hindbrain neural activities. It is possible that these asymmetries arise from unbalanced fluorescent labelling or imaging, but I have also observed asymmetric turning behavior following (symmetric) dark flash presentations in large populations of zebrafish (Figure 4.1A). If the behavior output of the brain is often biased, it will not be too surprising that the neural activity would often be left/right asymmetric. Indeed, when I quantify the significant responses to a certain stimulus, I find that the neural activity is much more symmetric in the midbrain than in the hindbrain (n = 6 fish, Figure 4.1B). I hypothesize that the anti-correlated clusters in the anterior hindbrain (as shown in chapter 3), may be a good candidate for where the asymmetric processing of symmetric sensory information arises.

Figure 4.1. Asymmetry in swimming behavior and hindbrain activity.

(**A**) Behavioral asymmetry. A free-swimming single fish is presented with many whole-field dark flashes. For the first turn after a dark flash, some fish always turn in the same direction, while some other fish make left and right turns at comparable frequencies. The left panel shows the laterality index (proportion of left turns) for the first turn after dark flashes, histogram plotted for the population (n = 36 fish). As a control, when counting significant turns (>5º) during the whole experiment instead, the laterality index of most fish is very close to neutral (right panel). (**B**) Asymmetry in hindbrain activity. Left panel, cells that pass regression with the same threshold for leftward and rightward phototactic stimuli. Dotted line indicates midbrain-hindbrain boundary. Right panel, laterality index of cells that pass regression as in the left panel, for the roughly "upstream" and "downstream" anatomical regions, respectively (rostral and caudal relative to the midbrain-hindbrain boundary, respectively). For all fish, the laterality index is more neutral for the "upstream" regions and more asymmetric for the hindbrain region.

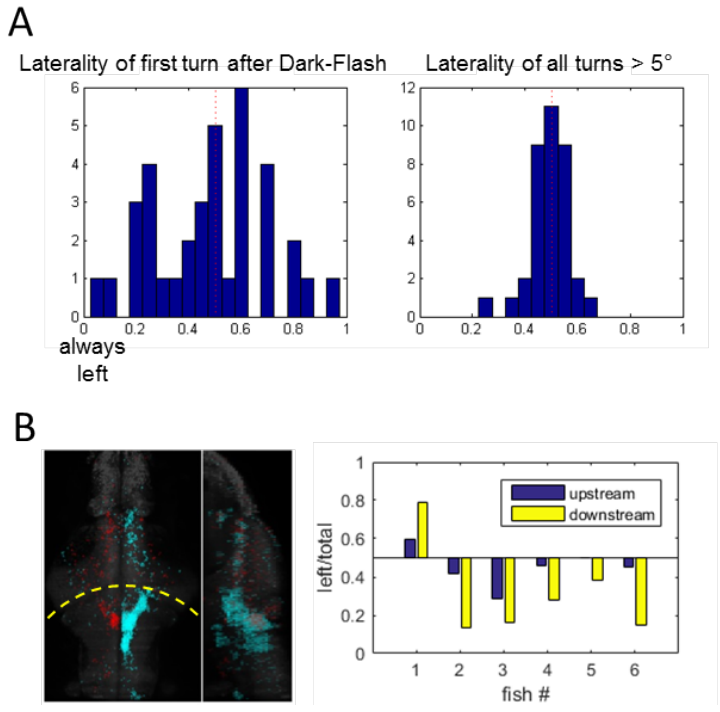

Ahrens, Misha B., Michael B. Orger, Drew N. Robson, Jennifer M. Li, and Philipp J. Keller. 2013. "Whole-Brain Functional Imaging at Cellular Resolution Using Light-Sheet Microscopy." *Nature Methods*, no. March. doi:10.1038/NMETH.2434.

Bianco, Isaac H., and Florian Engert. 2015. "Visuomotor Transformations Underlying Hunting Behavior in Zebrafish." *Current Biology* 25 (7). The Authors: 831–46. doi:10.1016/j.cub.2015.01.042.

Dunn, Timothy W., Yu Mu, Sujatha Narayan, Owen Randlett, Eva A. Naumann, Chao Tsung Yang, Alexander F. Schier, Jeremy Freeman, Florian Engert, and Misha B. Ahrens. 2016. "Brain-Wide Mapping of Neural Activity Controlling Zebrafish Exploratory Locomotion." *eLife* 5 (MARCH2016): 1–29. doi:10.7554/eLife.12741.

Fosque, Benjamin F, Yi Sun, Hod Dana, Chao-tsung Yang, Tomoko Ohyama, Michael R Tadross, Ronak Patel, et al. 2015. "Labeling of Active Neural Circuits in Vivo with Designed Calcium Integrators." *Science (New York, N.Y.)* 347 (6223): 755–60. doi:10.1126/science.1260922.

Naumann, Eva a, Adam R Kampff, David a Prober, Alexander F Schier, and Florian Engert. 2010. "Monitoring Neural Activity with Bioluminescence during Natural Behavior." *Nature Neuroscience* 13 (4). Nature Publishing Group: 513–20. doi:10.1038/nn.2518.

Pnevmatikakis, Eftychios A., Daniel Soudry, Yuanjun Gao, Timothy A. Machado, Josh Merel, David Pfau, Thomas Reardon, et al. 2016. "Simultaneous Denoising, Deconvolution, and Demixing of Calcium Imaging Data." *Neuron* 89 (2): 299. doi:10.1016/j.neuron.2015.11.037.

Portugues, Ruben, Claudia E Feierstein, Florian Engert, and Michael B Orger. 2014. "Whole-Brain Activity Maps Reveal Stereotyped, Distributed Networks for Visuomotor Behavior." *Neuron* 81 (6). Elsevier Inc.: 1328–43. doi:10.1016/j.neuron.2014.01.019.

Randlett, Owen, Caroline L Wee, Eva a Naumann, Onyeka Nnaemeka, David Schoppik, James E Fitzgerald, Ruben Portugues, et al. 2015. "Whole-Brain Activity Mapping onto a Zebrafish Brain Atlas." *Nature Methods* 12 (September): 1–12. doi:10.1038/nmeth.3581.

Shimono, Masanori, and John M. Beggs. 2015. "Functional Clusters, Hubs, and Communities in the Cortical Microconnectome." *Cerebral Cortex* 25 (10): 3743–57. doi:10.1093/cercor/bhu252.